Optimization of Focused Ultrasound and Image Based Modeling in Image Guided Interventions

A DISSERTATION
SUBMITTED TO THE FACULTY OF THE GRADUATE SCHOOL
OF THE UNIVERSITY OF MINNESOTA
BY

Mohamed Khaled Ibrahim Almekkawy

IN PARTIAL FULFILLMENT OF THE REQUIREMENTS
FOR THE DEGREE OF
Doctor of Philosophy

Emad S. Ebbini

May, 2014

Acknowledgements

I would like to acknowledge the support and help of many people, without them this work would not have been realized. It is not possible to enumerate all of them but I would like to express my gratitude to some people in particular.

First of all, I would like to express my deepest appreciation and gratitude to my advisor, Prof. Emad Ebbini, for giving me the chance to be one of his graduate students and for his excellent guidance caring, patience, encouragement and mentorship. Without his guidance and persistent help this dissertation would not have been possible.

I would like to thank my colleagues in my lab, for their great help and support. They provided a good working atmosphere and stimulating discussions.

I am also grateful to my friends specially Abdeltawab Hendawi, Islam Shehata, Omar Mehanna and Tamer Sharaf Eldin for their various forms of support during my graduate study.

Finally, I feel greatly indebted to my parents and my wife, whose love and faith for me has always been my inspiration for every activity that I undertake. I owe a very important debt to the innumerable sacrifices made by them. They were always there for me when I needed them and I cannot imagine myself going through all of this without their help and support.

Dedication

To all my family and those who held me up over the years

Abstract

Image-guided high intensity focused ultrasound (HIFU) is becoming increasingly accepted as a form of noninvasive ablative therapy for the treatment of prostate cancer, uterine fibroids and other tissue abnormalities. In principle, HIFU beams can be focused within small volumes which results in forming precise lesions within the target volume (e.g. tumor, atherosclerotic plaque) while sparing the intervening tissue. With this precision, HIFU offers the promise of noninvasive tumor therapy. The goal of this thesis is to develop an image-guidance mode with an interactive image-based computational modeling of tissue response to HIFU. This model could be used in treatment planning and post-treatment retrospective evaluation of treatment outcome(s).

Within the context of treatment planning, the challenge of using HIFU to target tumors in organs partially obscured by the rib cage are addressed. Ribs distort HIFU beams in a manner that reduces the focusing gain at the target (tumor) and could cause a treatment-limiting collateral damage. We present a refocusing algorithms to efficiently steer higher power towards the target while limiting power deposition on the ribs, improving the safety and efficacy of tumor ablation. Our approach is based on an approximation of a non-convex to a convex optimization known as the semidefinite relaxation (SDR) technique. An important advantage of the SDR method over previously proposed optimization methods is the explicit control of the sidelobes in the focal plane. A finite-difference time domain (FDTD) heterogeneous propagation model of a 1-MHz concave phased array was used to model the acoustic propagation and temperature simulations in different tissues including ribs.

The numerical methods developed for the refocusing problem are also used for retrospective analysis of targeting of atherosclerotic plaques using HIFU. Cases were simulated where seven adjacent HIFU shots ($5000W/cm^2$, 2sec exposure time) were focused at the plaque tissue within the posterior wall of external femoral artery. After segmentation of the ultrasound image obtained for the treatment region in-vivo, we integrated this anatomical information into our simulation to account for different parameters that may be caused by these multi-region anatomical complexities. An FDTD heterogeneous model was used for both acoustic field and temperature computations. The acoustic field simulation considered a concave (40-mm radius of curvature) 32-element array operating at 3.5 MHz. To account for the blood flow in the vicinity of the target (plaque), we have used a modified transient bioheat transfer equation (tBHTE) with a convective term. The results from the numerical simulation were in good agreement with the thermal lesions identified by histological examination of the treated tissues.

Within the context of accounting for the blood flow in tBHTE, the estimation of the displacement of tissue and blood motion are addressed. A new multi-dimensional speckle tracking method (MDST) utilizing the Riesz transform with subsample accuracy in all dimensions is described. Field II simulation of flow data in a channel is generated to provide a validation of the accuracy of the method. In addition, the new MDST method is applied to imaging data from the carotid artery of a healthy human volunteers. The results obtained show that using Riesz transform produces more robust estimation of the true displacement compared to previously published results.

Contents

List of Tables

List of Figures

Chapter 1

Introduction

Ultrasound and MRI are currently the leading image guidance modalities due to their nonionizing nature (which complements the nonionizing nature of HIFU), realtime operation, and temperature sensitivity. Currently approved HIFU systems target tumors and/or tissue abnormalities with uniform soft-tissue access where the distortion to the therapeutic beam is minimal. The success of these early applications has encouraged a number of research groups worldwide to investigate the feasibility of HIFU treatment of deep-lying tumors [1] with complex structures that may adversely affect the quality of the HIFU focus thus limiting the efficacy of the treatment. For example, patients with hepatocellular carcinoma or lung cancer may benefit greatly from a noninvasive approach with low morbidity due to the fact that only $10-15\%$ of the patient population is eligible for surgical resection [2]. In order to ensure adequate treatment of the target volume, the partial obstruction of the HIFU beam by the rib cage must be accounted for. Research efforts have addressed the transthoracic focusing (or refocusing) of the HIFU beam in the presence of strongly scattering objects like the ribs when targeting liver tumors. An image-guided HIFU surgery based on the dual-mode ultrasound array (DMUA) approach has been proposed where the DMUAs are capable of operating in both imaging and therapeutic modes using the same transducer elements. This results in inherent registration between the imaging and therapeutic coordinate systems thus providing the physician with instant image-based feedback for guidance and control of the HIFU beam to maximize the power deposition at the target, while minimizing collateral damage to critical tissue structures in the path of the HIFU beam.

The image-based refocusing has provided a demonstration of the feasibility of minimizing exposure at the critical structures, yet it does not offer any theoretical guarantees of maximizing power deposition at the target. The use of forward numerical modeling of wave propagation in the complex medium may be the only method for addressing the beam optimization problem noninvasively.

The goal of my thesis research is to develop optimal synthesis methods for the HIFU beams in both imaging and therapy modes, taking the forward heterogeneous propagation model into account. Based on imaging feedback, the physician can directs dynamic treatment plans with a model, like the one we propose, using the Finite-Difference Time-Domain (FDTD) Module that involves acoustic and temperature calculations. The computational model will play a key role in the envisioned system before, during, and after the treatment.

1.1 HIFU History

Even though HIFU was recognized in 1927 [3], it was not implemented as a regular method of treatment until much later. John Lynn and his coworkers in 1942 demonstrated, using focused ultrasound, that a localized area of damage $in - vitro$ tissue could be created [4]. This approach has encouraged researchers to investigate the using of HIFU in the treatment of medical conditions. Focused ultrasound was employed for brain therapy in the 1950s [5], and since then, clinical application has been attempted for cancer treatment. HIFU, was first used in the treatment of prostate cancer in 1995 [6]. This has been followed by additional clinical studies on different body organs [1]. Recently treatment of prostate cancer using HIFU [7] was approved worldwide.

Currently, MRI guidance has been adopted for HIFU treatment [8]. The MRI guided focused usltrasound is being used to estimate the temperature rise and the image anatomical structure [9]. The reason behind this is the precise tissue localization that MRI provides, and the accurate estimation of the temperature elevation at the treated region. We can achieve a precise data of monitoring the ongoing ablation process in the depth of the lesion in addition to temperature changes in tissue.

One of the applications of MRI guidance with HIFU is the treatment of uterine fibroids, which has been approved by the FDA. The targeted volume within the uterine

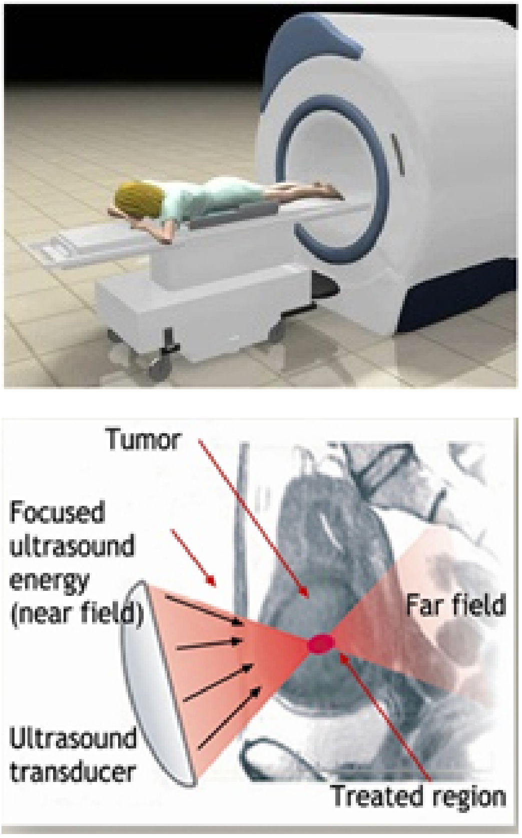

Figure 1.1: The targeted volume within the uterine fibroid is localized using MR. Image obtained from www.insightec.com

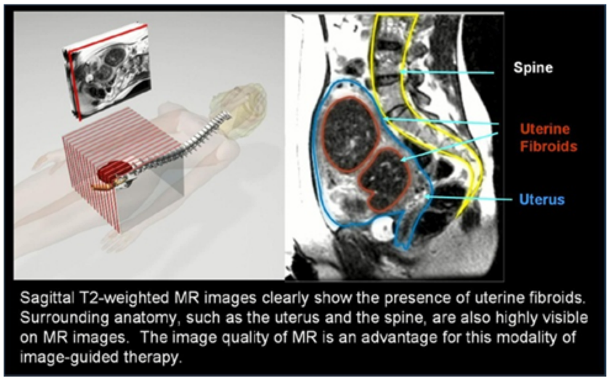

Sagittal T2-weighted MR images clearly show the presence of uterine fibroids. Surrounding anatomy, such as the uterus and the spine, are also highly visible on MR images. The image quality of MR is an advantage for this modality of image-guided therapy.

Figure 1.2: Focused ultrasound energy emanating from the transducer to a specific focal point on the uterine fibroid. Image obtained from www.insightec.com

fibroid is localized using MRI as shown in Fig. 1.1.

The beam of focused ultrasound energy emanates from the transducer through the skin and uterus to a specific focal point on the uterine fibroid as shown in Fig. 1.2.

In addition, Fig. 1.3 illustrates the targeted prostatic volume that is localized with the bi-planar ultrasound imaging probe. High-energy ultrasound waves are focused through the rectal wall to the targeted prostate area and the targeted zone destroyed by each shot is cigar-shaped and measures ~ 19 to $\sim 24mm$ in height by $\sim 2mm$ in diameter ($60 - 80\,^{\circ}$C temperature for 2 sec for each shot). By repeating the shots, and moving the focal point between each shot, it is possible to destroy a volume that includes the whole prostate (treatment time 2 - 3 hours).

The treatment transducer has to be located within an available acoustic window to the target to limit any possibilities of damage in the intervening tissue. Peizocomposite technology offers improved control over the beam patterns compared to conventional PZT transducer technology. Low f-number transducer arrays allow for deep localized treatment of tumors. The f-number is defined as the ratio of the focal length to the aperture size. The use of phased array technology in HIFU applications allows for the pursuit of optimal driving of signal distributions for thermal therapy applications (e.g. multiple-focus patterns conforming to the tumor geometry [10].

In addition, other researchers utilize the nonlinear imaging technique to capture lesion formation using a second order volterra filter to form a quadratic B-mode image from the ultrasound echo data [11, 12]. This technique utilizes the cavitation phenomena accompanying the lesion formation to increase the contrast ratio of the formed lesion.

1.2 Overview of treatment Modalities

Laser, microwave, radio-frequency, cryotherapy and ethanol ablation are considered invasive techniques that have been used for local ablation. They are all facing difficulties in ablating more than $5cm$ in diameter. In addition, one of the most recognized drawbacks of radiotherapy is the potential risk of affecting healthy tissue located in the path of the therapeutic radiation beam during treatment. This happens to the tissue around the target point that is exposed to the hazardous radiation.

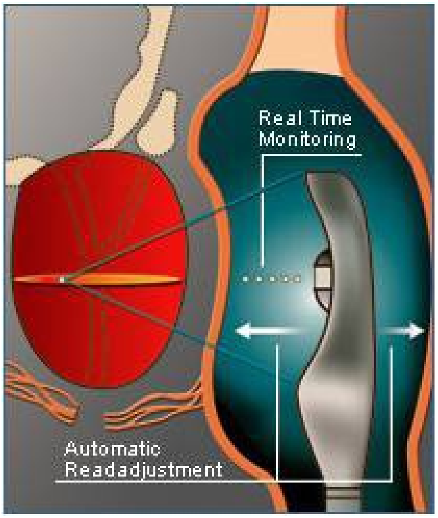

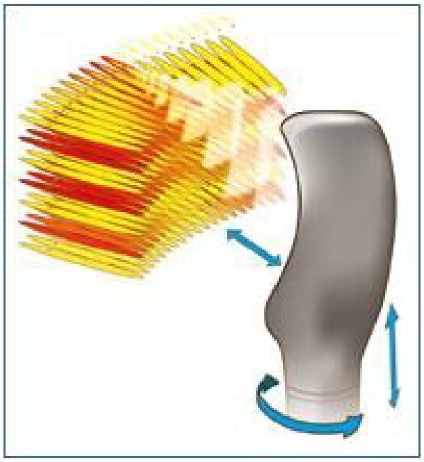

Figure 1.3: The targeted prostatic volume that is localized with the bi-planar ultrasound imaging probe. Image obtained from www.hifu.org.uk

As indicated previously, MRI and ultrasound are being used for guidance and monitoring of HIFU therapy. Each one has its pros and cons, e.g. (MRI provides temperature data within seconds after HIFU exposure, yet it is expensive). The draw back of using MRI guidance is the degradation of the image, if any artifacts exists, due to tissue motion; this will directly impair the temperature maps. The liver is one of the most mobile organs in the body, thus MRI guidance is difficult to apply. Constantly, the ongoing research tries to expedite the process of acquiring the image to follow the creation of lesions under the effect of respiration without degradation of thermal maps [13]. We should emphasize that ultrasound is facing, with less effect, the organs motion problem (liver and kidney) as a result of respiration. There is ongoing research on motion compensation techniques [14]. It is also interesting to note that ultrasound has been used as a guidance to monitor the temperature changes in tissue as well. This was in part due to the change of physical properties (speed of sound and thermal expansion) with temperature. Maintaining a monitoring feedback of the lesion formation and the direct impact on the excitation power of the HIFU transducer is one of the important parameters that has to be taken into consideration to achieve a closed loop control of the treatment procedure. To get a precise targeting localization of the HIFU beam, we need to minimize the hepatic movement by controlling patient immobilization and respiratory movement.

1.3 Thermal Therapy with HIFU

The patient is ready for the treatment process after properly positioned on the ablation table with the right dose of anesthesia. Then a three dimensional sonographic image is captured of the tumor which is being divided into sections. HIFU is exposed to the target tumor with a succession of shots on each section until completely ablating the target region. To guarantee the existence of coagulation necrosis in the desired treatment area, a real-time image is being acquired to monitor the echogenic change of the region of interest and use the sufficient exposure parameter to create the lesions. A proper amount of care to the body temperature has to be taken into consideration while using HIFU in such ablation procedures.

1.4 Limitations of HIFU

As indicated previously, HIFU has many advantages over other techniques. However, it still has some limitations that have to be considered.

- Positioning of the patient during the procedure: It is recommended to use the right lateral position and try to avoid, whenever possible, the prone position as it poses certain challenges under anesthesia.
- Lengthy time of treatment which will directly influence the anesthesia time: This might affect non-healthy patients. The prolongation of treatment time has been attributed to either large tumors in most of the treatment cases, limitation of the transducer intensity level or the avoidance of damaging the overlying structures in case high intensity levels are used.
- There is a real challenge in HIFU treatment to create lesions at the dome of the right lobe. The lungs hinder the HIFU beam from passing towards the target lesion. A right hydrothorax is required for ablation of such cases.
- Tumors located behind the ribs or any obstacles that might attenuate or reflect the HIFU beam represents a real challenge for HIFU therapy: To overcome this problem, a resection of the part of the ribs that are blocking the beam or a refocus algorithm, like the one presented in this thesis, is necessary.

We can conclude that some of the tumors are barely accessible to a HIFU beam. There is an ongoing extensive research to try to facilitate access to difficult places to overcome such problems. To evaluate the feasibility of this technique, we have to study the advantages and limitations of each case study.

1.5 Dual Mode Ultrasound Arrays

Dual Mode Ultrasound Arrays (DMUAs) are capable of operating in both imaging and therapeutic modes using the same transducer elements. The idea of achieving imaging and therapy with the same transducer was introduced by Ebbini and his coworkers in the 1990's [15]. More recently, the advent of piezocomposite transducer technology has allowed for the fabrication of a new generation of therapeutic arrays with relatively wide bandwidth and low cross coupling between elements resulting in new dual-mode ultrasound array (DMUA) systems for imaging and therapy [16]. Several groups are investigating the use of the DMUA to maximize the benefits achieved with this new technique. The University of Minnesota group (Ebbini and coworkers) recently published a series of papers illustrating the advantages and describing the challenges of the DMUA approach, including the use of image-based feedback in targeting tissues partially obstructed by ribs. Moreover, a realtime DMUA prototype has been designed and tested since April 2010. In addition, they have investigated several approaches of spherical shell DMUA imaging types, e.g. (single transmit focus (STF), synthetic aperture (SA) imaging, quadratic B-Mode and pulse inversion imaging [11] and post beamforming 2-D pseudoinverse filter for coarsely sampled ultrasound arrays [17]). More specifically, Ebbini's research aims at the validation of a new procedure that integrates the feedback and control of DMUA systems in the safe and efficacious targeting of subcostal tumors using HIFU. It will be possible to design and implement an adequate solution to the treatment of currently challenging diseases like hepatocellular carcinoma (HCC) and other subcostal targets with the use of large-aperture DMUAs with sufficient therapeutic gain, adequate parametric imaging with specificity to HIFU induced tissue changes, and interactive treatment planning software.

1.6 Ultrasound Imaging

Ultrasound imaging is an important, noninvasive and safe tool for medical diagnosis. Typically operating at frequencies between 1 and 10 MHz, the electrical signals are transformed into pressure waves using piezo electrical transducers and produce images through the echoes of the mechanical energy from boundaries through tissues due to reflection and scattering. Basically, the spatial pulse echo response for a single scatterer corresponds to the convolution of the spatial impulse responses of the transmit and receive apertures. Ultrasound systems have been increasingly targeted for portable, low cost and low-power consumption with some ultrasound devices implemented as application-specific integrated circuits (ASICs) [18]. However, the ASIC design suffers from its limitation to provide flexibility for further evolving applications. Some other applications of ultrasound utilizes the digital signal processors (DSPs) to improve the flexibility [19]. However, because of its limited transfer bandwidth, it is challenging to do beamforming for multiple channels on a single DSP chip. Although some applications based on Multi-Core DSPs have been proposed recently [20], the DSP-based approach is suffering from higher power consumption and non-prototypical design. Besides the diversity of the platforms, the implemented signal processing schemes also vary in terms of beamformer operation. Because the echoes are received by a group of transducer elements, an alignment of the echo signals of different transducers is necessary; hence, beamformer plays the role of aligning signals by delaying them appropriately. To improve resolution, accurate delays are desired in ultrasound imaging. The limitations of an analog-digital converter (ADC) constraints the time difference between two samples. Typically, there are two ways to improve the time delay accuracy in beamformer. One is using phase rotation, which is also known as direct sampled in-phase/quadrature (DSIQ) beamforming. This method yields degraded image quality because of its narrow band signal [20],[21]. Another way to improve time delay is by using interpolation filter. Traditionally interpolation-based filter requires up-sampling before low-pass filter [22], which requires high operating frequency in the DSP part and is not suitable for a low-cost FPGA. A more efficient method involving polyphase filter is employed with other groups. Besides the implementation of delay units, the calculation of delay is challenging for dynamic focusing, which requires delays to be updated continuously. An efficient way to compute the delay information is proposed in [23], but the resolution of the delay is bounded by the period of operating frequency. To acquire more accurate delay information, a higher operating frequency is necessary. Another widely-used method is to pre-compute the delays and save them in memory. Owing to memory-limitation, only pseudo-dynamic focusing is implemented in the related works, where delay information is only updated for some pre-determined depths [24], [23], instead of continuously updating them.

Beamforming Technique

The nature of the considerable time differences in signal arrivals among channels requires the beamforming to improve the quality of the ultrasound image. Fig. 1.4 shows the nature of how signals are organized to detect a focal point in an ultrasound system.

Assuming that the focal point F is under detection, the echo signals from the focal point arrive to varied channels at different time. The role of beamforming is to delay and sum echo signals from the transducers appropriately. After the proper delays in the beamformer, the signals are aligned together in a same time interval. Then all aligned signals are summed together to acquire the signal corresponding to the focal point F.

During the receive phase, dynamic focusing requires the beamformer to change the focal point continuously to corresponding sampled signal depth by adjusting the delays of all channels. Fig. 1.5 shows how the flight paths of signals change during the receive phase. Multiple channels are used to sense the echoed back ultrasound signals. An entire ultrasound image consists of multiple scan lines. To detect a single scan line, a series of focal points are sensed. Assuming the scan line starts from the position of channel A, the locations of the focal points are determined by the signals sampled by channel A. As Fig. 1.5 shows, there exists a depth in the physical positions between each two sampled data. The distance d between two focal points satisfies $d = (v * T_s)/2$, where T_s is the sampling interval and v is the speed of sound in tissue. The dynamic beamforming should delay signals received, by all transducer elements, variably for every sample. For the focal point 1 in the figure, it is assumed that the time of flight from transmission to reception by channel A, is T_1. The time for channel B to receive it is T_2, where $T_2 > T_1$ holds. It implies that the signal echoed back from point 1 will be delayed by $(T_2 - T_1)$ in channel A to be aligned with the signal in channel B. For the subsequent focal point 2, the time that corresponding signals received by channel A and channel B respectively are:

$$\hat{T_1} = \delta T_1 + T_1, \quad \hat{T_2} = \delta T_2 + T_2 \tag{1.1}$$

According to the property of the triangle, we have that $(b - a) < d$. Thus it derived that:

$$\begin{aligned} \delta T_2 &= \frac{d + b - a}{v} < \frac{2d}{v} \\ \frac{2d}{v} &= \delta T_1 \end{aligned} \tag{1.2}$$

This implies that the corresponding signal of focal point 2 has arrived to channel B

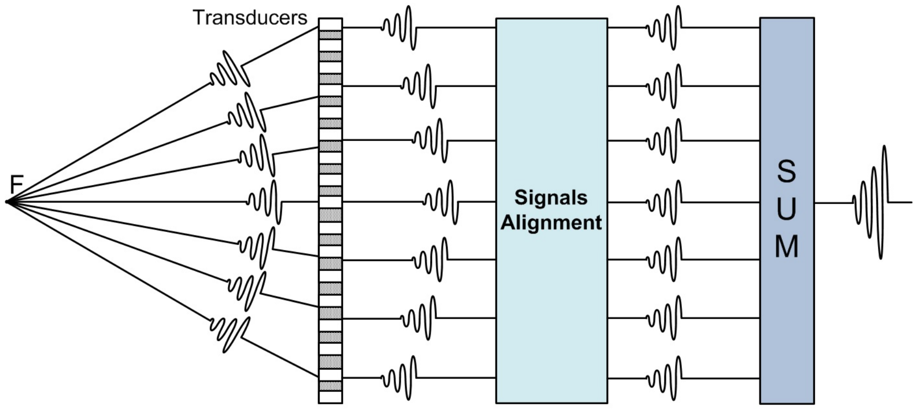

Figure 1.4: Signals Alignment in Ultrasound System

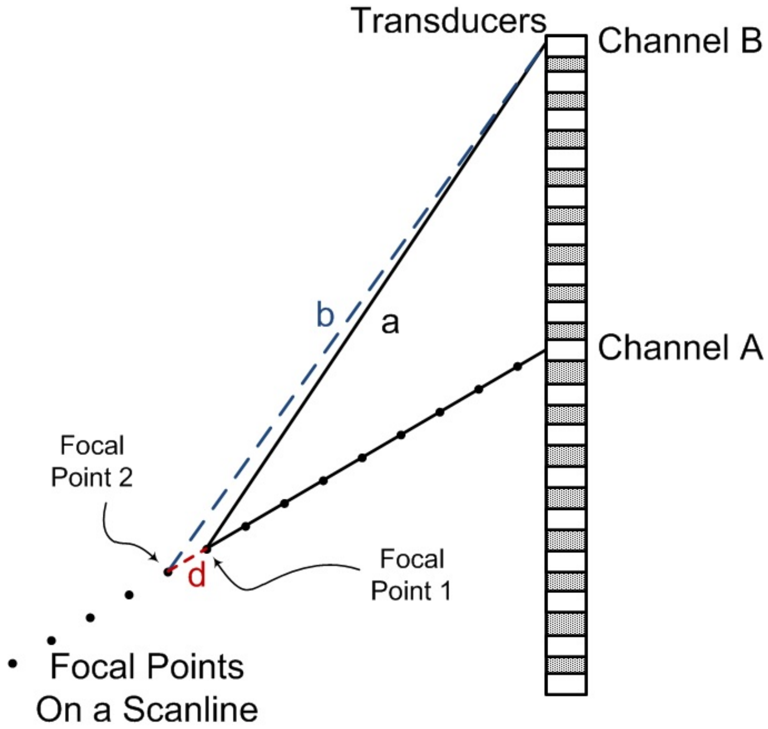

Figure 1.5: Variations of Echo Paths In Receiving Signals

before its next sampling. If $\delta T_1 - \delta T_2$ is relatively short, we can retrieve the fraction delay between two samples after sampling the next signals in channel B. However if $\delta T_1 - \delta T_2$ is large enough, the corresponding signal has to be accessed without sampling next signal. In this case, the previous sampled signal from channel B will be used twice and be aligned with both signals received from the channel for focal Point 1 and focal Point 2. Although same signal would be used twice to be aligned, different fractional delays are necessary to affect the identical sample to achieve finer alignment. To acquire fractional delays on the sample, there are techniques that use a 100 MHz sampling rate with digital interpolation filters [25], which allow the signals to be sampled at a lower frequency and concurrently get finer delays [26],[27]. Other techniques use the polyphase interpolation filter to acquire finer delays.

1.7 Overview and Contribution

A new optimization algorithm is presented that limits the power deposition over critical points while maximizing the exposure at the targets with numerical modeling of wave propagation and heat generation in heterogenous media. In addition, we present an FDTD to simulate the results of a lesion formation experiment based on actual $in-vivo$ treatments, this being achieved by a simulation modeling of the wave propagation in heterogeneous medium from the surface of a 3.5 MHz array prototype with 32-elements. The simulation model considered the effect of wall thickness of large arteries and the heat sink effect of flowing blood. We also introduce a new multi-dimensional speckle tracking method with subsample accuracy in all dimensions. The results obtained show that using the Riesz transform produces a more robust estimation of the true displacement of the simulated model compared to previously published results.

1.8 Dissertation Organization

The thesis consists of six chapters including the introduction. The chapters are organized as follows:

- Chapter 1 introduces the History of HIFU, highlighting the importance of HIFU as a non-invasive technique. The chapter also discusses the limitations of HIFU and the analytic goals pursued in this thesis.

- Chapter 2 presents the acoustic and temperature model presented in this thesis. In addition, it discusses the numerical simulation models used in solving the partial differential equations used in the model. In addition, it summarizes the theoretical and empirical relations used for thermal dose calculation.
- Chapter 3 represents the problem of focusing a HIFU beam on a target obstructed by the ribs. It also compares a new refocusing algorithm used in this thesis to an earlier algorithm using the pseudo inverse synthesis approach to solve the same problem.
- Chapter 4 describes the simulation of the effect of high intensity focused ultrasound (HIFU) in non-homogenous media for targeting atherosclerotic plaques in-vivo.
- Chapter 5 introduces a new multi-dimensional speckle tracking method (MDST) with subsample accuracy in all dimensions.
- Chapter 6 presents a final conclusion with a discussion on future work.

Chapter 2

Models Overview

2.1 System model

A numerical model is used to simulate the propagation of the ultrasonic pulses and the temperature field achieved. The model is based on the wave equation and the bio heat transfer equation (BHTE). A finite difference approximation of the partial derivatives are required in the numerical solution of the partial differential equations (PDE), which provides us with the required expressions for the function partial derivative in terms of function values at a number of neighboring grid nodes. The FDTD method [28] is used to analyze the HIFU field and temperature rise throughout the therapeutic region.

2.2 Numerical Method

The FDTD method is a powerful tool for solving a broad range of PDE. Numerical methods are used to compute an unknown scaler or vector function of position and time at the nodes of a structured grid of the solution domain that satisfies the required PDE. If there is time dependence, the discrete time level will be separated by a constant or variable time step $\triangle t$ otherwise, the computation is done at one time instant corresponding to a steady state. In the case of Cartesian coordinate, the grid consists of parallel lines to the $x, y, and z$ axes with $\triangle x, \triangle y, \triangle z$ as a grid spacing. The grid spacing may vary across the computational domain to solve sharp variation regions. This approximation that determines the unknown functions at a set of neighboring grid points at one or several time levels replaces the PDE with a finite difference equation. This replacement of the partial derivatives with algebraic differences is called finite difference discretization. The finite difference equation is applied at interior and boundary nodes. In certain cases, it is important to extend the solution domain beyond the natural boundaries of the physical problem to improve the expressing of the boundary condition, this point will be further explained on the implementation of the perfect matched layer in solving the field equation. The accuracy of the FDTD depends on the size of the space grid and the time step, the method becomes consistent as the accuracy increases. We have to apply well established finite difference formulas to approximate temporal and spatial derivatives in the PDE to increase the consistency. The finite difference method is consistent if the difference between the modified differential equation and the PDE has terms that are proportional to the powers of the time step and grid spacings. There is also another important term that has to be studied, this term is the stability. The numerical method is stable if the numerical solution is bounded and no growing oscillations exist. In case there is a growth in the numerical solution, the rate should at most be equal to that of the exact solution. In our case, we ensure stability by the absence of noticeable spatial or temporal oscillations in the computational results.

2.3 Acoustic Model

2.3.1 Perfect Matched Layer

The finite difference equation is applied at interior and boundary nodes. In certain cases, it is important to extend the solution domain beyond the natural boundaries of the physical problem to improve the expression of the boundary condition. This extension is called the perfect matched layer (PML) which has an important role in numerical simulations of acoustic wave propagation in inhomogeneous media. This is achieved by artificially adding boundary conditions in finite difference methods to minimize the reflection caused by the edges of the computational domain. The PML was first introduced in [29] as a material absorbing boundary condition (ABC) for electromagnetic waves. We follow [30] to account for the coupling of loss from a PML and the regular absorption loss in acoustic wave propagation.

2.3.2 Mathematical Methods

The propagation of the ultrasound field is governed by the (scalar) wave equation. This numerical simulation is providing all the information needed after refocusing the beam in inhomogeneous medium and is necessary to achieve a treatment plan before the actual treatment get into place. We used this equation to model the HIFU field from the DMUA. This model followed the Euler and continuity equations:

$$\boxed{\begin{aligned}\frac{\partial \mathbf{v}}{\partial t} &= \frac{-1}{\rho}\nabla \mathbf{p} \\ \frac{\partial \mathbf{p}}{\partial t} &= -\rho.c^2\nabla.\mathbf{v} - \beta c^2 \mathbf{p}\end{aligned}} \tag{2.1}$$

where $\mathbf{v}$, $\mathbf{p}$, and c, denote the particle velocity, pressure and speed of sound, respectively. The absorption coefficient β is used as an indication of the absorptive loss in the medium which can be related to the attenuation coefficient σ through the complex wave number k as in the following equation:

$$\begin{aligned} k &= \sqrt{\frac{\omega^2}{c^2} + iw\beta} \\ &= \omega/c' + i\sigma \end{aligned}$$

The c and σ are frequency dependent in absorptive media, but because the HIFU beam is narrowband, we will assume that they are independent of frequency over the bandwidth of interest. The two equations in 2.1 can be coupled to get the second order partial differential equation as in equation 2.2.

$$\boxed{\frac{1}{c^2}\frac{\partial^2 \mathbf{p}}{\partial^2 t} = \rho\nabla.\rho^{-1}\nabla\mathbf{p} - \alpha\frac{\partial \mathbf{p}}{\partial t}} \tag{2.2}$$

In this thesis, we solve the decoupled equations. A modification has to take place, according to [30], in equation 2.1 using stretched coordinates. This new coordinate will make it suitable to solve the PDE equation numerically in the PML region which is used as an ABC. The stretching is chosen as

$$g_\xi = s_\xi + i\frac{(h\sigma)_\xi}{\omega}(\xi = x, y, z)$$

as ω is the angular frequency and ∇_g is expressed as:

$$\nabla_g = \Sigma_{\xi=x,y,z}\ \xi \frac{1}{g_\xi} \frac{\partial}{\partial \xi}$$

and $h = \rho c^2$. The term $(h\sigma)_\xi$ represents the loss in the PML while s_ξ is a scaling factor. Equation 2.1 should be modified by using the stretched coordinates and by replacing ∇ with ∇_g we will get the following:

$$\boxed{\begin{aligned} s_\xi \frac{\partial \mathbf{v}_\xi}{\partial t} + (h\sigma)_\xi \mathbf{v}_\xi &= \frac{-1}{\rho} \nabla \mathbf{p} \\ s_\xi \frac{\partial \mathbf{p}}{\partial t} &= -h\nabla.\mathbf{v} - (s_\xi \beta c^2 + (h\sigma)_\xi)\mathbf{p} \end{aligned}} \tag{2.3}$$

These two equations are used in the whole computational domain with $s_\xi = 1$, $(h\sigma)_\xi = 0$ for the interior region.

The spatial and temporal partial derivatives are approximated by a Taylor series expansion for each node in the computational grid; this grid consists of spatial dimensions using uniform spacing in addition to the temporal dimension $\triangle t$ with uniform spacing. A perfect matched layer as a material ABC [30] was applied at the computational edge of the grid to eliminate the reflections from the outer boundary of the computational domain. A higher absorption is achieved by using PML as an absorbing boundary condition. To include the PML in the absorptive media for the acoustic waves, the computational domain, consisting of N_x, N_y, N_z cells, in 3D, is partitioned into a normal interior region and the boundary PML region.

After modification of equation 2.1 by using the stretched coordinates as described, and after using the FDTD method, the equations should be approximately:

$$\begin{aligned} s_\xi[\mathbf{v}_x(j_x, j_y, j_z, n) - \mathbf{v}_x(j_x, j_y, j_z, n-1)]/\Delta t \\ +(h\sigma)_\xi[\mathbf{v}_x(j_x, j_y, j_z, n) - \mathbf{v}_x(j_x, j_y, j_z, n-1)/2] \\ = -\frac{1}{\rho\delta\xi}[p(j_x, j_y, j_z, n) - p(j_x - 1, j_y, j_z, n)] \end{aligned} \tag{2.4}$$

After rearrangement, the time stepping equation for $\mathbf{v}_x$ is equal to

$$\boxed{\begin{aligned} \mathbf{v}_x(\prime j_x, j_y, j_z, n) = {} & A\mathbf{v}_x(\prime j_x, j_y, j_z, n-1) \\ + {} & B[p(\prime j_x, j_y, j_z, n) \\ - {} & p(\prime j_x - 1, j_y, j_z, n)] \end{aligned}} \tag{2.5}$$

where

$$\boxed{\begin{aligned} A = {} & \frac{s_\xi/\Delta t - (h\sigma)_\xi/2}{s_\xi/\Delta t - (h\sigma)_\xi/2} \\ B = {} & -\frac{1}{\Delta\xi(\frac{s_\xi \rho}{\Delta t} + \frac{(h\sigma)_\xi \rho}{2})} \end{aligned}} \tag{2.6}$$

For the pressure field p:

$$\begin{aligned} s_\xi[p(j_x, j_y, j_z, n+1) - p(j_x - 1, j_y, j_z, n)]/\Delta t \\ +(s_\xi \beta c^2 + (h\sigma)_\xi)[p(j_x, j_y, j_z, n+1) + p(j_x - 1, j_y, j_z, n)/2] \\ = -\frac{h}{\delta\xi}[\mathbf{v}_x(j_x + 1, j_y, j_z, n) - \mathbf{v}_x(j_x, j_y, j_z, n)] \end{aligned} \tag{2.7}$$

The time stepping equation for p is approximately equal to

$$\boxed{\begin{aligned} p(j_x, j_y, j_z, n+1) = {} & Cp(j_x, j_y, j_z, n) \\ + {} & D[\mathbf{v}_x(j_x + 1, j_y, j_z, n) \\ - {} & \mathbf{v}_x(j_x, j_y, j_z, n)] \end{aligned}} \tag{2.8}$$

where

$$\boxed{\begin{aligned} & C = \frac{s_\xi/\Delta t - (s_\xi \alpha c^2 + (h\sigma)_\xi)/2}{E} \\ & D = -\frac{h}{E} \\ & E = s_\xi/\Delta t + (h\sigma)_\xi \alpha c^2 \Delta t/2 + (s_\xi \alpha c^2 + (h\sigma)_\xi)/2 \end{aligned}} \tag{2.9}$$

The PML region is responsible for the absorption of the outgoing propagated wave; it consists of $L = 50$ cells with an increasingly quadratic attenuation profile toward the outer boundary as follows:

$$(h\sigma)_\xi(j_\xi) = \frac{(L - 0.5 - j_\xi)^q}{(L - 0.5)^q}\omega_{\xi,max} \qquad (j = 0, ..., L-1) \tag{2.10}$$

where $q = 2$ as we are using a quadratic profile and $(h\sigma)_{\xi,max}$ is the value at the center of the first cell. The PML boundary condition highly attenuates any reflections into the interior domain region. This acoustic numerical simulation provides all the information needed after directing and refocusing the beam, which is necessary to achieve a treatment plan.

2.4 Thermal Model

As an acoustical signal propagates, some of the energy is absorbed in the tissue leading to increased temperature which can be modeled by the BHTE used to govern the thermal effects in tissue. The temperature model is described by the following equation:

$$\boxed{\rho C_t \frac{\partial \mathbf{T}}{\partial t} = k\nabla^2 T - W_b C_b (T - T_b) + Q} \tag{2.11}$$

Where T is the tissue temperature, T_b is the arterial blood temperature, ρ is the tissue density (kg/m^3), C_t is the specific heat of tissue $(J/kg.)$, C_b is the specific heat of blood, k is the thermal conductivity of the tissue $(\mathbf{W}/m)$, Q is the applied intensity deposited by an external applicator $(\mathbf{W}/m^3)$, W_b is the perfusion parameter $(kg/m^3 s)$. A Forward-Time Central-Space (FTCS) has been used by applying a forward difference for the time derivative and a centered difference for the second spatial derivative as follows:

$$\boxed{\begin{array}{rcl} \rho C_t \dfrac{\mathbf{T}^{n+1}_{i,j,l} - \mathbf{T}^{n}_{i,j,l}}{\triangle t} & = & k \left[\begin{array}{cc} \frac{\mathbf{T}^n_{i+1,j,l} - 2\mathbf{T}^n_{i,j,l} + \mathbf{T}^n_{i-1,j,l}}{\triangle x} & + \\ \frac{\mathbf{T}^n_{i,j+1,l} - 2\mathbf{T}^n_{i,j,l} + \mathbf{T}^n_{i,j-1,l}}{\triangle y} & + \\ \frac{\mathbf{T}^n_{i,j,l+1} - 2\mathbf{T}^n_{i,j,l} + \mathbf{T}^n_{i,j,l-1}}{\triangle z}) & \end{array} \right] \\ & - & W_b C_b (\mathbf{T}_a - \mathbf{T}^n_{i,j,l}) + Q \end{array}} \tag{2.12}$$

The numerical error is on the order of $\triangle t$ and $\triangle \xi$. In order to meet the stability criteria, the temporal step must follow the Courant, Friedrichs and Lewy (CFL) condition [31] to achieve the convergence of the difference approximation.

2.5 Thermal Dose Model

An empirical exponential relation between the tissue temperature and the exposure time required to coagulate the tissue was used to predict the thermal dose (in equivalent minutes at $43°C$ [32]:

$$TD_{43} = \int_{t=t_{final}}^{t=0} R^{43-T(t)} dt \tag{2.13}$$

where TD is the thermal dose which relates the time required for coagulating the tissue at temperature T to the equivalent time at TD_{43}. The size of the necrosis is calculated based on the threshold value of 240 min at $43°C$ [33].

$$R = \begin{cases} 0.5 & T(t) > 43°C \\ 0.25 & otherwise \end{cases} \tag{2.14}$$

Chapter 3

Optimal Refocusing Through the Rib Cage Using Semidefinite Relaxation Method

3.1 Introduction

The use of HIFU in thermal therapy applications of tumors and other tissue abnormalities is on the rise due to improved real-time image guidance and improved transducer technology. Targets accessible to appropriately designed HIFU transducers (e.g. uterine fibroid and prostate) have been successfully treated under MRI and ultrasound guidance using commercially available systems. However, tumors in organs partially obscured by the ribs (e.g. liver tumors) represent a challenge for extracorporeal HIFU as shown in Fig. 3.1. The ribs in the path of the HIFU beam path produce strong aberrations and attenuation in addition to strong scattering. This results in a loss of power at the focus as well as an increase in the risk of damage to the ribs and overlying tissues.

The use of phased array technology in HIFU applications allows for the pursuit of optimal driving signal distributions for thermal therapy applications (e.g. multiple-focus patterns conforming to the tumor geometry as was shown in [10].) The optimization problem can also be defined more generally to include other constraints like minimizing the exposure to the ribs and other critical structures in the path of the HIFU beam

[34]. Several groups have investigated the transcostal refocusing of phased arrays in recent years. A two-step hybrid virtual array (VAR) method [34] has been used for the analysis and synthesis of multiple focused phased array heating patterns in the presence of strongly scattering obstacles. In [35], a one-step optimization algorithm to maximize the array intensity gain at the target while minimizing it across critical points by using regularized minimum norm least squares solution has been shown. Another group [36] studied the effect of removing the contribution of the edge segments, using a linearly segmented transducer, from one side of the transducer to the field. In [37], Aubry *et al* presented an experimental verification of transcostal focusing based on previously described time reversal acoustics methods [38, 39, 40, 41, 42, 43]. In [44], Ballard *et al* demonstrated an image-based approach to transthoracic refocusing using a dual-mode ultrasound array (DMUA) prototype described in [45]. The problem was also addressed by Ter Haar and coworkers to shed some light on the scattering by the human ribs [46, 47].

In [48], Khoklova and coworkers performed numerical and experimental studies that demonstrated the improved focusing when the effects of diffraction are taken into account compared to a geometric ray tracing approach. They reported 23% increase in focusing gain and significant reduction in power losses on the ribs (1% vs 7.5%) when using the diffraction-based approach. The diffraction-based optimal solution utilized the pseudo-inverse multiple-focus synthesis method described earlier [49] and supporting the results of the simulation study in [34] and the experimental study in [44]. Taken together, these studies highlight the fact that optimization of the phased-array beam patterns can help improve the safety and efficacy of transcostal HIFU. The optimal solutions described in our previous studies were designed based on minimizing the power deposition to the ribs (MPD) for a specified focusing gain (constraint.) The Lagrange multiplier method was used to find a weighted minimum-norm (minimum-energy) least squares solution to the optimization problem. With the advent of optimization methods, it is possible to reformulate the refocusing problem in a way that further enhances the safety and efficacy of transcostal refocusing of HIFU beams. In this chapter, we present an optimal refocusing algorithm that seeks a minimum-energy solution with specified focusing gain at the target while allowing for a "controlled" level of exposure to the ribs and a maximum sidelobe level in the target (focal) plane. This method we will name it the limited power deposition (LPD) method. The motivation for specifying maximum exposure to the ribs is to directly address the safety issue in terms of collateral damage to ribs or the surrounding tissue. The motivation for specifying maximum acceptable sidelobe level is that previous solutions produced peaks sidelobes related to the rib geometry which could be objectionable when steering the focus. Specifying the maximum sidelobe level also addresses the collateral damage to the tissues surrounding the target. Unfortunately, the design optimization accounting specifically to partial transmission through the ribs and maximum sidelobe level is a non-convex NP-hard computational problem. However, it was recently shown how convex approximation can be adapted to work in this context [50, 51]. In particular, a semidefinite relaxation approximation to the optimization problem [51] is the performance of the new optimization approach is validated in a simulation study utilizing finite-difference time-domain (FDTD) modeling of acoustic propagation and the transient bioheat equation in inhomogeneous media. The FDTD model of the wave equation utilizes the perfectly matching layer (PML) for the absorbing boundary condition as described in [30]. The BHTE simulations were performed as previously described [52, 53] and were used to confirm the improvement in the therapeutic gain achieved by the new algorithm compared to previously published methods [34, 44].

The optimization approach is described as:

- Minimization of the total transmit power subject to constrain on the energy deployed at the
    - Target (focal points)
    - Obstacles (ribs)
    - Side lobe locations

3.2 Problem Statement

3.2.1 Refocusing Algorithm

Our optimization approach is based on finding the array excitation vector with minimum energy that simultaneously maximizes the power deposition at the target while

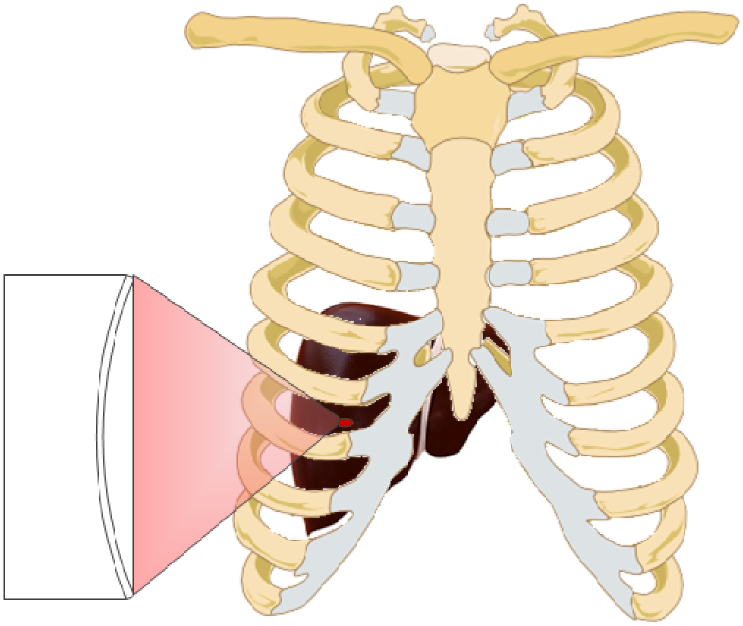

Figure 3.1: Medical explanation showing a HIFU beam targeting a tumor in the liver

minimizing the exposure to the ribs and controlling the maximum sidelobe power deposition in the focal plane. We solve a problem for designing a refocusing method to minimize the transmission power at the phased array given upper bound constraint on the ribs and the side lobe locations and a prescribed constraint at the target. This approach differs from previously proposed optimization procedures (e.g. [34]) in two aspects. First, it allows for "acceptable" level of exposure to the ribs and accounts for partial transmission through the ribs. Second, it specified the maximum sidelobe level in the focal plane. Consider the phased array with N elements and L target points. Let h_{ti}, h_{rj} and h_{sq} denotes the $N \times 1$ complex vectors that models the directivity, which is described later on this chapter, from N transmit elements of the phased array to the points $i \in \{1, ..., L\}$, $j \in \{1, ..., M\}$, and $q \in \{1, ..., K\}$ respectively. The t stands for the target, r stands for the ribs and s stands for side lobe. let $\mathbf{u}$ stands for the complex array excitation vector, $\mathbf{p}_{ti}$ is the prescribed exposure power at the targets, $\mathbf{p}_{rj}$ is the max threshold power at the ribs and $\mathbf{p}_{sq}$ is the upper bound power level at the side lobe locations. The problem of designing the refocusing method, which minimize the transmit power at the phased array given upper bound constraint on the ribs and side lobes in addition to a prescribed constraint at the target, can be mathematically described as:

$$\boxed{\begin{array}{lll} \min\limits_{\mathbf{u}\in\mathbb{C}^N} & ||\mathbf{u}||_2^2 & \\ \text{s.t. :} & |\mathbf{u}^{\mathcal{H}}\mathbf{h}_{ti}|^2 \geq \mathbf{p}_{ti}, & i = 1, \ldots, L \\ & |\mathbf{u}^{\mathcal{H}}\mathbf{h}_{rj}|^2 \leq \mathbf{p}_{rj}, & j = 1, \ldots, M \\ & |\mathbf{u}^{\mathcal{H}}\mathbf{h}_{sq}|^2 \leq \mathbf{p}_{sq}, & q = 1, \ldots, K. \end{array}} \tag{3.1}$$

This kind of optimization problem belong to the class of quadratic constraints quadratic programming (QCQP) problem [50],[54], the first constraints are concave homogeneous quadratic constraints resulting in a non-convex optimization problem, which is known to be NP-hard for directivity vectors [51]. $||\cdot||_2^2$ stands for the Euclidean norm of a vector while $\mathcal{H}$ for the hermitian. Also any bold high case letter through the chapter denotes for a matrix. This optimization problem assumed that we have a prior knowledge of the directivity vectors $\mathbf{h}_{ti}, \mathbf{h}_{rj}$ and $\mathbf{h}_{sq}$,which can be accomplished through a direct measurements [55], a computational model for wave propagation in inhomogeneous media [42], [56], [57] or an estimation from the beamforming parameters used in forming single transmit focus (STF) or synthetic aperture (SA) imaging [44].

3.2.2 Semidefinite Relaxation Approximation

The problem stated in (3.1) is not always feasible, The feasibility is geometrically defined as the intersection of the exteriors L co-centered ellipsoids and the interiors of M and K co-centered ellipsoids [58] which may turn out to be empty resulting in infeasible problem. The problem is defined as NP-hard which can be relaxed to a convex problem using semidefinite relaxation programming (SDR) approach [51], [59]. Define $\mathbf{Q}_i = \mathbf{h}_{ti}\mathbf{h}_{ti}^{\mathcal{H}}$, $\mathbf{F}_j = \mathbf{h}_{rj}\mathbf{h}_{rj}^{\mathcal{H}}$, $\mathbf{Z}_q = \mathbf{h}_{sq}\mathbf{h}_{sq}^{\mathcal{H}}$, and $\mathbf{X}_i \triangleq \mathbf{u}\mathbf{u}^{\mathcal{H}}$ and using the identities:

$$\begin{aligned} ||\mathbf{u}||_2^2 &= tr(\mathbf{u}\mathbf{u}^{\mathcal{H}}) \\ |\mathbf{u}^{\mathcal{H}}\mathbf{h}|^2 &= \mathbf{h}^{\mathcal{H}}\mathbf{u}\mathbf{u}^{\mathcal{H}}\mathbf{h} \\ &= tr(\mathbf{h}^{\mathcal{H}}\mathbf{u}\mathbf{u}^{\mathcal{H}}\mathbf{h}) \\ &= tr(\mathbf{h}\mathbf{h}^{\mathcal{H}}\mathbf{u}\mathbf{u}^{\mathcal{H}}) \end{aligned}$$

where $tr(.)$ denotes the trace operator. Given that $\mathbf{X}$ is an $N \times N$ complex matrix, "$\mathbf{X} \succcurlyeq 0$" ($\mathbf{X}$ is symmetric positive semidefinite) and rank($\mathbf{X}$)=1 (not always the case), we can strictly define $\mathbf{X} = \mathbf{u}\mathbf{u}^{\mathcal{H}}$. The SDR approach can be mathematically described, after dropping the non-convex rank constraint rank($\mathbf{X} = 1$), as:

$$\boxed{\begin{array}{lll} \displaystyle\min_{\mathbf{X}\in\mathbb{C}^{N\times N}} & tr(\mathbf{X}) & \\ \text{s.t. :} & tr(\mathbf{X}\mathbf{Q}_i) \geq \mathbf{p}_{ti}, & i = 1, \ldots, L \\ & tr(\mathbf{X}\mathbf{F}_j) \leq \mathbf{p}_{rj}, & j = 1, \ldots, M \\ & tr(\mathbf{X}\mathbf{Z}_q) \leq \mathbf{p}_{sq}, & q = 1, \ldots, K \\ & \mathbf{X} \succcurlyeq 0 & \end{array}} \tag{3.2}$$

In (3.2), the objective function is linear in $\mathbf{X}$, and the trace constraints are linear inequalities of $\mathbf{X}$. In addition, the set of symmetric positive semidefinite matrices is

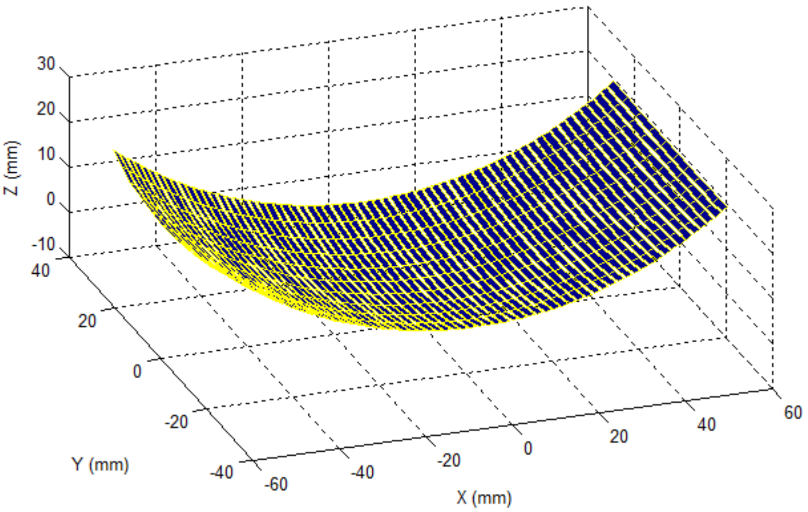

Figure 3.2: 64-element DMUA diced in Y direction to form a rectangular elements for directivity computations, temperature and field simulations.

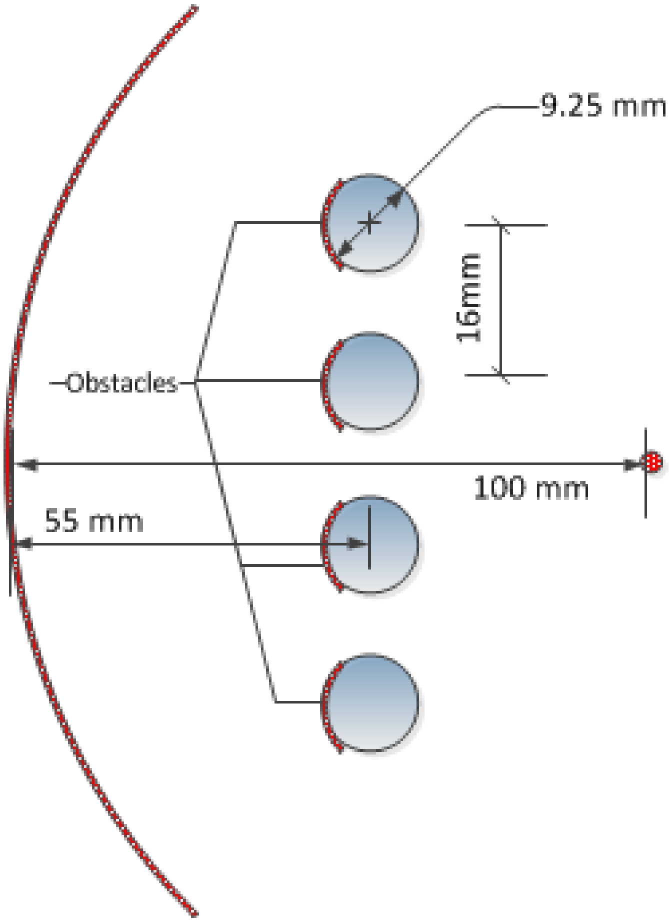

Figure 3.3: Geometric description of the simulated domain

convex [51], [60]. We now obtain the convex optimization problem which can be solved using interior point methods [61], [62] and a Matlab toolbox `SeDuMi` [63] and `yalmip` [64] used as an implementation of the modern interior point methods for SDR. This relaxation is the closest convex problem to the non-convex problem mentioned earlier.

3.2.3 Randomization Algorithm

As a consequence of dropping the rank one constraint, the optimal solution ($\hat{\mathbf{X}}$) obtained from solving the SDR in (3.2) might not be rank one. Hence, it results in two cases: rank($\mathbf{X}$) $= 1$ or rank($\mathbf{X}$) > 1. We can recover our solution in the first case by finding its principle component which defined as the principle eigenvector corresponding to the only one nonzero eigenvalue. In the second case, we have to solve a randomization approach [51],[60] to get an approximate solution of the original problem (3.1) from the relaxed version solution [50], [54] and choose the excitation vector that yields the minimum total power and also satisfy the constraints. When the excitation vector $\mathbf{u}$ violates any of the ($\geq$) constraints in (3.1), it should be scaled up by a factor as described in [60] to guarantee the satisfaction of the power deposition at the ($\geq$) constraints. After the scaling up, we also have to check the satisfaction of the ($\leq$) constraints. If any of the constraints is violated, the particular scaled up excitation vector is discarded and a new round of the randomization techniques is started. Finally, we choose the excitation vector that holds the minimal norm among all possible solutions. This search is close to the concept of brute-force, exhaustive search.

3.3 Directivity Calculations

Single or multiple-focus HIFU patterns can be synthesized using appropriately designed phased arrays when the element directivity values at the focus location(s) are known [49]. Acoustic field patterns are generated by specifying the amplitude and phase of the ultrasound beam at a set of N_c control and N_t target points. The propagation of an ultrasound wave of unit amplitude from each of N elements of the array to each control point, is stored in the $M \times N$ matrix $\mathbf{H}_c$ and $L \times N$ matrix $\mathbf{H}_t$. The complex pressure at a point in the field due to continuous wave source is given by the Rayleigh-Sommerfield integral [49],[52]:

$$\boxed{p(r) = \frac{j\rho c\kappa}{2\pi}\int_S \mathbf{u}(\acute{r})\frac{e^{-j\kappa|r-\acute{r}|}}{|r-\acute{r}|}\,dS}$$

Where ρ and c are the density and the speed of sound in the medium respectively, $\kappa = \frac{\omega}{c}$ is the wave number , S is the surface of the source, $\mathbf{u}$ is the particle velocity normal to the surface of the source, r and $\acute{r}$ are the observation and source points respectively. We can tolerate the previous equation to work for an N elements array having arbitrary geometry as:

$$\boxed{p(r) = \frac{j\rho c\kappa}{2\pi}\sum_{n=1}^{N}\mathbf{u}_n\int_S \frac{e^{-j\kappa|r-\acute{r}_n|}}{|r-\acute{r}_n|}\,dS_n}$$

Where S_n and $\mathbf{u}_n$ are the surface and the particle velocity of the n^{th} element of the array and $\acute{r}_n$ represents points on the n^{th} element of the array. If the complex pressure is specified at C control points, we can write

$$\boxed{p(r) = \frac{j\rho c\kappa}{2\pi}\sum_{n=1}^{N}\mathbf{u}_n\int_S \frac{e^{-j\kappa|r_c-\acute{r}_n|}}{|r_c-\acute{r}_n|}\,dS_n}$$

The complex pressure at a point in the field due to continuous wave source [49],[52] can be expressed in matrix form as:

$$\mathbf{H}_t\mathbf{u} \;=\; \mathbf{p} \tag{3.3}$$

where $\mathbf{u}$ is $N \times 1$ is complex array driving vector and $\mathbf{p}$ is $L \times 1$ vector denoting the complex pressures at the control points in the field and $\mathbf{H}_t$ is the forward propagation operator.

$$\boxed{H(m,n) = \frac{j\rho c\kappa}{2\pi}\int_A \frac{e^{-j\kappa|r_c-\acute{r}_n|}}{|r_c-\acute{r}_n|}\,dA_n} \tag{3.4}$$

3.3.1 Comparison with MPD Method

The refocusing excitation vectors are obtained by solving a constrained optimization problem that minimizes the direct incidence of acoustic power at the ribs. The objective is to maximize the array intensity gain at a target point while minimizing the incident power at a set of critical points. let $\mathbf{H}_t = [\mathbf{h}_{t1}^T; \mathbf{h}_{t2}^T; \ldots; \mathbf{h}_{tL}^T]$ be the array directivity vector at target and let $\mathbf{H}_r = [\mathbf{h}_{r1}^T; \mathbf{h}_{r2}^T; \ldots; \mathbf{h}_{rM}^T]$ where L, M and T refer to the number of targets, critical points and transpose, respectively. This problem can be mathematically described as follows:

$$\boxed{\begin{array}{ll} \min\limits_{\mathbf{u} \in \mathbb{C}^N} & \mathbf{u}^{\mathcal{H}} \mathbf{W}_r \mathbf{u} \\ \text{s.t.}: & ||\mathbf{H}_t \mathbf{u} - p||^2 = \epsilon \end{array}} \tag{3.5}$$

with the weighting matrix

$$\mathbf{W}_r = [\mathbf{H}_r^{\mathcal{H}} \mathbf{H}_r + \gamma I]$$

This is an optimization problem that can be solved using Lagrange multipliers utilizing the pseudoinverse method, where I is the identify matrix and γ is the smallest nonzero singular value resulting from the singular value decomposition of $\mathbf{H}_r$. This leads to an optimal complex array driving vector given by:

$$\mathbf{u} = \mathbf{W}_r^{-1} \mathbf{H}_t^{\mathcal{H}} (\mathbf{H}_t \mathbf{W}_r^{-1} \mathbf{H}_t^{\mathcal{H}})^{-1} p_o$$

where p_o is the specified complex pressure at the target. For a single target, p_o is a scalar and $\mathbf{H}_t$ will be a row vector.

3.4 Materials and Method

3.4.1 Ultrasound Array

We have simulated a 1-MHz, 64-element array with a concave aperture with 100-mm radius of curvature. This array geometry is the same as our dual-mode array prototype described in [44]. The array geometry shown in Fig. 3.2 with the element segmentation in the elevation (Y) direction is only for computational purposes, i.e. the 64 elements

Table 3.1: Acoustic and Thermal values for the medium

Type	Density kg/m^3	Specific Heat $J./kg.°$C	Thermal Conductivity $W.m^{-1}/°$C	Speed of Sound m/s	Attenuation (α) $dB/cm/MHz$
Medium	1090	3540	0.52	1500	0.94
Simulated ribs	1800	1300	0.32	2800	4

are linearly distributed in the lateral (X) direction. The center-to-center spacing is 2 mm with a kerf of 0.5 mm. The element height is 50 mm.

3.4.2 Model Description

The propagation medium was modeled as a tissue-like material and the proposed method is simulated on the rib cage using a simulation model of four ribs (9.25 mm in diameter each) separated by 16 mm. This is shown in the geometry of the domain including the position of the scattering obstacles used in this simulation study as in Fig. 3.3. The medium and the simulated ribs follow the acoustic and thermal values in table 4.2 .

3.4.3 Numerical Model

This chapter demonstrates the feasibility of generating focused pattern in the rib cage. However, a more realistic computational model is needed with actual geometry and operating conditions. We need to predict field and temperature numerical techniques accurately within the computational domain. Numerical methods are used to compute an unknown scalar or vector function of position and time at the nodes of a structured grid of the solution domain that satisfies the required partial differential equations (PDE). This model is used to simulate the propagation of the ultrasonic pulses and the temperature field achieved to ensure adequate thermal treatment without any harm to the ribs. The model is based on the wave equation and the bio heat transfer equation (BHTE). A finite difference approximation of partial derivatives are required in the numerical solution of the PDE, it provides us with the required expressions for the function partial derivative in terms of function values at a number of neighboring grid nodes. We have to apply well established finite difference formulas to approximate temporal and spatial derivatives in the PDE to increase the consistency. The finite difference method is consistent if the difference between the modified differential equation and the PDE has terms that are proportional to powers of the time step and grid spacings.

The finite difference equation is applied at interior and boundary nodes. In certain cases, it is important to extend the solution domain beyond the natural boundaries of the physical problem to improve the expressing of the boundary condition.

The FDTD method [28] is a powerful tool for solving a broad range of PDE. It is used to analyze the HIFU field and temperature rise throughout the therapeutic region. This numerical simulation is providing all the information needed after refocusing the beam in inhomogeneous medium and is necessary to achieve a treatment plan before the actual treatment gets into place. This propagation of focused acoustic wave in a tissue as described earlier in the wave equation :

$$\boxed{\begin{aligned} \frac{\partial \mathbf{v}}{\partial t} &= \frac{-1}{\rho}\nabla p \\ \frac{\partial p}{\partial t} &= -\rho.c^2\nabla.\mathbf{v} + \alpha p \end{aligned}}$$

where $\mathbf{v}$, p, and c, denote the particle velocity, pressure and speed of sound respectively. The absorption coefficient α is used as an indication of the absorptive loss in the medium. The spatial and temporal partial derivatives are approximated by a Taylor series expansion for each node in the computational grid, this grid consists of a spatial dimensions using uniform spacing in addition to temporal dimension $\triangle t$ with uniform spacing. We have to artificially use boundary conditions in finite difference methods to extremely decrease the reflection caused by the edges of the computational domain. A perfect matched layer as a material absorbing boundary condition (ABC) [30] were applied at the computational edge of the grid to eliminate the reflections from the outer boundary of the computational domain. A higher absorption is achieved by using PML as absorbing boundary condition.

As an acoustical signal propagates, some of the energy is absorbed in the tissue leading to temperature increased which can be modeled by the BHTE used to governed the thermal effects in tissue.

$$\boxed{\rho C_t \frac{\partial \mathbf{T}}{\partial t} = k\nabla^2 T - W_b C_b (T - T_b) + Q}$$

Where T is the tissue temperature, T_b is the arterial blood temperature, ρ is the tissue density kg/m^3, C_t is the specific heat of tissue $(J/kg.)$, C_b is the specific heat of blood, k is the thermal conductivity of the tissue (W/m), Q is the applied intensity deposited by an external applicator (W/m^3), W_b is the perfusion parameter (kg/m^3s).

A Forward-Time Central-Space (FTCS) discretization scheme has been used. More specifically, a forward difference for the time derivative and a centered difference for the second spatial derivative as:

$$\boxed{\begin{aligned} \rho C_t \left[\frac{T^{n+1}_{i,j,l} - T^{n}_{i,j,l}}{\triangle t}\right] &= \\ k \left[\begin{array}{cc} \frac{T^n_{i+1,j,l} - 2T^n_{i,j,l} + T^n_{i-1,j,l}}{\triangle x} & + \\ \frac{T^n_{i,j+1,l} - 2T^n_{i,j,l} + T^n_{i,j-1,l}}{\triangle y} & + \\ \frac{T^n_{i,j,l+1} - 2T^n_{i,j,l} + T^n_{i,j,l-1}}{\triangle z}) & \end{array}\right]& \\ -W_b C_b (T_a - T^n_{i,j,l})& \\ +Q& \end{aligned}}$$

The accuracy of the FDTD depends on the size of the space grid and the time step, the method is consistent as the accuracy increase.

The numerical error is on the order of $\triangle t$ and $\triangle x$. In order to meet the stability criteria, the temporal step has followed the Courant, Friedrichs and Lewy (CFL) condition [31] for the convergence of a difference approximation in terms of the concept of the domain of dependence of the partial differential equation (PDE).

3.5 Simulation Results

Simulations were performed at 1 MHz using a 64-element phased array described in [45] and [44]. The acoustic and thermal simulation parameters are shown in table 4.2. For acoustic simulations, the simulation grid spacing was set to 0.15 mm (one-tenth of the wavelength in water.)

The performance of the optimization methods is illustrated by focusing the 64-element array at one target point in the presence of the four Plexiglas ribs as illustrated in Fig. 3.3. For the LPD method, an optimal solution was sought by using the desired intensity at the target as a constraint and specifying the maximum exposure to the ribs together with the maximum acceptable sidelobe in the focal plane. The resulting array excitation vector (magnitude and phase) are shown in Fig. 3.4. For the MPD method, an optimal solution was sought by using the desired intensity at the target as a constraint and solving a Lagrange multiplier problem to minimize exposure to the ribs [49, 34]. The resulting array excitation vector (magnitude and phase) are shown in Fig. 3.5. Examining the two solutions, one can see that both exhibit a spatial modulation which reflects the presence of the obstacles. However, both utilize the full aperture of the array, even the elements that reside in the shadow of a point source located at the target. Our studies have shown that the excitation of these elements helps in the optimization in two ways:

1. They create destructive interference over the ribs to help minimize the exposure.
2. These elements can also contribute to the power deposition in the focal plane due to the limited shadow region behind the ribs.

It is therefore not surprising that both optimization methods utilize these elements to provide additional degrees of freedom in finding the optimal solution.

Figures 3.6 and 3.7 show the 2D intensity patterns resulting from the LPD and MPD optimal solutions, respectively. The general behavior of both solutions can be observed from these profiles. Specifically, both methods produce a well-defined focal spot at the target by shaping the acoustic wavefront in a manner that maximally utilizes the intercostals. The differences between the two results are in the details of the sidelobes in the target plane and the level of exposure to the ribs as illustrated below.

Fig. 3.8 shows the intensity profiles in the focal plane achieved by the LPD method (solid) and MPD method (dashed.) All intensity values are normalized to the maximum (achieved by the LPD method) in the target plane. This normalization was based on assuming that the array excitation vectors are normalized to the same maximum. based on this normalization, one can see that the LPD produced an intensity pattern with approximately 50% increase in intensity gain compared to the MPD solution. In

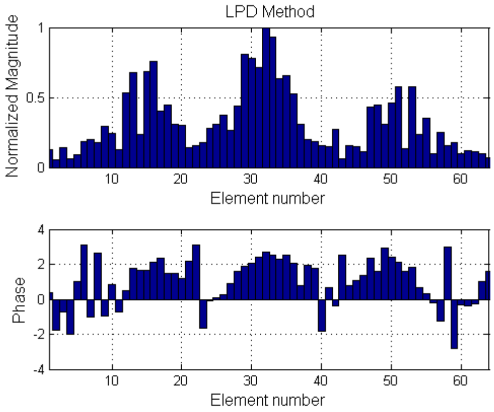

Figure 3.4: Complex excitation distribution vector of the feed array using the LPD method, (Top) Relative magnitudes, (Bottom) relative phases.

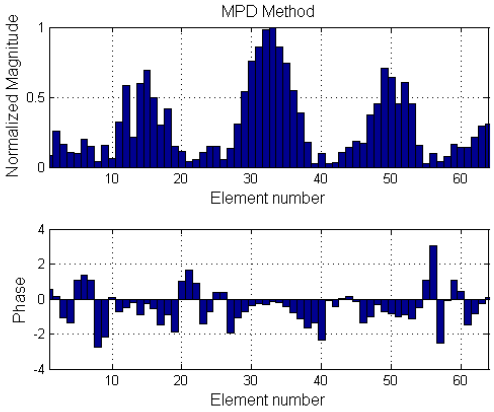

Figure 3.5: Complex excitation distribution vector of the feed array using the MPD method, (Top) Relative magnitudes, (Bottom) relative phases.

addition, the LPD solution also produces more balanced sidelobes owing to the fact that the optimization problem was solved for a specified peak sidelobe level. On the other hand, the sidelobe level was not constrained in the MPD optimization.

The normalized intensity profiles distal to the rib plane are shown in Fig. 3.9, which illustrates the wavefront shaping property of both optimization algorithms. The three peaks correspond to the intercostals between the ribs as expected. Both intensity profiles are well-behaved, but sufficiently different. This difference between them reflects the fact that the optimization problems are able to find a unique solution among the infinite number that meets the constraint at the target (or when the number of targets is less than the number of array elements.)

To illustrate the difference between the two optimal solutions on the temperature response in the target plane and in the vicinity of the ribs, we solved the inhomogeneous transient bioheat equation for five-second exposure using the thermal properties shown in Table 4.2. Figure 3.10 shows the temperature profiles in the focal plane for the LPD solution (solid) and MPD solution (dashed.) These profiles smoothed versions of the intensity profiles shown in Fig. 3.8 as expected due to the lowpass nature of the BHTE. They also show that the increased intensity gain achieved by the LPD solution achieve an increase of temperature rise at the target compared to the MPD solution. The behavior of the temperature profiles distal to the rib plane (Fig. 3.11) are also consistent with the intensity profiles shown in Fig. 3.9.

To further illustrate the well-behaved nature of the optimal solutions, Fig. 3.12 shows the temperature profiles in two additional planes in the vicinity of the ribs. The figure demonstrates that both solutions result in well-behaved temperature profiles in the vicinity of the ribs, both near the skin and below the ribs in the viscera. These results demonstrate clearly that the new formulation results in well-behaved intensity fields and temperature patterns suitable for thermal therapy in transthoracic refocusing applications.

The results illustrated by the case shown above are generally true for a variety of target locations, even when the focusing gain of the array suffers due to the presence of the obstacles. We have run simulations by placing the target at different positions with respect to the ribs. To compare between these cases, we use the ratio between the temperature at the target and the peak temperature in a plane of interest [44]. This

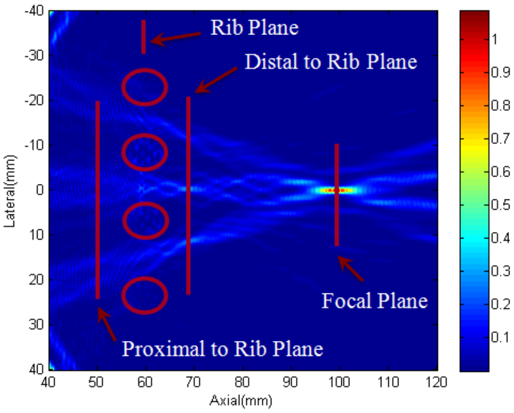

Figure 3.6: Simulated field intensity pattern for the LPD method.

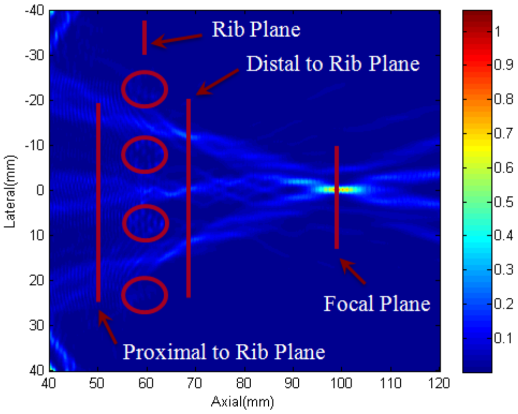

Figure 3.7: Simulated field intensity pattern for the MPD method.

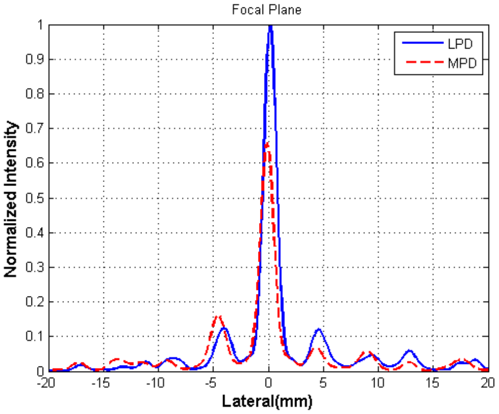

Figure 3.8: Simulated field intensity pattern in the focal plane for the LPD method (solid line), MPD method (dashed line).

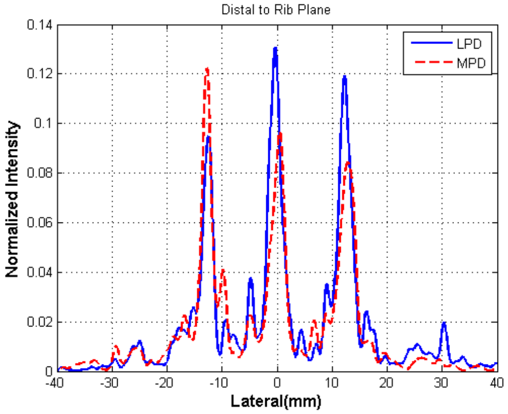

Figure 3.9: Simulated field intensity pattern in a distal-to-the-rib plane for the LPD method (solid line), MPD method (dashed line).

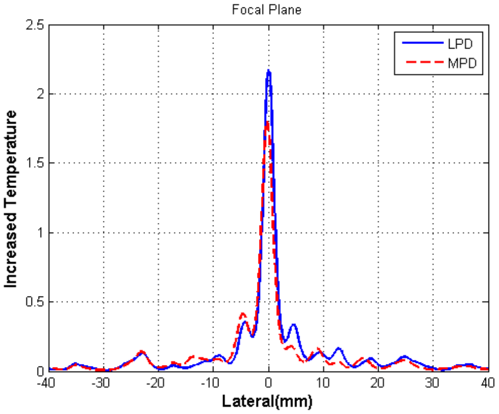

Figure 3.10: Simulated temperature pattern at the focal plane for the LPD method (solid line), MPD method (dashed line).

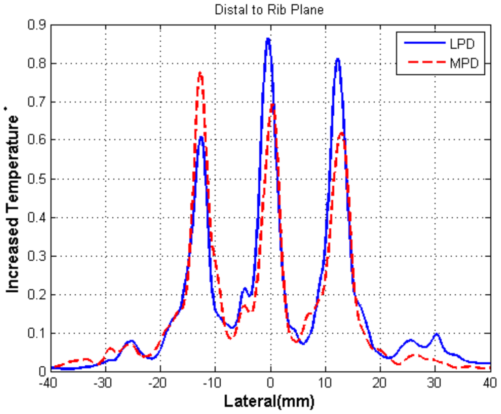

Figure 3.11: Simulated temperature pattern distally to the rib plane for the LPD method (solid line), MPD method (dashed line).

Table 3.2: Target to rib temperature

Method (x_t, z_t)	T_T/T_{PR}	T_T/T_R	T_T/T_{DR}
MPD (0,100)	11	4.29	9.77
LPD (0,100)	12.94	5.78	10.47
MPD (5,100)	2	4.63	4.4
LPD (5,100)	2.09	7	6.4
MPD (10,100)	1.47	2.38	3.57
LPD (10,100)	1.5	6	6

ratio is a measure of the therapeutic gain and is more useful than the intensity gain from the application point of view. This ratio, T_R/T_{CP} gives a measure of heating efficiency at the target with reference to a critical plane (e.g. the rib plane) for a given heating protocol. Table 3.2 shows a summary of performance for three target locations near the array geometric center but with significant difference in shadowing. The results show that the LPD solution either meets or exceeds the performance of the MPD solution in every case and throughout the vicinity of the ribs.

3.6 Discussion

The simulation results presented in this chapter provided validation of a new optimization algorithm to the problem of transthoracic targeting of abdominal targets, e.g. liver tumor. Inhomogeneous acoustic field (4.3.1) and temperature (4.2) models were used to demonstrate the applicability of the optimization algorithm in realistic situations. The use of a realistic computational model also allowed us to provide intensity and temperature profiles throughout the treatment region including the rib plane and areas proximal to it, which is difficult to achieve experimentally [44].

Compared to our previous results addressing the transthoracic focusing in [34], the approach described in this chapter takes the partial transmission through the ribs into account in the inverse problem as well as the field computation. The optimization approach described in [34] simply attempted to minimize the exposure to the ribs. The approach described in this chapter solves the optimization problem allowing for a specified level of exposure to the ribs. A direct consequence of this additional degree of freedom is the ability to better control the sidelobe distribution in the target plane

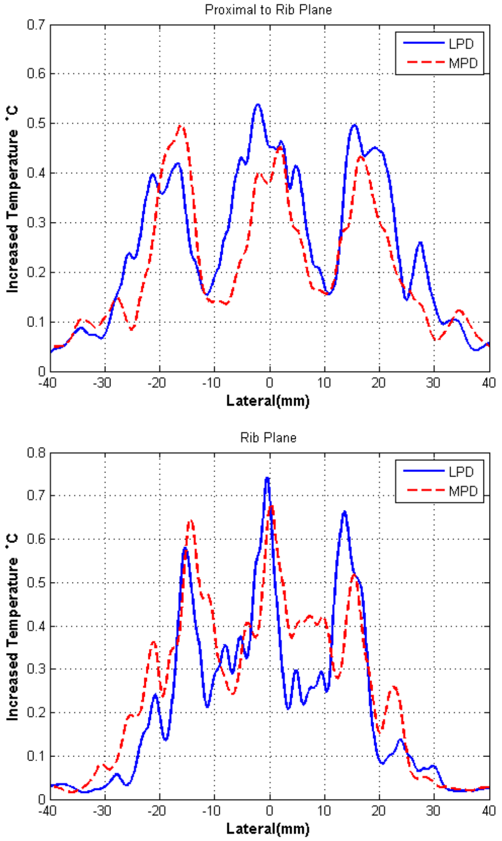

Figure 3.12: Simulated temperature profiles proximal to (top) and within (bottom) the rib plane.

as can be seen in Fig. 3.9. In this case, the sidelobes resulting from the LPD method are relatively lower and more balanced than the peak sidelobe resulting from the MPD formulation. The LPD and the MPD methods utilized for solving the optimization problem demonstrate the need for optimal synthesis when refocusing in the presence of obstacles. A key observation that can be made based on the resulting complex excitation vectors (Figs. 3.4 and 3.5) is that all the array elements are being utilized. It can be easily shown that the naïve solution of switching off array elements based on tray tracing from the target to the array surface results in an inferior solution to what is presented here. The phase and magnitude profiles resulting from both methods are well-behaved and are easily implemented using phased array drivers like the one used to generate the experimental results shown in [45] and [44] (0.67% amplitude quantization and 1.2° phase quantization at 1 MHz.)

We have simulated a variety of target locations and used both optimization methods to assess the therapeutic gain with respect to the rib plane. The relative advantage enjoyed by the LPD over the MPD algorithm generally hold. Table 3.2 shows the temperature ratios in the rib plane and two planes proximal and distal to it as illustrated in Fig. 3.7. These results illustrate that the LPD solution generally produces field patterns with higher therapeutic gain than the MPD solution.

3.7 Conclusion

A new optimization approach to the transthoracic refocusing problem was presented together with validation results based on realistic acoustic and temperature simulation models. The optimization algorithm accounts for the rib plane geometry to reshape the acoustic wavefront in a manner favoring the transmission through the intercostals and achieves “controlled” exposure to the ribs as it maximizes the power deposition at the target(s). Explicitly accounting for the partial propagation through the ribs demonstrates the advantage of achieving a higher degree of control of the field pattern in the target plane. In particular, we have shown that the LPD method produces a solution with better behaved sidelobes compared to the MPD solution. Furthermore, the LPD solution generally results in higher therapeutic gain compared to the MPD solution. These gains are achieved while utilizing realizable phase and amplitude distributions with existing array drivers. This approach can also make use of elements cancelation by adding the L1-norm squared which induces sparsity useful in imaging application [65].

Chapter 4

Image Based Numerical Simulation Of HIFU Induced Lesion

4.1 Introduction

Atherosclerosis is a systemic disease that affects large and medium sized arteries. The disease starts as an endothelial dysfunction which initiates recruitment of inflammatory cells and lipids within the arterial wall [66]. This, together with smooth muscle hyperplasia, leads to the development of slowly growing atherosclerotic plaques that become clinically symptomatic when they cause significant hemodynamic stenosis. HIFU beams can be precisely focused within small focal volume, resulting in a rapid rise of the local tissue temperature. This temperature elevation causes localized tissue damage through coagulative necrosis [67, 68, 69, 70]. With proper choice of operating frequency and transducer design, this can be achieved without significant biological damage to the intervening tissue. The advent of image guidance modalities like MRI and ultrasound has allowed for completely noninvasive thermal therapy procedures [71, 72, 73, 74]. Different applications of image guided HIFU therapy for potential medical applications have been proposed [75, 76] in addition to a computational model for ultrasound tomography [77]. The computational modeling of these therapies has become an important research tool, allowing physician to improve monitoring during treatment procedure and prediction of thermal lesion before treatment which would be of great benefit in treatment planning. Several numerical models already exist for simulation of the treatment process and predicting the outcomes of some other procedures [78, 79]. In addition, some groups studied the nonlinear thermal effect of the wave propagation [80, 81, 82] and the vascular damage induced by ultrasound [83, 84]. Several guidelines currently exist for treatment of atherosclerosis, including medical, surgical and interventional treatments [85]. We have been investigating the use of HIFU to target localized atherosclerotic plaques in-vivo. We demonstrated the feasibility of inducing HIFU thermal lesions within atheromatous plaques in the femoral arteries of Familial Hypercholesterolemic (FH) Swine in vivo [86]. One of the most important conclusions of this study is that it is possible to form a thermal lesion within the plaque tissue without damage to the endothelial cells. This is most probably due to the heat sink effect of the blood flow in the artery, which resulted in a thin ($\sim$ 200 micrometer) layer of protected tissue (endothelium and part of the tunica intima). Imaging and histological studies of peripheral vessels in the FH swine model have clearly demonstrated the heterogeneity of the tissues surrounding the target plaque tissue [86]. The HIFU beam goes through regions of skin, fat and muscle in addition to the connective tissue around the vessel. These studies also showed that diagnostic ultrasound, when carefully administered before treatment can produce sufficient anatomical contrast to differentiate between these tissue types. This information can be used to define a heterogeneous propagation model for the HIFU beam and a heterogeneous model for the transient bioheat transfer equation (tBHTE). Furthermore, the arteries and veins in the treatment region can be easily identified on a diagnostic ultrasound. This provides an opportunity to account for their effect on the resulting heating patterns. The availability of a realistic numerical model for the HIFU propagation and temperature evolution in the presence of tissue heterogeneity and directional blood flow would be highly advantageous for the potential treatment of atherosclerotic plaques. It provides an opportunity for pretreatment planning to allow for treatment optimization. It also allows for retrospective analysis of the treatment results to help the physician decide post treatment protocol. In this chapter we present results from a heterogeneous acoustic and thermal model derived from pretreatment ultrasound images of the treatment region. In addition to the tissue heterogeneity, the thermal model contains a convective term accounting for blood flow in the target vessel. Both models utilize the finite difference time-domain (FDTD) discretization of their respective partial differential equations (PDE). The model geometry is obtained based on an image segmentation of a pretreatment ultrasound of the target region. The model accounts for the water bolus, skin, fat, muscle, and connective tissue in addition to target vessel lumen. The acoustic and thermal properties of the different tissues within the treatment region are obtained from the literature. Two simulations of actual HIFU treatments targeting the femoral artery in the FH swine model are presented in this chapter. In one scenario, the model showed that all attempted HIFU shots formed produced lesions at the intended target plaque without damage to the endothelium or intervening tissue in the path of the HIFU beams. In the second scenario, the model predicted a prefocal lesion near a vessel in the path of the HIFU beam. In both cases, the model predictions were consistent with histological evaluations of the treated regions.

4.2 Materials and Method

4.2.1 Ultrasound Pretreatment Imaging

A conventional diagnostic ultrasound imaging (Sonix RP: Ultrasonix. Richmond, British Columbia, Canada) was conducted through the 7.2-MHz diagnostic transducer (L14-5/38: Ultrasonix) to visualize the artery and the plaque. This was also performed to collect data regarding the depth and the diameter of the artery in addition to the thickness of subcutaneous fat region. The full study was described at [86].

4.2.2 Integrated Dual-mode Ultrasound Array (DMUA) System for Image-guided Lesion Formation

The DMUA system described in [87] was used for targeting the femoral artery in the FH swine model. The integration of both the diagnostic imaging transducer and the concave transducer create the capability to provide two types of images in addition to the high power level suitable for HIFU therapy. For more details, the authors refer the reader to [86, 87]. In addition, the setup of the experiment is shown in Fig. 4.2.

The DMUA used herein operates at a 3.5 MHz and has a central fenestration through

Table 4.1: DMUA specifications

Number of channels	32 x 2
Radius of curvature	40 mm
Elementary Pitch	1.5 mm
Inter-element spacing	0.2 mm
Height of the elements	30 mm with 16.5 mm centeral fenestration

which a diagnostic transducer is applied Fig. 4.1. Specifications of the used DMUA are summarized in table 4.1.

4.2.3 Simulated Treatments

We simulated two cases for targeting atherosclerotic plaques within the posterior wall of the femoral artery (FA) of FH swine. In each case, the treatment consisted of seven (7) HIFU shots with the foci spaced 1-mm spacing circumferentially at the periphery of the posterior wall. The intensity was approximately 5000 W/ cm2 with 2-sec exposure duration for each shot. The wait time between shots was approximately 1.5 seconds. Electronic steering was used to generate the shots without the need to move the transducer mechanically. Case #1 This case was sacrificed after 3 days and the HIFU beam passed through the skin, fat, muscles, and perivascular connective tissue before crossing the arterial lumen to reach the targeted plaque in the posterior wall of the FA as shown in Fig. 4.4. This case was an example of a successful treatment as evidenced by histological evaluation. Case #2 This case was sacrificed after a month and the saphenous artery (proximal branch of the FA) traversed in front of the FA to come within the path of the incident HIFU beam possibly causing scattering and distortion of the therapeutic HIFU beam as shown in Fig. 4.3. Histological evaluation in this case showed a prefocal lesion proximal to the saphenous artery and represents an example of collateral damage that could have been predicted by numerical modeling.

4.3 Numerical Model

A finite difference approximation of partial derivatives was used in the numerical solution of the partial differential equations (PDE). The FDTD method is a powerful tool for solving a broad range of PDEs [88]. The FDTD heterogeneous model for acoustic and thermal tissue response was used; the model is based on the wave equation and the transient bio heat transfer equation (BHTE). This was achieved after segmentation of the ultrasound image to yield accurate information about the regional anatomical details and by using the values of Table 4.2 [89, 90]. A level-set method described in [91] was used for segmentation of the different tissue regions. The simulation accounted for the thickness and nature of the skin, subcutaneous fat, muscles, perivascular connective tissue and the blood vessel within the path of the HIFU beam is illustrated in (Figure 4.4) which shows an ultrasound image of the target femoral artery (labeled A) with the labeling of the skin (S), fat (F), muscle (M), and connective tissue (CT). To maintain the stability of this model, the temporal step follows the Courant, Friedrichs and Lewy (CFL) condition [31, 88]. Electronic steering of the HIFU beam was also considered in this simulation, as described in [92].

4.3.1 Acoustic Model

The propagation of ultrasound field is governed by the wave equation. We used this equation to model the HIFU field from the DMUA. This model followed the following equation:

$$\boxed{\begin{aligned} \frac{\partial \mathbf{v}}{\partial t} &= \frac{-1}{\rho}\nabla \mathbf{p} \\ \frac{\partial \mathbf{p}}{\partial t} &= -\rho . c^2 \nabla . \mathbf{v} + \beta \mathbf{p} \end{aligned}}$$

where $\mathbf{v}, \mathbf{p}, c$ and β denote the particle velocity, pressure, speed of sound, attenuation respectively.

This acoustic numerical simulation with a perfect matched layer as a material absorbing boundary condition followed the acoustic model described in section 2.3.

4.3.2 Thermal Model

The transient bio-heat transfer equation (BHTE) is used to govern the thermal effects in tissue with a convective term, as described in [77]. The temperature model is described by the following equation:

$$\boxed{\rho C_t \frac{\partial \mathbf{T}}{\partial t} = k\nabla^2 T - W_b C_b (T - T_b) + (\rho C_p)_b \bar{v}.\nabla T + Q} \tag{4.1}$$

where T, C, ρ, K, w, v, Q are the temperature, specific heat, density, thermal conductivity, perfusion rate, blood flow velocity, and the external heating (HIFU) source, respectively. The term $\nabla.K\nabla T$ models the thermal diffusion, while $w_b C_b (T_a - T)$ models the effect of perfusion. The boundary condition of the tissue domain is conducted through body temperature (37 °C) at the domain borders. The temperature initial condition is assumed to be (37 °C). The simulation was conducted at a 3.5MHz central frequency with an approximately corresponding wavelength of 0.42 mm and the simulation grid was set to one tenth of a wavelength. A Forward-Time Central-Space (FTCS) has been used with applying upwind differencing (class of numerical discretization) for the convection component. A forward difference for the time derivative, a backward difference for the first spatial derivative and a centered difference for the second spatial derivative is as follows:

$$\boxed{\begin{array}{ccr} \rho C_t \dfrac{\mathbf{T}^{n+1}_{i,j,l} - \mathbf{T}^{n}_{i,j,l}}{\triangle t} & = & k \left[\begin{array}{cc} \frac{\mathbf{T}^n_{i+1,j,l} - 2\mathbf{T}^n_{i,j,l} + \mathbf{T}^n_{i-1,j,l}}{\triangle x} & + \\ \frac{\mathbf{T}^n_{i,j+1,l} - 2\mathbf{T}^n_{i,j,l} + \mathbf{T}^n_{i,j-1,l}}{\triangle y} & + \\ \frac{\mathbf{T}^n_{i,j,l+1} - 2\mathbf{T}^n_{i,j,l} + \mathbf{T}^n_{i,j,l-1}}{\triangle z}) & \end{array} \right] \\ & - & W_b C_b (\mathbf{T}_a - \mathbf{T}^n_{i,j,l}) \\ & + & \rho C_p \, \bar{v} \dfrac{\mathbf{T}^n_{i,j+1,l} - \mathbf{T}^n_{i,j-1,l}}{\triangle y} + Q \end{array}} \tag{4.2}$$

The numerical error is on the order of t and. In order to meet the stability criteria as indicated previously, the temporal step followed the (CFL) condition [31] to achieve the convergence of the difference approximation.

Table 4.2: Acoustic and Thermal values for the medium

Type	Density kg/m^3	Specific Heat $J./kg.\,^{\circ}\mathrm{C}$	Thermal Conductivity $W.m^{-1}/\,^{\circ}\mathrm{C}$	Speed of Sound m/s	Attenuation $dB/cm/MHz$
Skin	1109	3530	0.4	1400	1.15
Fat	960	2973	0.24	1476	0.36
Connective Tissue	1525	2372	0.39	1613	1
Muscle	1090	3600	0.42	1547	2
Blood	1050	3800	0.55	1627	0.1
Blood Vessel Wall	1102	3400	0.48	1550	1.15
Atherosclerotic plaque	1320	2900	0.49	1600	1.2

4.4 Thermal dose

Follow exactly section 2.5.

4.5 Simulation results

The acoustic field simulation accounted for the phased array concave geometry of 3.5-MHz 32x2 elements, described in [87], used to target the femoral artery of the adult swine through a water bolus. The simulation grid spacing was set to one tenth of the acoustic signal wavelength in water and the acoustic and thermal simulation parameters are shown in Table 2. The area of induced HIFU thermal damage was defined as the tissue area that reached a thermal dose equivalent to 43 °C for 240 minutes. As a guidance to detect the location of the arterial pulsation, we performed the two dimensional M-mode and strain imaging as shown in Fig. 4.15 and Fig. 4.16. Case #1: An ultrasound image of the target femoral artery was acquired and segmented using the level-set method as described in [26]. The segmentation contours and the different tissue types are shown in Fig. 4.5. The lesion formed at each shot is shown in Fig .4.6. Fig .4.5, the extension and configuration of the HIFU induced thermal damage, as predicted by the simulation, significantly matches the actual damage as detected by histology evaluation. Another important outcome predicted by the proposed model was that the temperature distribution over the intima was lower than at the focus, within the plaque itself. Therefore, the intima was kept intact without any significant damage. Also Fig .4.5 shows the intact intimal endothelial lining overlying the targeted plaque in histology. This was in keeping with the results predicted by the simulation model. The results of our simulation correlated well with the histology data of the targeted plaque which has revealed thermal injury within the plaque tissue consistent with the applied HIFU shots.

Case 2: In this case, the aim was to target an atherosclerotic plaque within the posterior wall of the external femoral artery partially obscured by another artery on the high intensity focused ultrasound (HIFU) path in large (100 140 Kg) swine. The simulation model showed evidence of prefocal damage in the vicinity of the saphenous artery, while the temperature rise within the targeted plaques was below the threshold for thermal damage. Histology analysis was again consistent with the simulation results. As shown in Fig. 4.14) histology analyses showed evidence of fibrosis (scarring) in the connective tissue adjacent to the saphenous artery, while there was no unequivocal HIFU induced thermal damage in the targeted plaque. Fig. 4.7 to Fig. 4.13 show the step by step creation, in each shot, of the lesion in addition to the increased temperature . The fact that no unequivocal HIFU lesions were detected within the targeted atherosclerotic plaques can be explained by the orientation of the saphenous artery in relation to the femoral artery during treatment. Fig. 4.4 shows that the saphenous artery, together with its perivascular connective tissue, is directly superficial and in front of the FA within the path of the HIFU beam. It also shows the arterial pulsation detected from the two dimensional M-mode and strain imaging techniques. Orientation was attributed to slight tilting of the transducer during treatment. With this orientation, the saphenous artery became aligned with the FA as compared to its position in the pre-procedural ultrasound scanning, as shown in Fig. 4.4. Thus, the saphenous artery may have masked significant HIFU energy from reaching its original target within the plaque in the femoral artery. The simulation program showed that HIFU induced damage in the prefocal region instead of the target area. As in both cases, the formed HIFU lesions, as predicted by our simulation, is consistent with the actual damage detected in histology.

4.6 Discussion

We have previously demonstrated that HIFU can be delivered, safely and with sufficient energy, to induce thermal damage within atherosclerotic plaques in-vivo [86].

However, for the proposed approach to gain more acceptance, we needed to explore the behavior of the HIFU lesions within the targeted plaques. Simulation programs, like the one we propose here, should help to predict the extent and pattern of thermal damage induced within the targeted plaques. Our experience so far shows that, even for the same exposure parameters, the size and extension of the HIFU lesions within the plaque are not consistent. This may be attributed to differences in plaque composition, blood flow parameters or other anatomical constraints in the path of the HIFU beam. The proposed simulation model considered the effect of wall thickness of large arteries and the heat sink effect of flowing blood. Furthermore, we integrated the anatomical details obtained from an ultrasound scan of the region of interest within our simulation program. Thus, we took into consideration the attenuation of the HIFU beam caused by different anatomical regions. We consider histological analysis of the targeted plaques as the gold standard for evaluation of HIFU induced damage. We had a unique opportunity to validate the results of our simulation program against those of histology. For case #1, the extension and configuration of thermal damage predicted by the simulation program correlated well with the actual HIFU induced thermal damage detected within the targeted plaque on histology. Of note, running the simulation program clearly showed the pattern by which the discrete thermal lesions overlapped to create such a confluent zone of damage. This pattern can be explained by the thermal conduction within the fat rich plaque that caused the adjacent discrete HIFU lesion to overlap. The fact that the intimal endothelial lining was kept intact can be explained by the heat sink effect of the flowing blood in the targeted vessel that appears to protect the intima. An intact overlying endothelium is an important safety determinant of this procedure because any intimal damage, if accidentally induced, can carry the risk of inducing localized thrombosis or even serious distal embolism. For case #2, the saphenous artery with the surrounding connective tissue passing in front of the femoral artery increased the pre-focal attenuation of the HIFU beam, preventing the delivery of enough HIFU power to the inside of the targeted plaque. This resulted in unintended prefocal damage, with apparent failure to induce significant damage within the targeted plaque. This case clearly demonstrates the importance of analysis of the treatment region before treatment. In our experience, the pre-procedural diagnostic ultrasound scanning provided essential sufficient data about the treatment region. This information can help in treatment planning in view of the anatomical constraints within the path of the HIFU beam. Both safety and efficient control are essential requirements for any proposed application to be implemented clinically in the future. Real time feedback mechanisms need to be developed to provide instantaneous information regarding the ongoing treatment. However, we also believe that simulation models, like the one we are proposing herein, are essential to predict the outcome of the treatment in advance. This kind of prediction can give the treating physicians higher degree of confidence in predicting how the treatment process will proceed. Furthermore, if the feedback data can be implemented in such simulation programs in real time settings, this can provide physicians with enhanced visual perception and immediate evaluation of the ongoing treatment process.

4.7 Conclusion

The results provide an early validation for the feasibility of using image-based modeling of the acoustic and thermal field in heterogeneous tissues. Image-based modeling could play a critical role in treatment planning when HIFU is used in noninvasive precision lesion formation. In the first case, the simulation model correctly predicted the protection of the intima by the heat sink effect due to blood flow in the targeted vessel. This could be significant when noninvasive HIFU is used in the treatment of vulnerable plaques. In the second case, the model shows the formation of a lesion in the prefocal plan instead of the target area. In this case, the retrospective analysis benefited from real-time image data to help explain the collateral damage and the apparent failure to form a lesion at the target. The retrospective analysis can provide added value to the quality of treatment follow up based on risk analysis of collateral damage and confidence level of therapeutic outcome at the target.

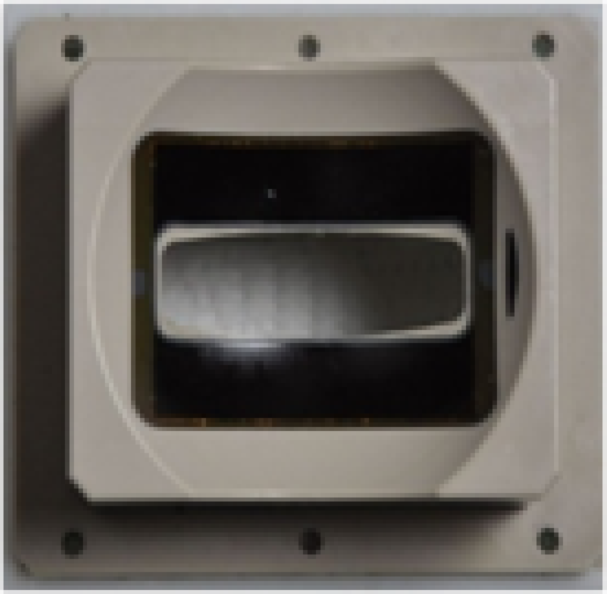

Figure 4.1: 3.5 MHz DMUA showing a central fenestration for integration of a diagnostic ultrasound transducer.

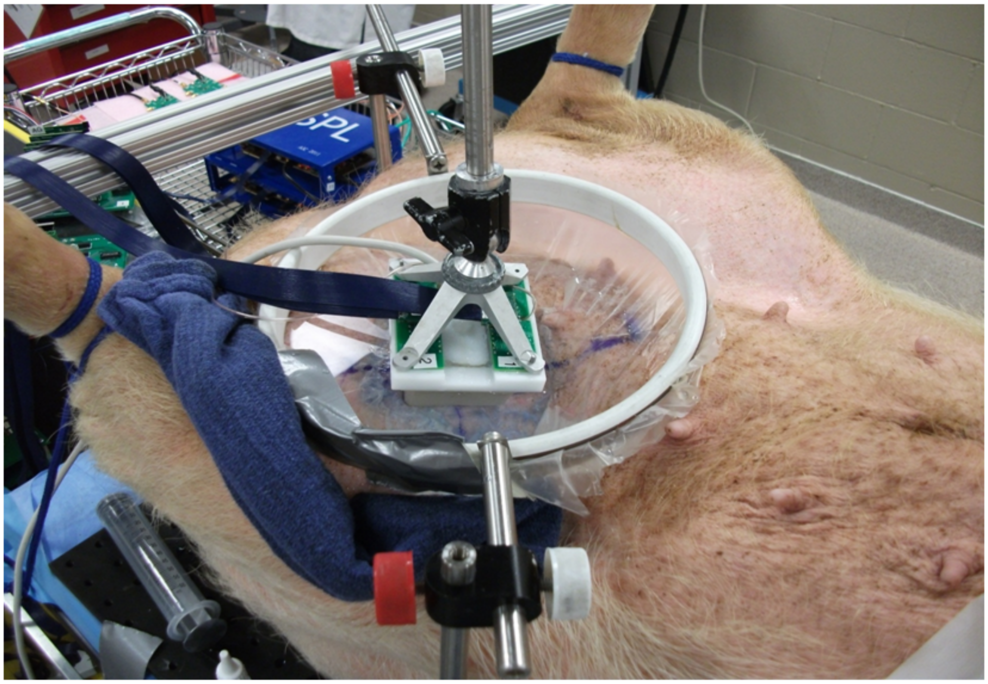

Figure 4.2: Setup of the experiment, The integration of both the diagnostic imaging transducer and the concave transducer merged in the water bolus.

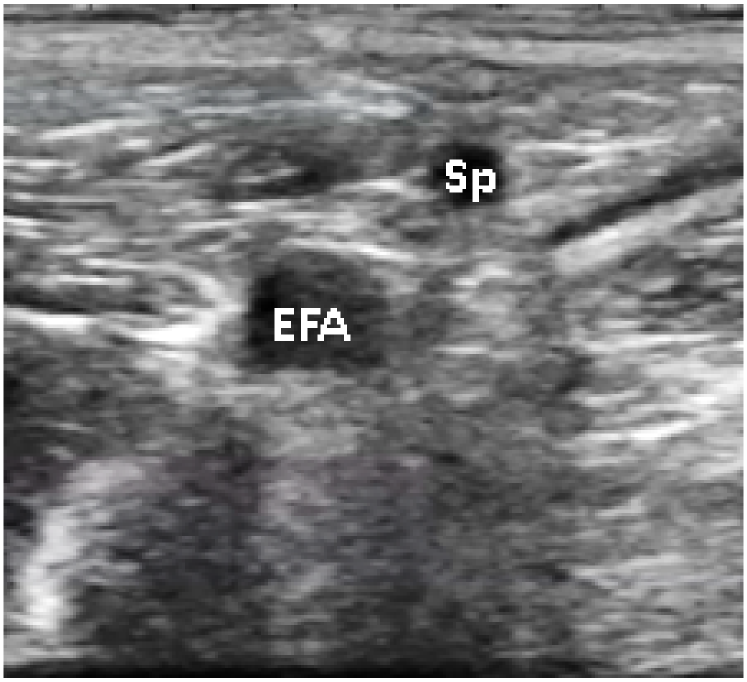

Figure 4.3: Second case, the saphenous artery (arrow) traversed in superficial to the EFA to come within the path of the incident HIFU beam. EFA: external femoral artery, Sp: saphenous artery.

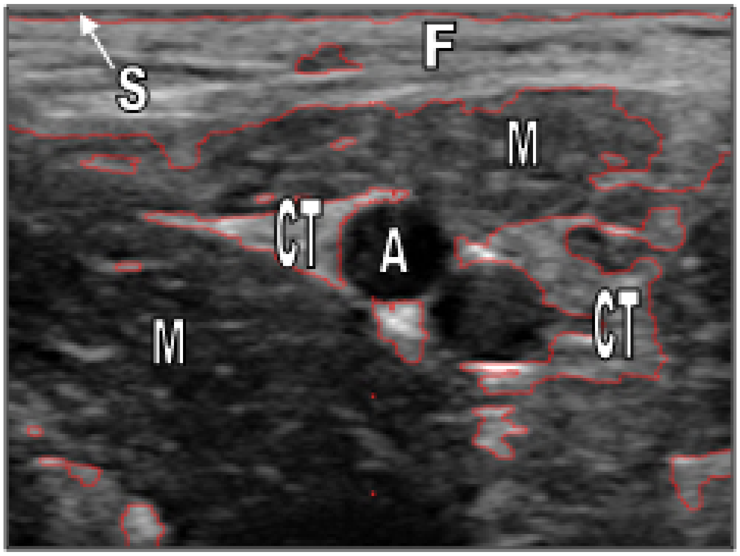

Figure 4.4: Segmentation of the ultrasound image from the treatment region. Segmentation lines outline the main anatomical structures. S: Skin, F: fat, M: muscles, A: artery, CT: connective tissue.

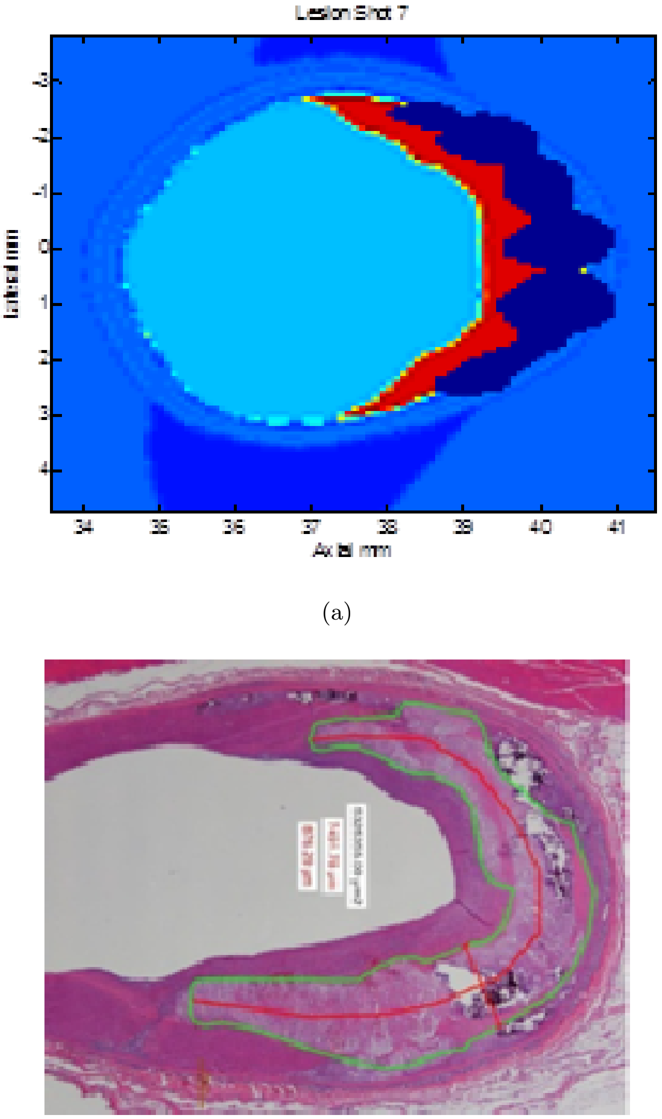

(a)

(b)

Figure 4.5: Correlation between the simulation results and histology. (a) Simulation result of the thermal dose within the targeted atheromatous plaque. (b) Thermal damage within the targeted plaques as shown from histology (H and E stain). Note the intact intima (black arrows) overlying the targeted plaque.

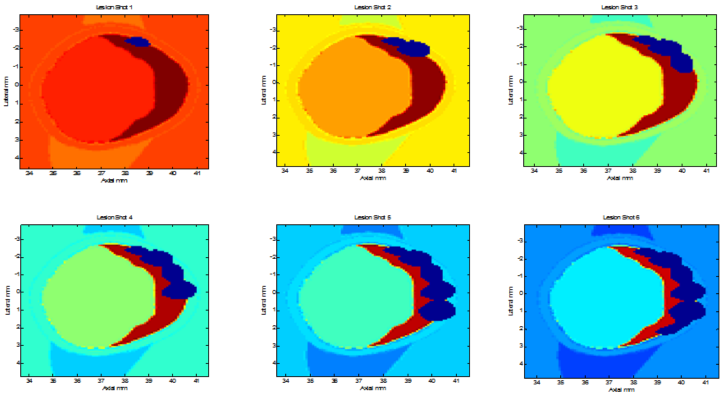

Figure 4.6: Simulation result of the lesion creation on each shot within the targeted atheromatous plaque..

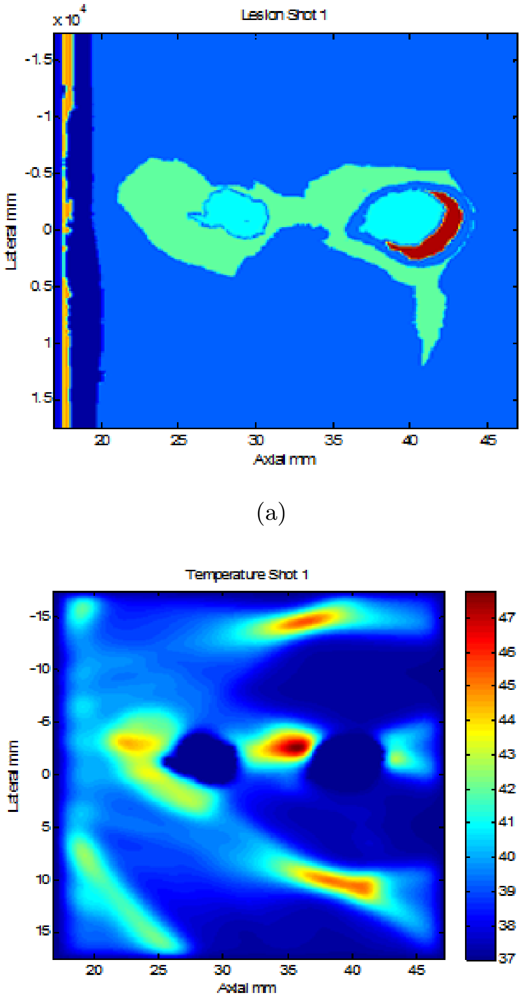

(a)

(b)

Figure 4.7: Simulation results of the first shot. (a) Simulation result of the thermal dose within the prefocal region. (b) Simulation result of the increased temperature in the domain.

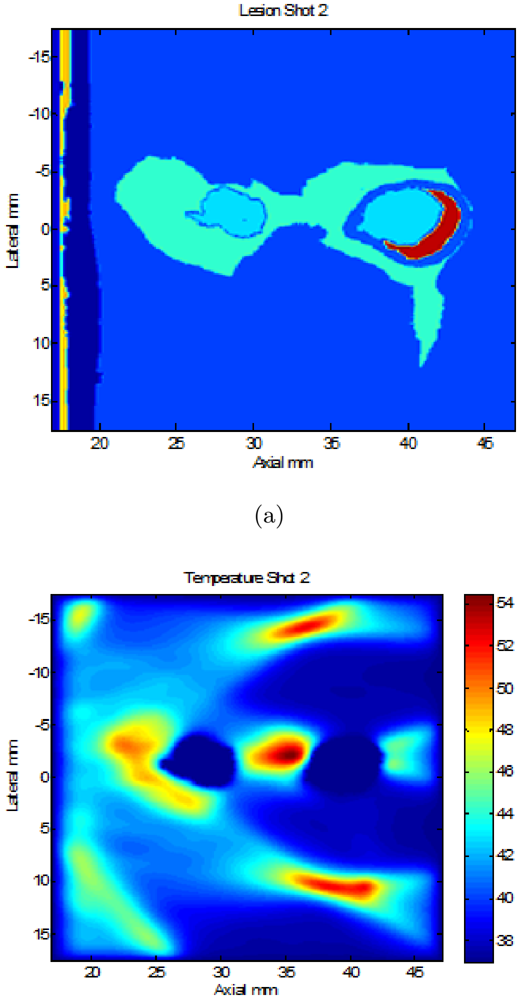

(a)

(b)

Figure 4.8: Simulation results of the second shot. (a) Simulation result of the thermal dose within the prefocal region. (b) Simulation result of the increased temperature in the domain.

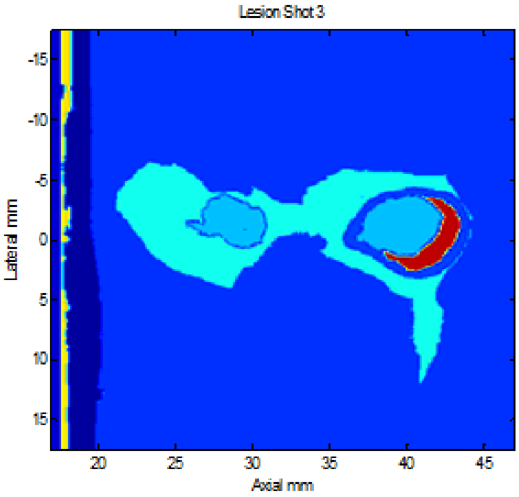

(a)

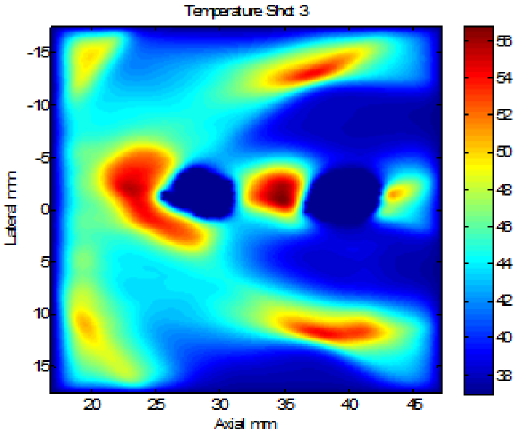

(b)

Figure 4.9: Simulation results of the third shot. (a) Simulation result of the thermal dose within the prefocal region. (b) Simulation result of the increased temperature in the domain.

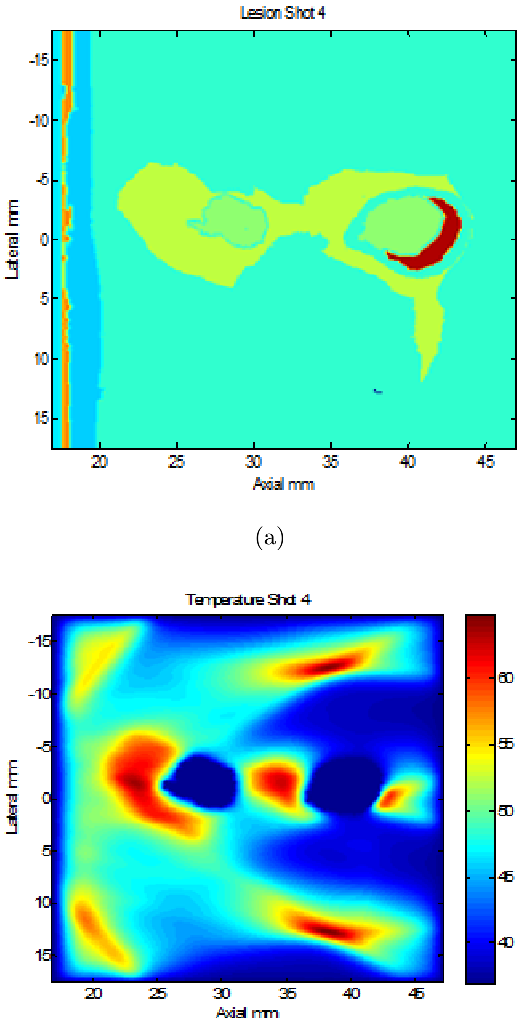

(a)

(b)

Figure 4.10: Simulation results of the fourth shot. (a) Simulation result of the thermal dose within the prefocal region. (b) Simulation result of the increased temperature in the domain.

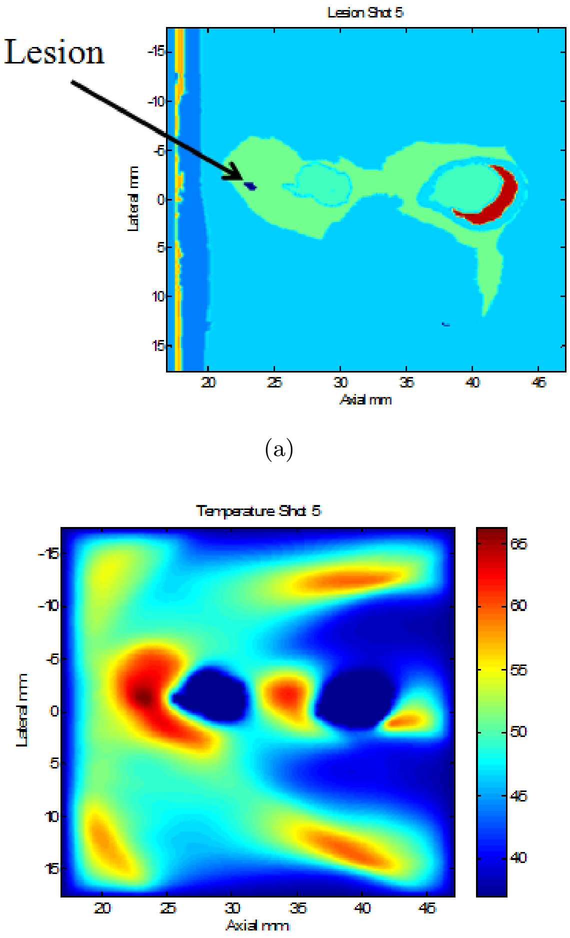

(a)

(b)

Figure 4.11: Simulation results of the fifth shot. (a) Simulation result of the thermal dose within the prefocal region. (b) Simulation result of the increased temperature in the domain.

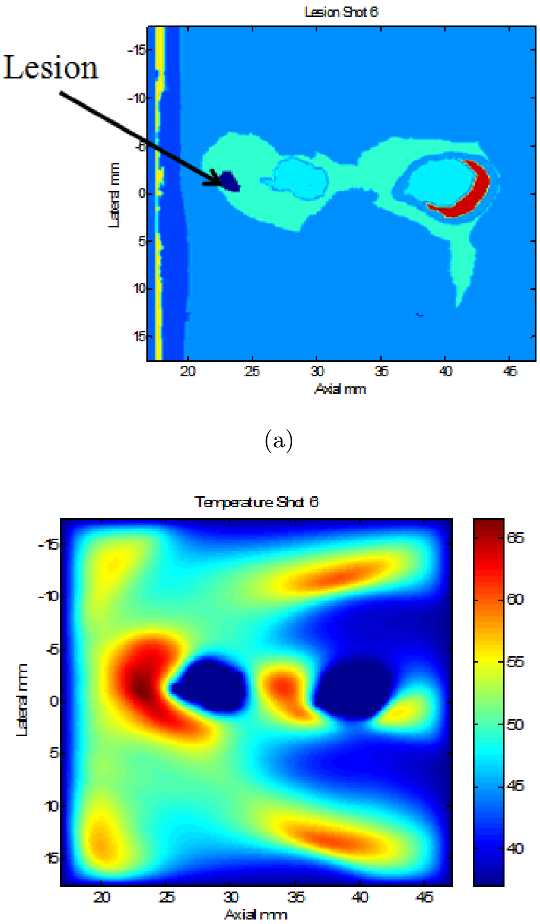

(a)

(b)

Figure 4.12: Simulation results of the sixth shot. (a) Simulation result of the thermal dose within the prefocal region. (b) Simulation result of the increased temperature in the domain.

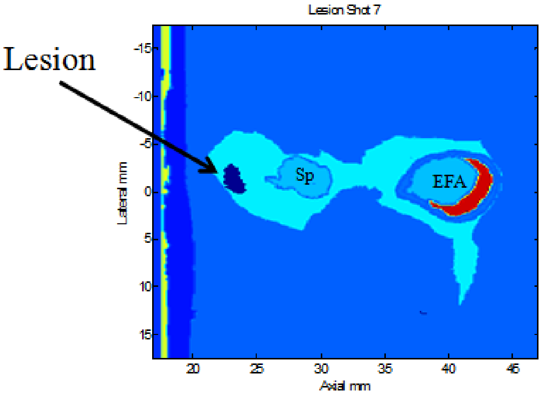

(a)

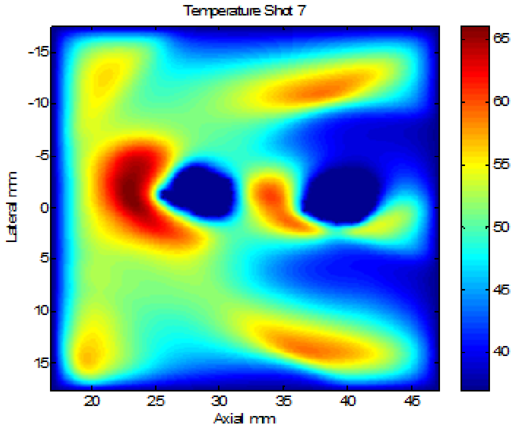

(b)

Figure 4.13: Simulation results of the seventh shot. (a) Simulation result of the thermal dose within the prefocal region. (b) Simulation result of the increased temperature in the domain.

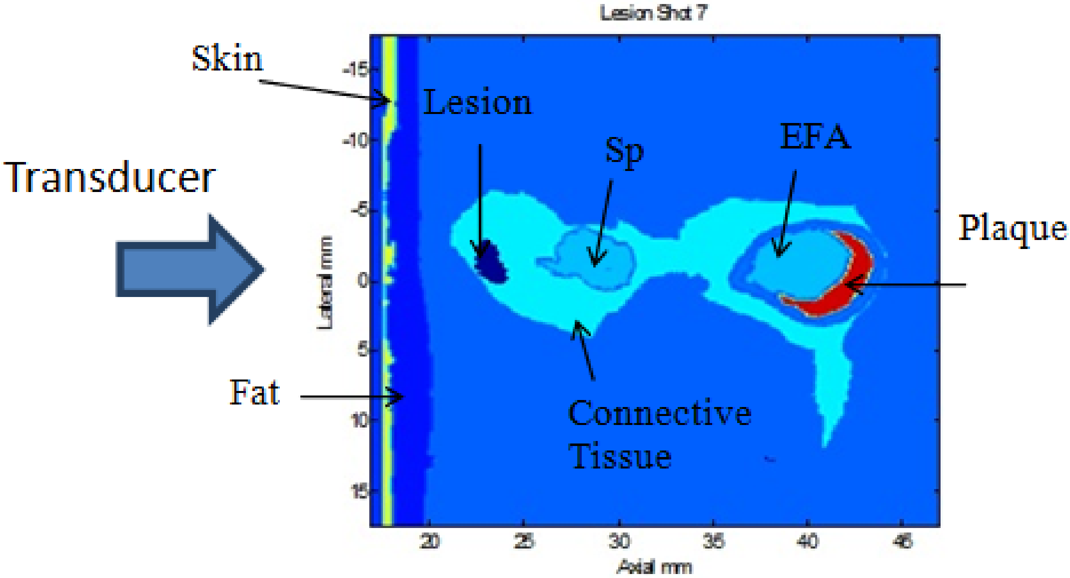

(a)

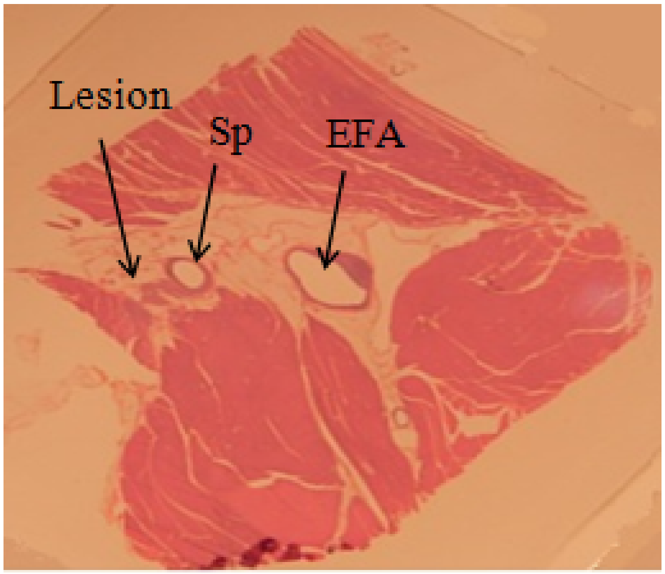

(b)

Figure 4.14: Correlation between the simulation results and gross histology slide. (a) Simulation result of the thermal dose within the prefocal region, the arrow points to the damage induced at the prefocal. (b) Thermal damage within the same region as shown from gross histology. EFA: external femoral artery, Sp: saphenous artery.

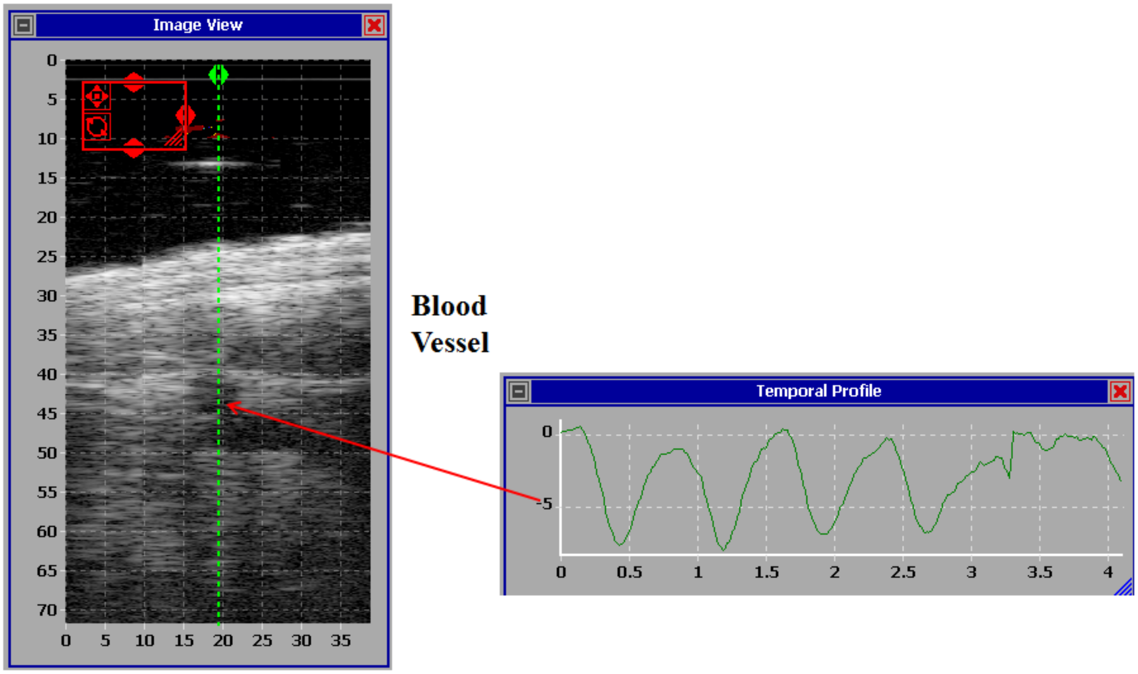

Figure 4.15: B-mode image of the treated region while targeting the blood vessel. The strain imaging on the right hand side shows a pulsation indicated the existing of blood vessels in the shown regions. EFA: external femoral artery, Sp: saphenous artery.

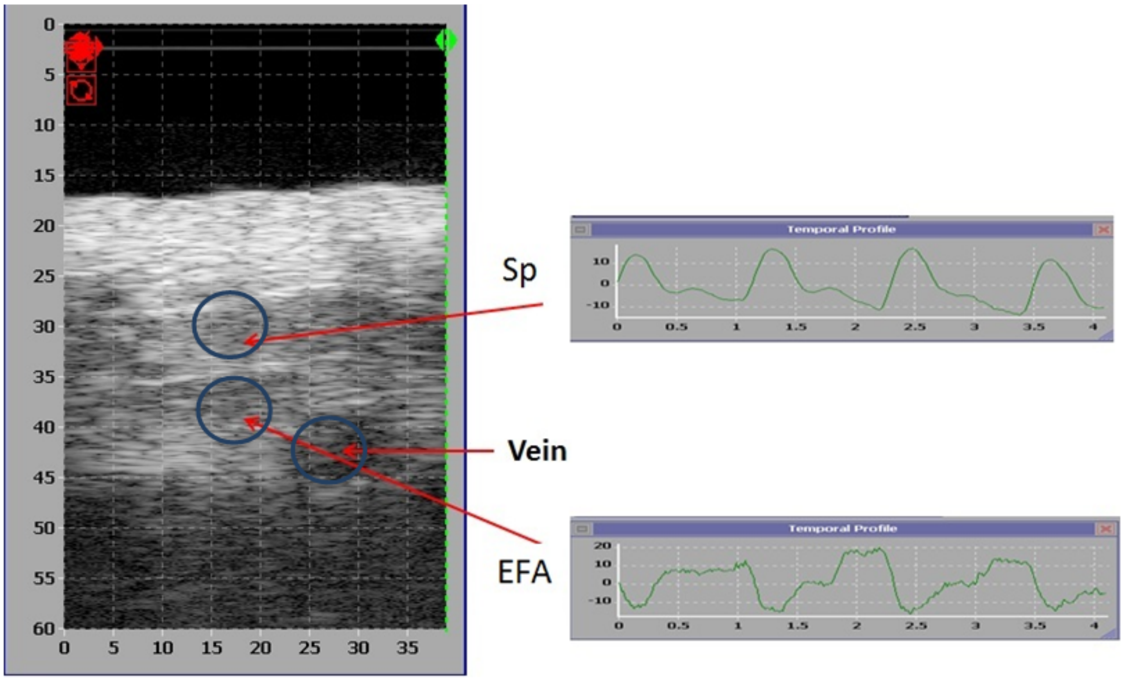

Figure 4.16: B-mode image of the treated region while targeting the blood vessel. The strain imaging on the right hand side shows a pulsation indicated the existing of blood vessels in the shown regions. EFA: external femoral artery, Sp: saphenous artery.

Chapter 5

Phase Coupled 2D Speckle Tracking using Riesz Transform

5.1 Introduction

Ultrasound speckle tracking is the task of detecting moving structures on the ultrasound image time sequence. It provides robust estimates of fine tissue displacements along the beam direction due to the analytic nature of echo data. To accomplish this, a sequence of 2D spatial correspondence based on radio frequency (RF) has to be continuously acquired at the same spatial location. The movement of a structure can be achieved by concatenating the spatial correspondence of the structure in consecutive frames and can be described by motion vectors. This is one of the most critical subjects in detecting ultrasound strain imaging. Many different approaches have been proposed to solve this problem. The correlation techniques have been widely used, e.g. cross correlation, and normalized cross correlation, which is assumed to be a robust technique for the estimation of displacement. These methods assume the linearity among the intensity distributions. Initial research in speckle tracking was conducted in 2D ultrasound sequences [93], [94]

Several approaches have been proposed for tracking ultrasound image sequences. One approach for estimating tissue motion in ultrasound images is called optical flow, which the displacement is estimated under the assumption of constant image intensities over time and classified as differential [95], phase-based [96], and block-matching

[97], [98] techniques. The problem with differential methods is that it generates inaccurate results as the ultrasound images are unlikely to keep the constancy of intensities. The optimality of filter design and its responses is the bottle neck of the phased-based techniques, while the block-matching (correlation based) techniques are less sensitive to noise and fast motion. The other approach is called speckle tracking, which has applications in estimating blood flow and elastography. The displacement is estimated under the assumption that the tissue region has the same unique speckle pattern, and is detected by locating the same speckle pattern in the consecutive frames using the block-matching method. The matching of the image similarity is performed by either using the sum of squared [99], absolute [100] difference or normalized cross correlation using 1D RF signals [101]-[102] , 2D based algorithms [103]-[104] or the extended 3D calculations [105]- [106].

The speckles limit the image quality; however, they have a direct impact in tissue motion detection. They are a result of the constructive and destructive interference generated by the reflection of tiny scatters [107] from the echo signals; the patterns of the speckles have been observed from the RF ultrasound data [93], [101] . Other approaches have quantified the similarity between the two images based on a maximum likelihood concept [108]. This concept assumes that the noise in both images follows the Rayleigh multiplicative distribution. The main limitations of the accuracy of all algorithms are the artifact, ambiguity of motion in weak acoustic scatters regions, and reverberation. In addition, tissues undergo rotation, shearing, stretching and translational motions. A number of groups have quantified the heart motion from two dimensional echocardiograms by locally analyzing the images using a local-affine model that allows the description of typical heart motions [109], [110]. All the previous approaches have generated the analytical signal by calculating the Hilbert transform with respect to one of the image coordinate axes; this method suffers from the absence of an isotropic extension of the analytic signal in the two dimensional case. In this chapter we present an assessment method for the strain and shear strain estimation of the blood flow field and the wall/tissue motion which is indeed essential in clinical practice. This method is based on an earlier described polynomial fit method and the phase coupled 2-D speckle tracking algorithm [111] using a generalization method of the analytic signal. The algorithm uses the cross-correlation function between two images and the zero crossing of the cross-correlation phase to estimate the displacement. The generalization method extends the analytic signal concept to multiple dimensions and is built from the Riesz transform which is the vector extension of the Hilbert transform [112]. Refer to [113] and references therein for more details. Robustness of the tracking algorithm is investigated using a realistic synthetic data sequences created with (Field II) for which the bench mark displacement was known. In addition, the new multi dimension speckle tracking (MDST) method is used in the estimation of the flow and surrounding tissue motion on controlled tissue-mimicking flow phantom (ATS Model 524) and human carotid artery *in- vivo*. We have also studied the problem of finding the peak by getting the coefficients of a second order polynomial that fits the 2-D cross correlation matrix. To focus on the relevant regions of interest, the motion is color coded and superimposed on the original image in a way similar to tissue Doppler imaging. The results obtained show that using Riesz transform produces more robust estimation of the true displacement of the simulated model compared to previously published results.

5.2 Material and Methods

5.2.1 Hilbert Transform

The desire to construct the Hilbert transform is to find a companion function $g(x)$ for a real-valued function $f(x) : \Re \rightarrow \Re$ so that the addition of both $a(x) = f(x) + ig(x)$ can be analytically extended from the real line $t \epsilon \Re$ to the upper half of the complex plane. The companion function $g(x)$ is called the Hilbert transform of $f(x)$ and the real part of the analytic function is equal to the original given function $f(x)$. The Hilbert transform can be computed by first calculating the Fourier transform of the signal, then rejecting the negative frequencies. To get the complex-valued signal we then have to calculate the inverse Fourier transform to get the the real and the imaginary parts that form a Hilbert-transform pair. This can be done in *Matlab* by using *hilbert* function that computes the discrete-time analytic signal $a(x)$ such that $g(x)$ is the Hilbert transform of $f(x)$. It is done by getting $F(u)$ which is the FFT of $f(x)$ and only taking the elements that correspond to frequencies in $-\pi < \omega < 0$ and finally getting the inverse FFT. In order to get a 2-D generalization of the Hilbert transform, we have to preserve the anti symmetric property $H(-x) = -H(x)$, the property of the suppression of the

DC component $H(0) = 0$ and the property that the energy is equal to one for all nonzero frequencies $H(x) = 1 \quad \forall x < 0$. Other properties are discussed in [114]. The 2-D Hilbert transform is a key to getting a 2-D analytic signal. Consequently, the analytic signal has the following properties:

- The total energy is twice the energy of the original signal if we neglect the DC component.
- Has a one sided spectrum $[H(x) = 0 \quad \forall x < 0]$.
- Performs a split of identity.

Split of identity means that the modulus of the analytic signal can be identified as a local amplitude and a local phase which fulfills the properties of invariance and equivariance [115]. The local amplitude represents the quantitative measure, while the local phase represents the qualitative information. This means that the local phase varies with local structure changes and that the local amplitude represents the local energy. The signal is a combination of two independent information known as the structure and the energy. This is not the case if the combination is formed of partial signals with different local phases on different scales. In this case, the signal has to be bandpass filtered to maintain the invariance-equivariance property and remove the other partial signals. The analytic signal in the case of 1-D Hilbert transform will be:

$$\boxed{\begin{aligned} a(x) = &\quad f(x) \quad + \quad ig(x) \\ = &\quad f(x)(\delta(x) + \frac{i}{\pi x}). \end{aligned}} \tag{5.1}$$

where $g(x)$ is the Hilbert transform of $f(x)$. This can be represented in the Fourier domain as follows:

$$\boxed{\begin{aligned} A(u) = &\quad F(u) \quad + \quad iG(u) \\ = &\quad F(u)(1 + sign(u)). \end{aligned}} \tag{5.2}$$

Using these concepts, a 2-D generalization of the Hilbert transform has to be defined. The following approach discusses the generalization of Hilbert transform to higher dimensions. (more extensive discussion is presented in the literature [114], [113]).

- *Partial Hilbert transform*: The Hilbert transform is performed with respect to one of the coordinate (axis) directions (n):

  $$\boxed{H_p(u) = i\; sign(< u,\, n >).} \tag{5.3}$$

  as $< u,\, n >= u^T \,.\, n$ where T refers for the transpose.

- *Total Hilbert transform*: The Hilbert transform is performed with respect to both axes:

  $$\boxed{H_T(u) = -sign(u_1)\; sign(u_2).} \tag{5.4}$$

  which can be represented more generally for (n) directions:

  $$\boxed{H_T(u) = (-i)^n \prod_{j=1}^{n} sign(u_j).} \tag{5.5}$$

  This can not be a valid approach for the generalization since it is missing the phase shift of $\pi/2$.

  A successive application of partial Hilbert transform with respect to all (n) axis directions can be considered as a way to calculate the total n-D Hilbert transform.

- We can combine the previous two concepts in the complex Fourier domain to achieve a one quadrant analytic signal [116, 117]:

  $$\boxed{H_Q(u) = i(sign(u_1) + sign(u_2) + sign(u_1)\; sign(u_2)).} \tag{5.6}$$

The common problem of all the previous approaches for calculating the Hilbert transform for more than 1-D is the missing isotropy (dependence on the orientation of a signal) of the transform, which is a key to maintaining the invariance equivariance property.

5.2.2 Riesz Transform

Riesz transform is a vector extension of the Hilbert transform in the n-D Euclidean space. In our case we will stick with the 2-D space, and the spatial representation of the Riesz transform is:

$$\boxed{(R_x(x,y), R_y(x,y)) = (\frac{x}{2\pi|(x,y)|^3}, \frac{y}{2\pi|(x,y)|^3}),\ (x,y)\epsilon\mathbb{R}^2} \tag{5.7}$$

The expression of the Riesz transformed as a function in the Fourier domain is:

$$\boxed{R_u(u,w), R_w(u,w) = (\frac{-iu}{2\pi|(u,w)|}, \frac{-iw}{2\pi|(u,w)|}),\ (u,w)\epsilon\mathbb{R}^2} \tag{5.8}$$

and

$$\boxed{H_R(u,w) = (\frac{-iu}{2\pi|(u,w)|}, \frac{-iw}{2\pi|(u,w)|})} \tag{5.9}$$

The relation to the Fourier domain is obtained from the theorem of the derivative in the Fourier domain $F(|x|^{-1}) = |u|^{-1}$ [112], [118]. The Riesz transform is a 2-D vector generalization of the Hilbert transform.

5.2.3 2D Analytic Signal

The generalization of the 1-D analytic signal to the 2-D Euclidean space will no longer be based on the Hilbert transform; instead it will be based on the Riesz transform [112]. The combination of the signal f and its Riesz transform forms the 2-D analytic signal.

$$A_{2D} = (f,\ R_x * f,\ R_y * f) \tag{5.10}$$

as $*$ stands for convolution. Having defined the 2-D generalization of the analytic signal, we can check properties of the Riesz transform.

- It is antisymmetric as $H_R(-(u,w)) = -H_R(u,w)$.
- It suppresses the DC component as $H_R(0,0) = 0$.

- $|H_R(u,w)| = 1 \forall\ (u,w) \neq 0$.

According to the properties of the Riesz transform, the new 2-D analytic signal has the following properties.

- The energy of the new 2-D analytic signal is double the original signal in case we neglect the DC component.
- The new 2-D analytic signal fulfills the split of identity [117]. The amplitude of the signal is only modified by a constant real factor, which means it satisfy the isotropy property.

5.3 Phase Coupled 2D Speckle Tracking Algorithm

The phase-coupled 2D speckle tracking method has been introduced in [111]. Let the analytic ultrasonic signal received from a 2-D region at time t_o be $a(x, y, t_o)$. The signal after time t_1 with a displacement $d_x\hat{x}+d_y\hat{y}$ can be described as $a_{new} = a(x-d_x, y-d_y, t_o)$. In the Fourier domain the equation will be:

$$\boxed{A_{new} = A(k_x, k_y, t_o)e^{-j(k_x d_x + k_y d_y)}} \tag{5.11}$$

where k_x and k_y are spatial frequency variables in the x and y directions, respectively. The correlation in the Fourier domain is written as:

$$\boxed{G_{12}(k_x, k_y) = |A(k_x, k_y, t_o)|^2 e^{-j(k_x d_x + k_y d_y)}} \tag{5.12}$$

The 2D cross correlation function can be represented as:

$$\begin{aligned} g_{12}(l_x, l_y) &= (a_{new} * a)(l_x, l_y) && (5.13) \\ &= g_{11}(l_x - d_x, l_y - d_y) && (5.14) \end{aligned}$$

where $*$ is a convolution operator and l_x and l_y are the lags in the x and y directions, respectively. The function peak in both the axial and lateral directions is located at lag values equal to the shift values, and the integer position of the region is estimated by finding the position of maximal correlation. To get a sub-pixel resolution, a method for a search algorithm in a $3x3$ region around the integer position with maximal correlation is introduced in [111]. This is achieved with a minimum level of lateral interpolation. The novelty of this approach is that it acquires the subsample accuracy by utilizing, near the correlation peak, the phase and the magnitude gradients in both axial and lateral directions. The zero phase contour is orthogonal to the magnitude gradient of the true peak. The 2D phase-coupled algorithm achieves smooth lateral displacement estimates highly free of quantization effects due to interpolation. In addition, the adaptive localized determination of the interpolation factor used leads to an estimate that is robust and computationally efficient. Refer to [111] for a full description of the 2D phase-coupled approach.

5.4 Polynomial Fit

The basic idea of polynomial fit is to approximate a neighborhood of each pixel with a polynomial; it is assumed that we can capture sufficient information about the signal through the coefficients of the polynomial. We can use polynomials of any degree, but our primary and exclusive interest is on quadratic polynomials. This is primarily because the surface near the true correlation peak is close to quadratic function in the l_x, l_y space.

The local signal model is expressed as:

$$\begin{aligned} f(L) &\simeq L^T \mathbf{Q}\, L + d^T L + c \qquad (5.15) \\ &= (l_x\ l_y)\mathbf{Q} \begin{pmatrix} l_x \\ l_y \end{pmatrix} + d^T \begin{pmatrix} l_x \\ l_y \end{pmatrix} + c \end{aligned}$$

where f is the magnitude of the 2D complex cross correlation in the vicinity of the true peak, $\mathbf{Q}$ is a symmetric matrix, d a vector, c a scalar and $L^T = (l_x\ l_y)$.

We can write the complex correlation function model in the form:

$$f(L) = a_1 + a_2 l_x + a_3 l_y + a_4 l_x^2 + a_5 l_y^2 + a_6 l_x l_y \qquad (5.16)$$

where

$$\mathbf{Q} = \begin{pmatrix} a_4 & \frac{a_6}{2} \\ \frac{a_6}{2} & r_5 \end{pmatrix} \tag{5.17}$$

$$d = \begin{pmatrix} a_2 \\ a_3 \end{pmatrix}$$

$$c = a_1$$

We can conclude that the quadratic term $\mathbf{Q}$ captures the even part information of the signal (excluding DC), the linear term d captures the odd part information, and the local DC level is captured by the constant term c.

The coefficients of the model can be estimated with the basis functions:

$$[1, l_x, l_y, l_x^2, l_y^2, l_x l_y] \tag{5.18}$$

The equation $\mathbf{A}\mathbf{x} - \hat{f}$ is not guaranteed to have a solution, where $\mathbf{x} = [a_1\ a_2\ a_3\ a_4\ a_5\ a_6]^t$ and

$$\mathbf{A} = \begin{bmatrix} l_{x1}^2 & l_{y1}^2 & l_{x1}l_{y1} & l_{x1} & l_{y1} & 1 \\ l_{x2}^2 & l_{y2}^2 & l_{x2}l_{y2} & l_{x2} & l_{y2} & 1 \\ \vdots & \vdots & \vdots & \vdots & \vdots & \vdots \\ l_{xN}^2 & l_{yN}^2 & l_{xN}l_{yN} & l_{xN} & l_{yN} & 1 \end{bmatrix} \tag{5.19}$$

where $N = 9$ is the number of points on the grid. It is possible to get polynomial coefficients by minimizing the residual square error. The linear least square problem is:

$$\boxed{arg \min_{\mathbf{x}\in\mathbb{R}^N} \qquad ||\mathbf{A}\mathbf{x} - \hat{f}||^2} \tag{5.20}$$

If we assume that $\mathbf{A}$ is an n x m matrix, which, in our case $n > m$, and of rank m the solution for eq. 5.20 is:

$$\mathbf{x} = (\mathbf{A}^T\mathbf{A})^{-1}\mathbf{A}^T\hat{f} \tag{5.21}$$

where T refers to the transpose of a matrix. By evaluating the gradients of eq. 5.16, we can calculate $l_{x_{max}}$ and $l_{y_{max}}$

$$\frac{\partial f}{\partial l_x} = 2a_1 l_x + a_3 l_y + a_4 \tag{5.22}$$

$$\frac{\partial f}{\partial l_y} = a_3 l_x + 2a_2 l_y + a_5 \tag{5.23}$$

The matrix equation can be solved to get:

$$\begin{bmatrix} l_{x_{max}} \\ l_{y_{max}} \end{bmatrix} = \begin{bmatrix} 2a_1 & a_3 \\ a_3 & 2a_2 \end{bmatrix}^{-1} \begin{bmatrix} -a_4 \\ a_5 \end{bmatrix} \tag{5.24}$$

The solution is based only on the magnitude, which can result in an error in the estimate of the true correlation peak, especially in the axial direction. The reason behind that is the extent in axial direction is only 1 lag sample. This is not the case in the interpolated lateral direction which results in a smooth quadratic polynomial expansion. Consequently, the derivative will yield a reliable estimate of the peak. The estimate of the shift in the axial direction can be achieved with high subsample accuracy using complex cross correlation without interpolation [119], [120], [121].

5.5 Strain Calculations

We use the MATLABs gradient command, using the 2D speckle tracking method of the axial and lateral displacement fields, to calculate the strain and shear strain. A simple Gaussian lowpass filter with a size of 3 x 3 and standard deviation of 1 follows the strain and shear strain calculations.

5.6 Results

5.6.1 Data Acquisition

A diagnostic ultrasound scanning (Sonix RP; Ultrasonix, Richmond, British Columbia, Canada) was performed by using a 7.2-MHz center frequency of the transmit pulse. The linear array transducer (L14-5/38; Ultrasonix) was used to acquire the M2D pulse echo data through a custom designed program. A Cole Parmer Master Flex pump was used with the ATS Model 524 flow phantom to emulate the flow in a blood vessel. This can illustrate the displacement in both directions (axial and lateral). The controlled fluid flow channel in the ATS model has a 4-mm diameter; the pump is used to mimic the blood flow rates in a carotid artery (e.g. 336 ml/min). In order to produce a flow channel with linear scattering during the collection of data, a cellulose micro-spheres were diluted in water. As a ground truth validation, we have imaged pure water as a control to determine the channel boundaries. The M2D data was collected at a frame rate of approximately 325 frames per second. This was typical of the setup described in [122].

5.6.2 Field II simulation

An ultrasound simulation program (Field II) is used to generate data for the flow in a blood vessels similar to a carotid artery. A parabolic velocity profile is used as a fair approximation for most of the cardiac cycle [123] of the type of artery used in this simulation. We limit the simulated phantom to generate 2 files of the scatterers positions at the corresponding time step. According to the velocity function and the time between pulses, the scatterers propagate to a new position in the next generated file. Consequently the RF lines are generated for different imaging directions at different times according to the number of files generated (2 in our case). A 64 active element of linear array scanner was used with a Hanning window as an apodization function during transmission and receiving. The elements have a Kerf of 0.05 mm, a height of 5 mm and a width of a wavelength ($\lambda = \frac{c}{f_o}$) as $c = 1540m/s$ represents the speed of sound and $f_o = 5MHz$ is the transducer center frequency. We used a fixed transmit focus placed at 70 mm while the receiver focus was accomplished at 30 mm from the surface of the transducer in 20 mm intervals.

5.6.3 Simulated Phantom Results

Robustness of the tracking algorithm is investigated using a realistic synthetic data sequences created with (Field II) for which the bench mark displacement was known. The displacement is estimated from acquired successive radio-frequency (RF) data frames of the region of interest.

The graphics below highlights the result obtained from a simulated model for an interpolation-based phase coupled and the new method (MDST). Fig. 5.1 shows the displacement estimation of the simulated model in the lateral direction, while Fig. 5.1 shows the displacement estimation of the simulated model in the axial direction.

We also applied the same concept of generalization of the analytic signal to the polynomial expansion method described earlier. Fig. 5.3 shows the displacement estimation comparison of the simulated model in the lateral direction using the parabolic polynomial expansion technique with Hilbert and Riesz transform, and Fig. 5.4 shows the displacement estimation of the simulated model in the axial direction.

5.6.4 Flow Phantom Results

The image data of a 4-mm flow channel of the ATS Model 524 flow phantom was collected using a linear array probe (LA14-5/38) with the axis of the channel and the beam perpendicular to each other. The MDST phase coupled algorithm has been used to estimate the lateral displacement from the flow in addition to the axial displacement of the pulsating channel wall. Fig. 5.5 and Fig. 5.6 illustrate an instance of the estimates of the displacement acquired with the the M2D imaging in the axial and lateral direction respectively.

More specifically Fig. 5.5 highlight the channel contraction detected by the axial displacement estimate while Fig. 5.6 shows the mostly uniform flow detected by the lateral displacement estimate.

The strain fields are shown in Fig. 5.7, Fig. 5.8 for the axial and lateral direction respectively while Fig. 5.9 shows the shear strain field of the axial. An indication of any channel narrowing or existence of plaques built in the wall of the vessel can be detected from the lateral shear strain field shown in Fig. 5.10 .

5.6.5 In Vivo Results

The imaging probe with M2D mode was placed to get a longitudinal view of the carotid artery, the image data has been collected at a frame rate of 325. In all figures, the study fields are color-coded and overlaid on the B-mode images of the carotid artery segment. All the data shown in this subsection is using the MDST method of the carotid artery. Fig. 5.11 shows the axial displacement field represented by highlighting

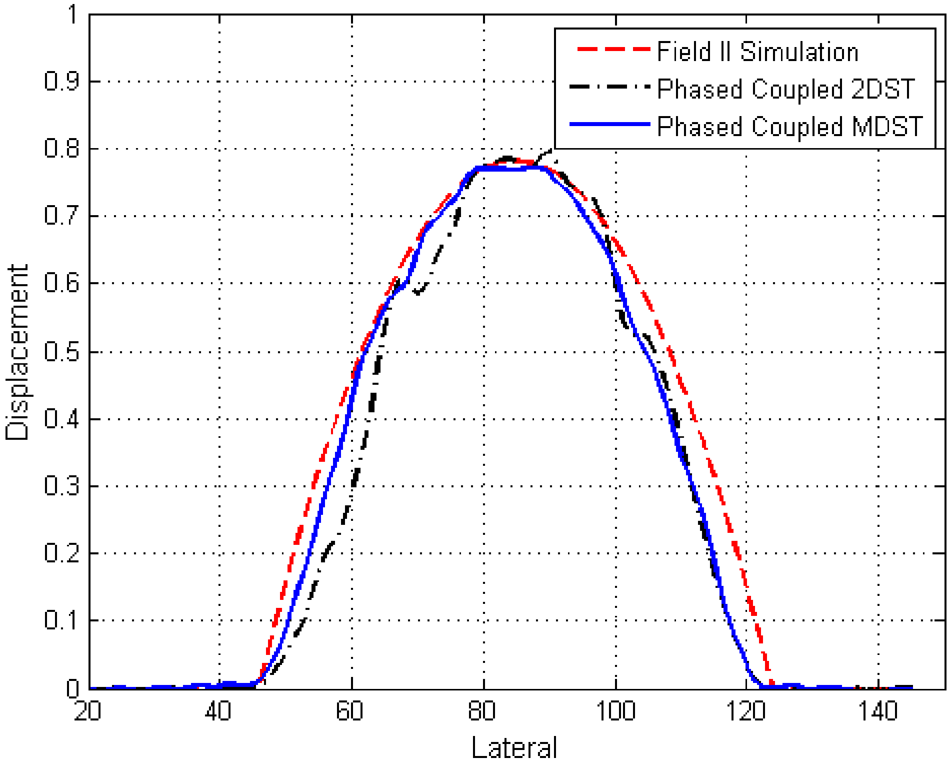

Figure 5.1: The lateral displacement from the simulated flow phantom for the simulated model (dashed line), phase coupled 2DST (dash-dot line) and the phase coupled MDST (solid line).

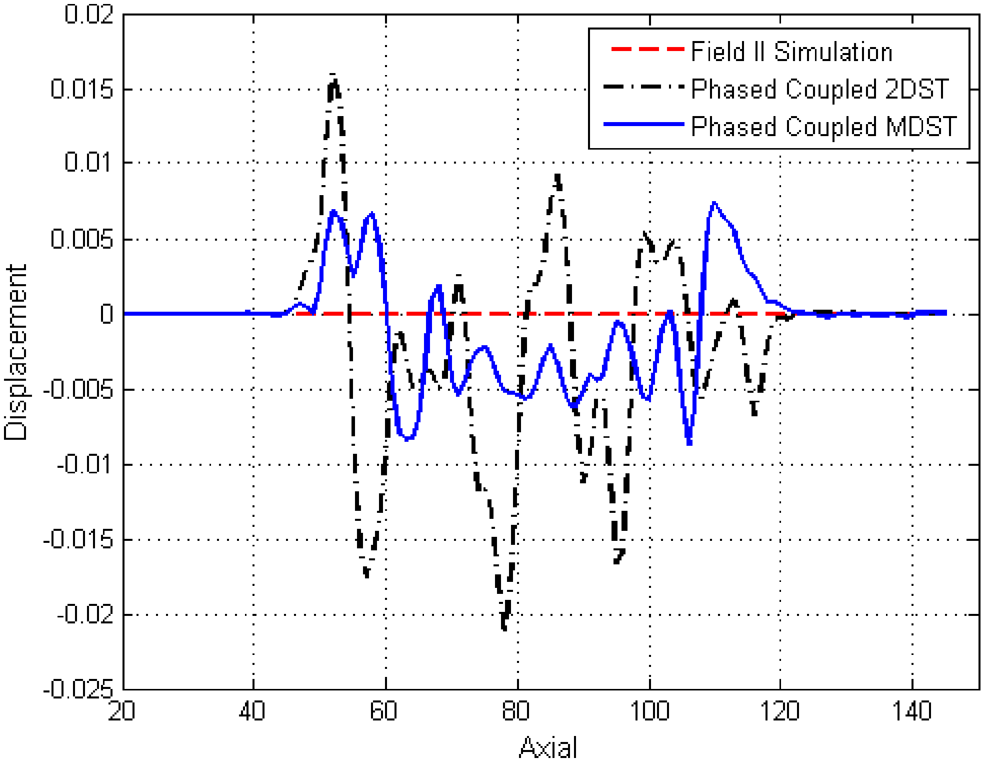

Figure 5.2: The axial displacement from the simulated flow phantom for the simulated model (dashed line), phase coupled 2DST (dash-dot line) and the phase coupled MDST (solid line).

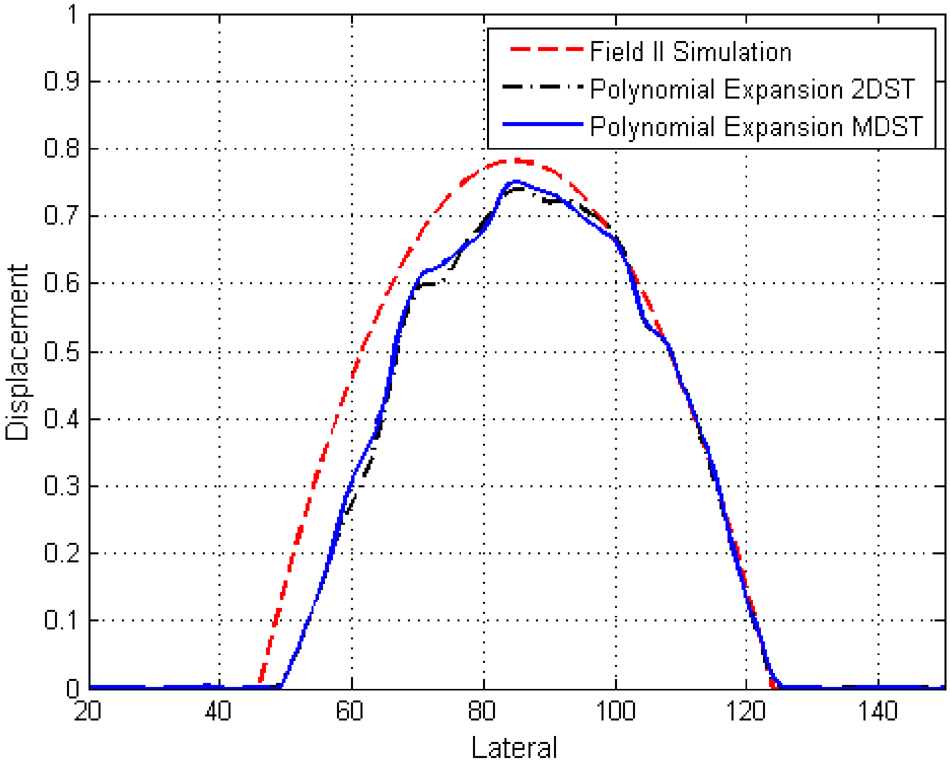

Figure 5.3: The lateral displacement from the simulated flow phantom for the simulated model (dashed line), polynomial expansion 2DST (dash-dot line) and the polynomial expansion MDST (solid line).

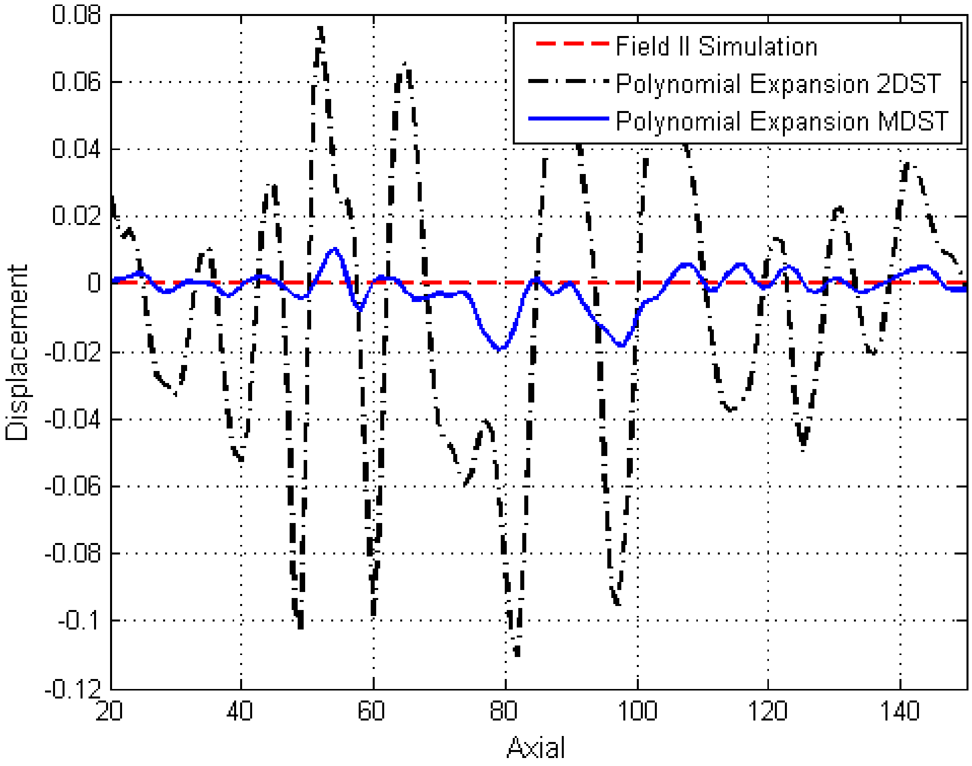

Figure 5.4: The axial displacement from the simulated flow phantom for the simulated model (dashed line), polynomial expansion 2DST (dash-dot line) and the polynomial expansion MDST (solid line).

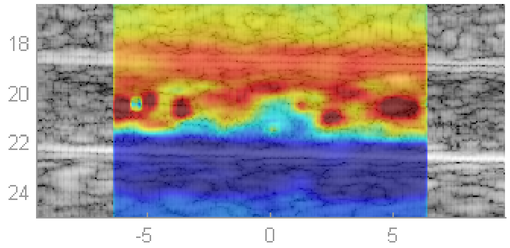

Figure 5.5: The axial displacement from the flow phantom. The results with color coded are overlaid on the B-mode images. Displacements and distances are in mm

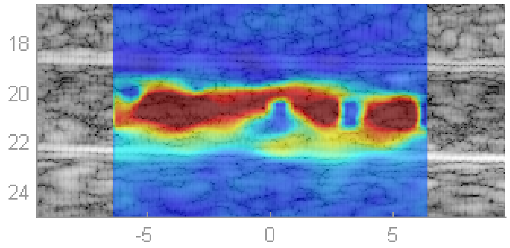

Figure 5.6: The Lateral displacement from the flow phantom. The results with color coded are overlaid on the B-mode images. Displacements and distances are in mm

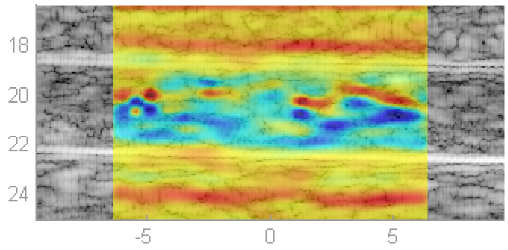

Figure 5.7: The axial strain of the flow phantom.

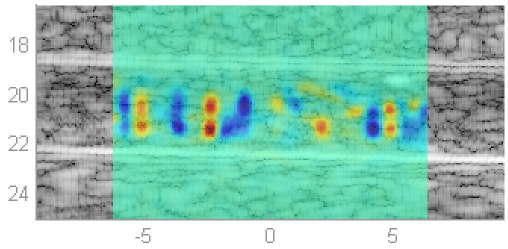

Figure 5.8: The lateral strain of the flow phantom.

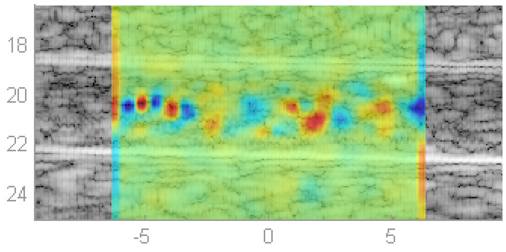

Figure 5.9: The axial shear strain of the flow phantom.

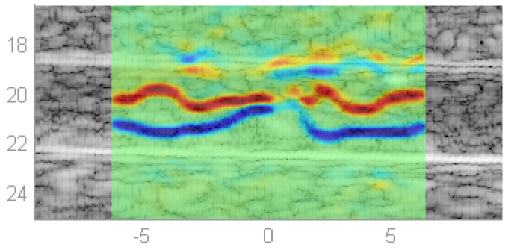

Figure 5.10: The lateral shear strain of the flow phantom.

the motion strength of the vessel wall. Simultaneously Fig. 5.12 gives an indication of the lateral movement of speckles due to the flow of blood cells. This shows the ability of tracking motion (tissue motion and flow pattern) fields in both directions simultaneously with the ultrasound probe placed in any arbitrary angle to the tissue structure. The conterminous of the displacement field throughout the interested region facilitate the calculation of the strain and shear strain.

This can be better illustrated in Fig. 5.13 which provides a measurement of the thickness of the vessel wall through the calculation of the axial strain. Fig. 5.15 gives an indication of the of the pulse wave propagation through the calculated axial shear strain in the vessel wall region. The stiffness of arteries can be estimated by the velocity of these pulses.

Furthermore, Fig. 5.14 and Fig. 5.16 show the lateral strain and the lateral sheer strain which can be used with axial strain and axial shear strain for detecting any plaque and any artery wall problems.

The change of the vessel diameter illustrate the pulsation pattern of the vessel wall motion as shown in Fig. 5.17.

5.7 Discussion

The simulation results presented in this chapter provided validation of the N-dimensional generalization of the analytic signal based on the vector extension of the Hilbert transform known as the Riesz transform. Compared to our previous results addressing the displacement estimation used in [111]. The 2-D speckle tracking approach described in [111] simply attempted to find the crossing between the gradient of the magnitude and the zero-phase of the 2-D complex correlation of the analytic signal. The approach described in this chapter utilized the Riesz transform to generate the sophisticated 2-D analytic signal. The new MDST method is used in the displacement estimation of a simulated flow image, flow phantom, and $in-vivo$ (carotid artery) data. The displacement is estimated from acquired successive radio-frequency (RF) data frames of the region of interest. The Field II simulation of flow data in a channel is generated to provide a validation for the accuracy of the method. The window size used in the algorithm is a typical size used in literature (not adaptive) and no trials done in the optimization of

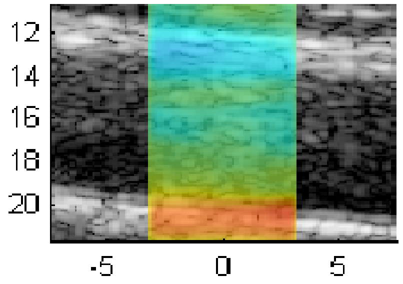

Figure 5.11: The axial displacement of the carotid artery. The results with color coded are overlaid on the B-mode images. Displacements and distances are in mm

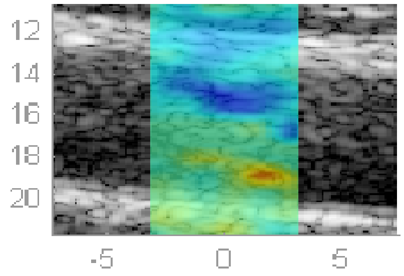

Figure 5.12: The Lateral displacement of the carotid artery. The results with color coded are overlaid on the B-mode images. Displacements and distances are in mm

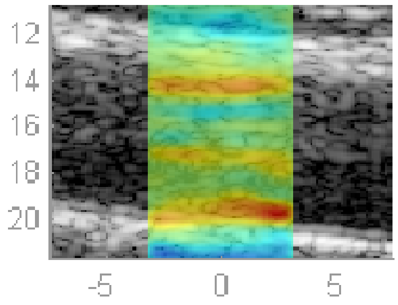

Figure 5.13: The axial strain of the carotid artery.

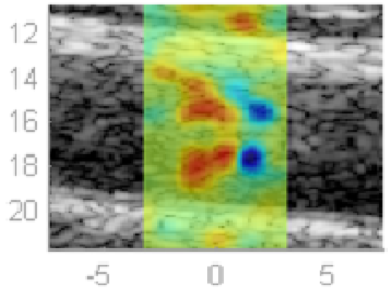

Figure 5.14: The lateral strain of the carotid artery.

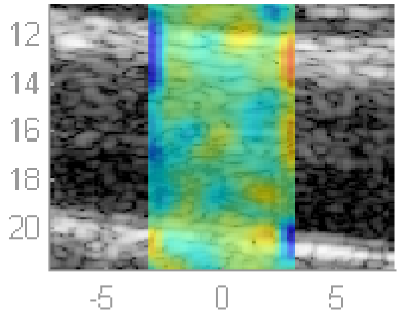

Figure 5.15: The axial shear strain of the carotid artery.

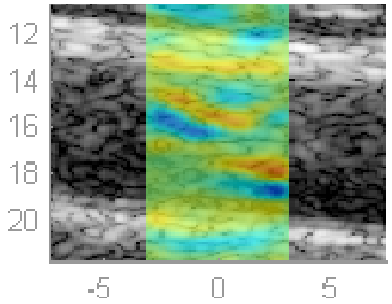

Figure 5.16: The lateral shear strain of the carotid artery.

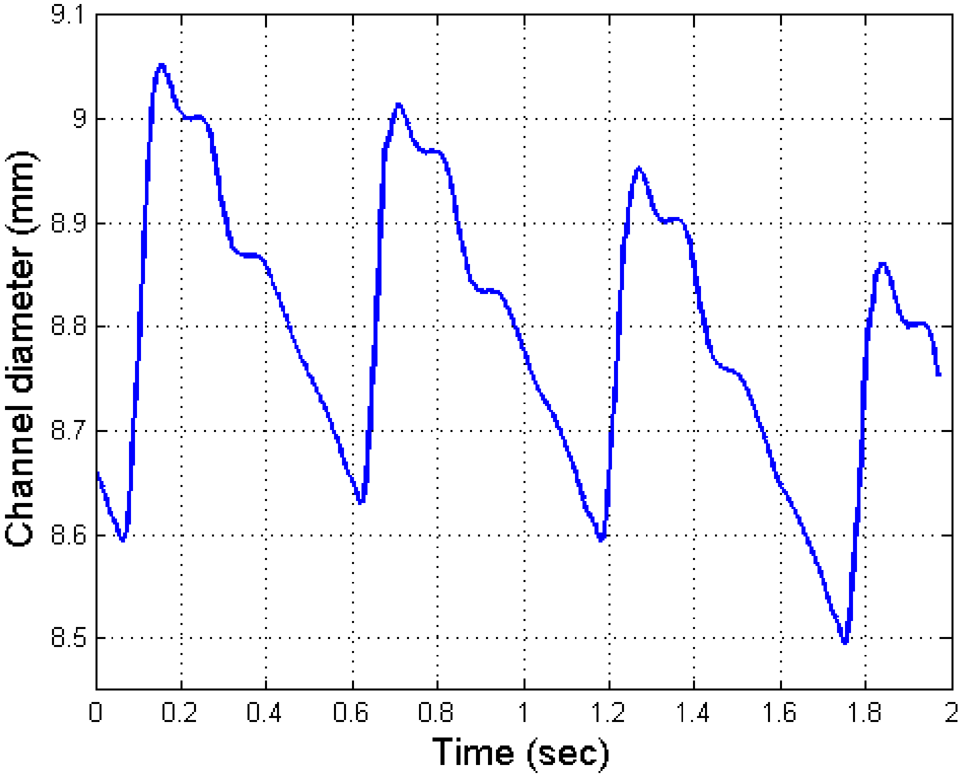

Figure 5.17: The change of the vessel diameter obtained from the two dimensional displacement field.

its size.

The flow channel experiment demonstrates the use of the MDST algorithm in estimating displacement in both directions. It also shows the applicability of the generalization algorithm in high frequency linear arrays. In this case, it is interesting to note that the lake of lateral flow information from B-mode image, has been highly recognized from the displacement estimation that expresses possible narrowing around the center of the flow channel. The estimated displacement fields clearly demonstrate a well behaved nature as can be seen from the smoothness of the calculated strain. It is important to note that the expansion and contraction of the channel due to roller pump action has been detected by our method. This has been clearly shown from the estimated displacement fields in both directions. Another important observation that can be made regarding the estimated fields is the clear contrast between the surrounding tissue mimicking material and the channel. On the other hand we used a low pass filter for the calculated average flow velocity. As we have observed from the results, the quasi-periodic nature of the flow velocity in addition to the relationship between the flow and the diameter in terms of their phase are shown clearly.

A characterization of the flow in a blood vessel (Carotid artery) has been demonstrated by the generalization algorithm (MDST). The results demonstrate the pulse wave propagation in the vessel wall region. One can use the pulse wave velocity to estimate mechanical properties of the arteries, e.g. (stiffness) [124], [125], [126]. A key result that can be obtained from the displacement of the upper and lower vessel walls is the vessel diameter. In addition, the displacement of a small region in the channel can be used to calculate the average flow velocity. The artifact and the noise has been filtered with a simple band pass filter and as expected, the pattern of the change in diameter coincide with the blood pressure wave. As indicated previously, the strain and the sheer strain in both directions could provide a tool for analysis and detection of plaque and local blood clots.

Conclusion

The new MDST method is used in the estimation of the flow and surrounding tissue motion on controlled tissue-mimicking flow phantom (ATS Model 524) and human carotid artery $in - vivo$. The data was collected using a linear array probe (LA14-5/38) of a Sonix RP ultrasound scanner at 325 fps. The vessel diameter has been calculated from the upper and lower vessel walls displacement, and clearly shows a blood pressure wave like pattern. The results obtained show that using the Riesz transform produces a more robust estimation of the true displacement of the simulated model compared to previously published results.

Chapter 6

Conclusion and Future Work

6.1 Conclusion

This dissertation addressed the problem of a refocusing algorithm that can efficiently steer higher power towards the target while controlling power deposition on critical points. A simulation of the effect of the new approach on the rib cage is presented and compared to the results of the pseudo inverse method used for minimal power deposition over the critical points. The proposed approach can be used to efficiently refocus HIFU beams through the rib cage and scattering objects in order to achieve a higher energy deposition within the target tumor. We have shown that allowing partial transmission through ribs can achieve higher intensity gain at the focus. In addition, the dissertation demonstrated an image-based modeling program that considered the actual anatomical details of the therapeutic region and was able to predict the outcome of the treatment process. The simulation model also correctly predicted the protection of the intima by the heat sink effect due to blood flow in the targeted vessel. This could be significant when noninvasive HIFU is used in the treatment of vulnerable plaques. Finally, we introduced a new multi-dimensional speckle tracking method (MDST) with subsample accuracy in all dimensions. The displacement is estimated from acquired successive radio-frequency (RF) data frames of the region of interest. A Field II simulation of flow data in a channel is generated to provide validation of the accuracy of the method. In addition, the new MDST method is applied to imaging data from the carotid artery of a healthy volunteer. The results obtained show that using Riesz transform produces a more robust estimation of the true displacement of the simulated model compared to previously published results.

6.2 Future Work

6.2.1 Fourier Continuation Method to solve partial differential equations

Partial Differential Equations (PDE) can be solved using various techniques like finite difference, spectral methods, pseudo-spectral methods etc. These methods, although accurate, suffer from Gibbs phenomenon. If the function is not periodic and the discrete Fourier transform is taken, the Gibbs phenomenon will be seen near discontinuities, where oscillations develop and the rate of convergence decreases as n (sample points) increases. Fig. 6.1, demonstrates this effect for a function $f(x) = x^2$ for $n = 300$. As can be clearly seen, the Fourier (spectral) method does not track the original function.

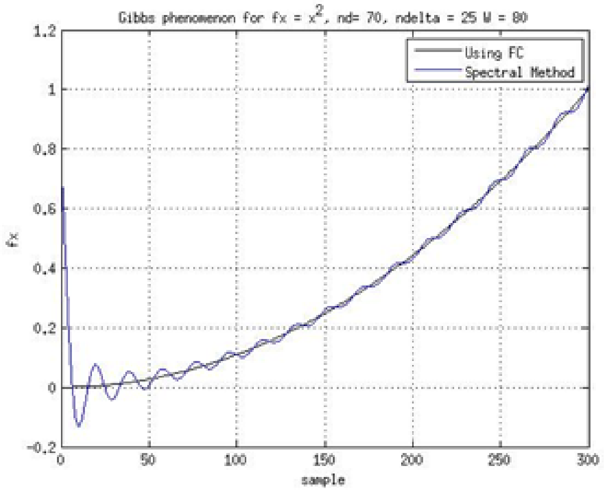

Figure 6.1: Demonstration of Gibbs phenomenon using Fourier interpolation (Spectral method) with 80 Fourier modes over a domain [0, 1], $f(x) = x^2$.

A Fourier Continuation (FC) method [127] is newly developed for countering this problem. Although similar techniques such as Chebyshev polynomials and Gegenbauer methods have been developed, they have certain problems like applicability in an arbitrary domain and slower convergence respectively. But perhaps the most attractive feature with FC method is that it lends to faster processing on large domains using fringing. Thus, the simulation can be implemented on parallel processors, reducing the simulation time and still maintaining the accuracy. The basic concept and algorithm developed for the FC method need to be studied in addition to some applications of the FC methods in solving PDE [128], [129] and calculating derivative using FFT.

Consider a smooth function $f \epsilon C^k[x_l, x_r]$ for some positive integer k, and assume approximate values of the function are known on a discrete grid $x_j, \quad j = 1, , n$. Assume $f \epsilon R[0, 1]$ and use the discrete grid

$$\boxed{x_j = \frac{j-1}{h}, \quad j = 1, ..., n, \qquad h = \frac{1}{n-1}.} \tag{6.1}$$

The FC algorithm relies on extending the periodicity of the function to $[0, 1+d], where d > 1$. Thus the new function will be,

$$f_{de}(x) = \begin{cases} f(x) & x = [0, 1] \\ f_{match}(x) & x = (1, 1+d] \end{cases} \tag{6.2}$$

The spectrally accurate Fourier continuation can then be obtained as a Fourier transform on the grid values of the discontinuous Fourier Extension eq. 6.2, and uniformly sampling it at $n + N_d - 2$ Points, where

$$\boxed{\Delta = h(N_\Delta - 1), \quad d = h(N_d - 1), ..., n, \qquad h = \frac{1}{n-1}.} \tag{6.3}$$

6.2.2 Nonlinear Simulation

Nonlinear propagation can have beneficial or detrimental effects on focused ultrasound beams for imaging and therapy. The advent of piezocomposite transducer technology has allowed for the fabrication of a new generation of therapeutic arrays with relatively wide bandwidth and low cross coupling between elements (resulting in new dual-mode ultrasound array (DMUA) systems for imaging and therapy). The feedback capabilities of DMUAs offer new opportunities to characterize the HIFU beam in situ, including its spectral components due to harmonic generation. This form of feedback allows for the optimization of the DMUA driving patterns to achieve maximum therapeutic gain, by maximizing the harmonic generation within the focal spot. We present a preliminary results of simulation modeling of nonlinear wave propagation from the surface of currently available DMUA prototypes ($1MHz$) into the treatment volume, modeled as heterogeneous absorbing mediums. The DMUA has f-number of 0.8 and geometrically focused at 100 mm with surface intensity of $2.2W/cm^2$. This new transducer technology has provided us with a new generation of transducers capable of producing high power levels suitable for therapy and resulted in array elements leading to more predictable element and beam patterns, both in imaging and therapy modes. A numerical solution for the Khokhlov Zabolotskaya- Kuznetsov (KZK) equation [130] which accounts for diffraction in the parabolic approximation, non-linearity, and thermo viscous absorption is found by means of operator splitting and propagation along the spatial depth coordinate.

$$\boxed{\frac{\partial}{\partial \tau}[\frac{\partial P}{\partial Z} - \frac{\beta}{c^3 \rho} P \frac{\partial P}{\partial \tau} - \frac{\delta}{2c^3} \rho \frac{\partial^2 P}{\partial \tau^2}] = \frac{c}{2} \Delta_T P} \tag{6.4}$$

where P is the acoustic pressure in the beam, Z is the coordinate along the beam axis, $c = 1612m/s$ is the propagation velocity of longitudinal acoustic waves in the tissue, $\rho = 1210kg/m3$ is the density, $\beta = 4.78$ is the nonlinearity factor of the tissue [131] and Δ_T is the Laplacian with respect to the transverse coordinates, which, in the case of an axisymmetric beam considered here, has the form $\Delta_T = \frac{\partial^2}{\partial x^2} + \frac{\partial^2}{\partial y^2}$.

The numerical model simulate the nonlinear propagation of therapeutic ultrasound pulses through tissue. The effects of acoustic nonlinearity play a considerable role in the case of such a HIFU; they lead to the appearance of additional higher harmonics in the initial wave spectrum in addition to an increase in temperature. The prediction of the harmonics field was sensitive to the choice of frequency dependent absorption. In comparing the spatial distribution we found that the harmonics had reduced amplitude in the near field and lower amplitude side lobes in the focal region than the fundamental. A non-linear propagation of ultrasound lead to increase the heat generation due to the preferential absorption of harmonics of the original frequency. The FDTD simulation allows for computation of the temperature rise throughout the therapeutic region as governed by the transient bioheat transfer equation. The purpose of this work is the investigation of the effects of acoustic nonlinearity in the process of the tissue heating by a HIFU beam in DMUA with sinusoidal excitation. The absorption is represented as follows:

$$\boxed{\alpha(f) = \alpha_o (f/f_o)^{\gamma}.} \tag{6.5}$$

Where the power index γ is close to unity, α is the absorption coefficient at a frequency f, and α_o is the absorption coefficient at the selected frequency f_o [132]. We use the temporal finite-difference schemes to solve eq. 6.4. The nonlinear transformation of the wave energy up the spectrum leads to an increase in the absorption of the ultrasonic wave energy because of the growth of the absorption coefficient with frequency eq. 6.5. In the case of a strong influence of the nonlinear effects, the heating of the tissue increases most strongly in the focal region [133]. In the case of a propagating harmonic wave, the heat release in the focus, $q = 2\alpha_o I = 2\alpha_o p^2/2\rho c$, is proportional to the wave intensity I or the squared pressure amplitude P. The results obtained from the simulation of eq. 6.4 provide an opportunity to investigate the influence of acoustic nonlinearity on the temporal and spatial characteristics of an ultrasonic beam, on the distribution of thermal sources, and on the evolution of the thermal field in the tissue. Fig. 6.2 shows the profiles of an acoustic wave in the focal region along and across the beam axis respectively, which are calculated with allowance for nonlinear effects.

6.2.3 Affine Model

A more general model, such as the affine model [111, 134, 135], can replace the too restrictive simple translation model for estimating the local displacement, accounting for rotation, expansion, compression and shear. This can provides a realistic description of the tissue motion patterns. Shear strains correspond to a twist or rotation, while normal strains correspond to pure compression and/or expansion. In the 2D domain, the affine transformation is defined by 6 parameters at position $\mathbf{d} = [d_x; d_y]$. Two parameters accounts for translation $[dx; dy]$ and the rest accounts for strain and shear strain. This can be represented as:

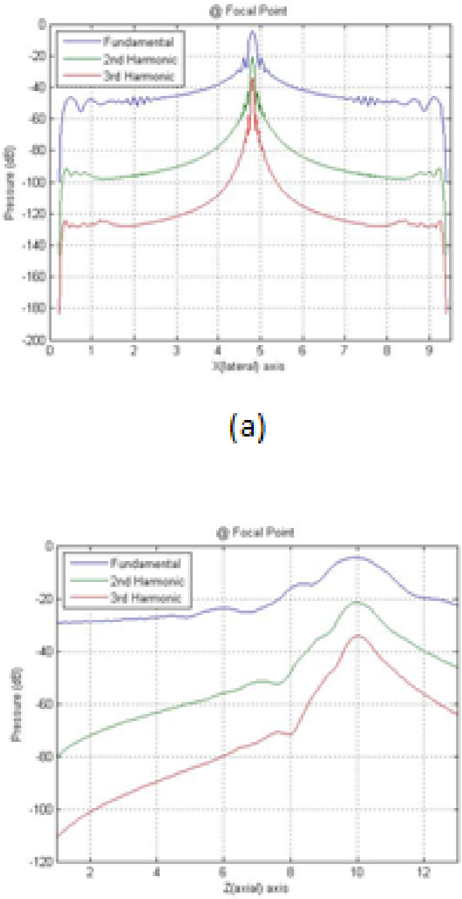

(a)

(b)

Figure 6.2: The wave profile in the focal region of the DMUA 1 MHz at (a) the lateral direction, (b) at the elevation direction and (c) at the axial direction. ©ISTU 2011

$$\begin{pmatrix} d_x \\ d_y \end{pmatrix} = \begin{pmatrix} \partial_x d_x & \partial_y d_x \\ \partial_x d_y & \partial_y d_y \end{pmatrix} \begin{pmatrix} x_o \\ y_o \end{pmatrix} + \begin{pmatrix} dx \\ dy \end{pmatrix} \tag{6.6}$$

This model can accounts for the typical contraction, shear and torsion of the heart motion.

References

[1] Young-sun Kim, Hyunchul Rhim, Min Joo Choi, Hyo Keun Lim, and Dongil Choi. High-intensity focused ultrasound therapy: an overview for radiologists. *Korean Journal of Radiology*, 9(4):291–302, 2008.

[2] Gunnar Myrdal, Sigridur Valtysdottir, Mats Lambe, and Elisabeth Ståhle. Quality of life following lung cancer surgery. *Thorax*, 58(3):194–197, 2003.

[3] Robert Williams Wood and Alfred L Loomis. Xxxviii. the physical and biological effects of high-frequency sound-waves of great intensity. *Philosophical Magazine Series 7*, 4(22):417–436, 1927.

[4] John G Lynn, Raymund L Zwemer, Arthur J Chick, and August E Miller. A new method for the generation and use of focused ultrasound in experimental biology. *The Journal of general physiology*, 26(2):179, 1942.

[5] William J Fry. Biological and medical acoustics. *The Journal of the Acoustical Society of America*, 30(5):387–393, 2005.

[6] JY Chapelon, M Ribault, A Birer, F Vernier, R Souchon, and A Gelet. Treatment of localised prostate cancer with transrectal high intensity focused ultrasound. *European journal of ultrasound*, 9(1):31–38, 1999.

[7] Laura Poissonnier, Jean-Yves Chapelon, Olivier Rouviere, Laura Curiel, Raymonde Bouvier, Xavier Martin, Jean Michel Dubernard, and Albert Gelet. Control of prostate cancer by transrectal hifu in 227 patients. *European Urology*, 51(2):381–387, 2007.

[8] MR Imaging-guided Focused. Ultrasound surgery of uterine leiomyomas: A feasibility study. *Radiology*, 226:897–905, 2003.

[9] James P Vetro and Ferenc A Jolesz. Focused us system for mr imaging-guided tumor ablation. *Radiology*, 194:731–737, 1995.

[10] Emad S Ebbini and Charles A Cain. A spherical-section ultrasound phased array applicator for deep localized hyperthermia. *Biomedical Engineering, IEEE Transactions on*, 38(7):634–643, 1991.

[11] Emad S Ebbini, John C Bischof, Rachana K Visaria, and Ajay Shrestha. Quadratic b-mode and pulse inversion imaging of thermally-induced lesions in vivo. In *Biomedical Imaging: From Nano to Macro, 2007. ISBI 2007. 4th IEEE International Symposium on*, pages 1120–1123. IEEE, 2007.

[12] Pornchai Phukpattaranont and Emad S Ebbini. Post-beamforming second-order volterra filter for pulse-echo ultrasonic imaging. *Ultrasonics, Ferroelectrics and Frequency Control, IEEE Transactions on*, 50(8):987–1001, 2003.

[13] Ferenc A Jolesz and Kullervo H Hynynen. *MRI-guided focused ultrasound surgery.* CRC Press, 2013.

[14] Mathieu Pernot, Mickael Tanter, and Mathias Fink. Feasibility of real-time motion correction for hifu applications. In *Ultrasonics, 2003 IEEE Symposium on*, volume 1, pages 998–1001. IEEE, 2003.

[15] Claudio Simon, Idris A Elbakri, Jian Shen, Timothy L Hall, and Emad S Ebbini. Combined ultrasound image guidance and therapy using a therapeutic phased array. In *Medical Imaging'98*, pages 89–98. International Society for Optics and Photonics, 1998.

[16] Gerard Fleury, David Melo de Lima, Kullervo Hynynen, Remi Berriet, Olivier Le Baron, and Bertrand Huguenin. New piezocomposite transducers for therapeutic ultrasound. In *Biomedical Optics 2003*, pages 227–236. International Society for Optics and Photonics, 2003.

[17] Yayun Wan and Emad S Ebbini. A post-beamforming 2-d pseudoinverse filter for coarsely sampled ultrasound arrays. *Ultrasonics, Ferroelectrics and Frequency Control, IEEE Transactions on*, 56(9):1888–1902, 2009.

[18] VS Gierenz, R Schwann, and TG Noll. A low power digital beamformer for handheld ultrasound systems. In *Solid-State Circuits Conference, 2001. ESSCIRC 2001. Proceedings of the 27th European*, pages 261–264. IEEE, 2001.

[19] Vijay Shamdasani, Ravi Managuli, Siddhartha Sikdar, and Yongmin Kim. Ultrasound color-flow imaging on a programmable system. *Information Technology in Biomedicine, IEEE Transactions on*, 8(2):191–199, 2004.

[20] Jieming Ma, Kerem Karadayi, Murtaza Ali, and Yongmin Kim. Software-based ultrasound phase rotation beamforming on multi-core dsp. In *Ultrasonics Symposium (IUS), 2011 IEEE International*, pages 503–506. IEEE, 2011.

[21] C Yoon, J Lee, YM Yoo, and T-K Song. Display pixel based focusing using multi-order sampling for medical ultrasound imaging. *Electronics letters*, 45(25):1292–1294, 2009.

[22] Alan V Oppenheim, Ronald W Schafer, John R Buck, et al. *Discrete-time signal processing*, volume 2. Prentice-hall Englewood Cliffs, 1989.

[23] HT Feldkamper, R Schwann, V Gierenz, and TG Noll. Low power delay calculation for digital beamforming in handheld ultrasound systems. In *Ultrasonics Symposium, 2000 IEEE*, volume 2, pages 1763–1766. IEEE, 2000.

[24] Gi-Duck Kim, Changhan Yoon, Sang-Bum Kye, Youngbae Lee, Jeeun Kang, Yangmo Yoo, and Tai-Kyong Song. A single fpga-based portable ultrasound imaging system for point-of-care applications. *Ultrasonics, Ferroelectrics and Frequency Control, IEEE Transactions on*, 59(7):1386–1394, 2012.

[25] Chang-Hong Hu, Xiao-Chen Xu, Jonathan M Cannata, Jesse T Yen, and K Kirk Shung. Development of a real-time, high-frequency ultrasound digital beamformer for high-frequency linear array transducers. *Ultrasonics, Ferroelectrics and Frequency Control, IEEE Transactions on*, 53(2):317–323, 2006.

[26] Ronald A Mucci. A comparison of efficient beamforming algorithms. *Acoustics, Speech and Signal Processing, IEEE Transactions on*, 32(3):548–558, 1984.

[27] Timo I Laakso, Vesa Valimaki, Matti Karjalainen, and Unto K Laine. Splitting the unit delay [fir/all pass filters design]. *Signal Processing Magazine, IEEE*, 13(1):30–60, 1996.

[28] Kane Yee. Numerical solution of initial boundary value problems involving maxwell's equations in isotropic media. *Antennas and Propagation, IEEE Transactions on*, 14(3):302–307, May 1966.

[29] Jean-Pierre Berenger. A perfectly matched layer for the absorption of electromagnetic waves. *Journal of computational physics*, 114(2):185–200, 1994.

[30] Qing-Huo Liu and Jianping Tao. The perfectly matched layer for acoustic waves in absorptive media. *The Journal of the Acoustical Society of America*, 102(4):2072–2082, 1997.

[31] Richard Courant, Kurt Friedrichs, and Hans Lewy. On the partial difference equations of mathematical physics. *IBM journal of Research and Development*, 11(2):215–234, 1967.

[32] S. A. Sapareto and W. C. Dewey. Thermal dose determination in cancer therapy. *International Journal of Radiation Oncology Biology Physics*, 10(6):787–800, 1984.

[33] P Hariharan, MR Myers, and RK Banerjee. Hifu procedures at moderate intensitieseffect of large blood vessels. *Physics in medicine and biology*, 52(12):3493, 2007.

[34] Youssry Y Botros, Emad S Ebbini, and John L Volakis. Two-step hybrid virtual array ray (var) technique for focusing through the rib cage. *Ultrasonics, Ferroelectrics and Frequency Control, IEEE Transactions on*, 45(4):989–1000, 1998.

[35] Hui Yao and Emad S Ebbini. Refocusing dual-mode ultrasound arrays in the presence of strongly scattering obstacles. In *Ultrasonics Symposium, 2004 IEEE*, volume 1, pages 239–242. IEEE, 2004.

[36] John Civale, Robert Clarke, Ian Rivens, and Gail Ter Haar. The use of a segmented transducer for rib sparing in hifu treatments. *Ultrasound in medicine & biology*, 32(11):1753–1761, 2006.

[37] J-F. Aubry, M. Pernot, F. Marquet, M. Tanter, and M. Fink. Transcostal high-intensity-focused ultrasound: ex vivo adaptive focusing feasibility study. *Phys Med Biol*, 53(11):2937–2951, Jun 2008.

[38] Mathias Fink. Time reversal of ultrasonic fields. i. basic principles. *Ultrasonics, Ferroelectrics and Frequency Control, IEEE Transactions on*, 39(5):555–566, 1992.

[39] Mathias Fink. Time reversal of ultrasonic fields. i. basic principles. *Ultrasonics, Ferroelectrics and Frequency Control, IEEE Transactions on*, 39(5):555–566, 1992.

[40] Claire Prada, Jean-Louis Thomas, and Mathias Fink. The iterative time reversal process: Analysis of the convergence. *The Journal of the Acoustical Society of America*, 97(1):62–71, 1995.

[41] Jean-Louis Thomas and Mathias A Fink. Ultrasonic beam focusing through tissue inhomogeneities with a time reversal mirror: application to transskull therapy. *Ultrasonics, Ferroelectrics and Frequency Control, IEEE Transactions on*, 43(6):1122–1129, 1996.

[42] Mickaël Tanter, Jean-Louis Thomas, and Mathias Fink. Focusing and steering through absorbing and aberrating layers: Application to ultrasonic propagation through the skull. *The Journal of the Acoustical Society of America*, 103(5):2403–2410, 1998.

[43] M. Tanter, M. Pernot, J. F. Aubry, G. Montaldo, F. Marquet, and M. Fink. Compensating for bone interfaces and respiratory motion in high-intensity focused ultrasound. *Int J Hyperthermia*, 23(2):141–151, Mar 2007.

[44] John R Ballard, Andrew J Casper, Yayun Wan, and Emad S Ebbini. Adaptive transthoracic refocusing of dual-mode ultrasound arrays. *Biomedical Engineering, IEEE Transactions on*, 57(1):93–102, 2010.

[45] Emad S Ebbini, Hui Yao, and Ajay Shrestha. Dual-mode ultrasound phased arrays for image-guided surgery. *Ultrasonic Imaging*, 28(2):65–82, 2006.

[46] P Gélat, G ter Haar, and N Saffari. Scattering of the field of a multi-element phased array by human ribs. In *Journal of Physics: Conference Series*, volume 353, page 012010. IOP Publishing, 2012.

[47] Pierre Gélat, Gail ter Haar, and Nader Saffari. Modelling of the acoustic field of a multi-element hifu array scattered by human ribs. *Physics in medicine and biology*, 56(17):5553, 2011.

[48] Svetlana Bobkova, Leonid Gavrilov, Vera Khokhlova, Adam Shaw, and Jeffrey Hand. Focusing of high-intensity ultrasound through the rib cage using a therapeutic random phased array. *Ultrasound in medicine & biology*, 36(6):888–906, 2010.

[49] E.S. Ebbini and C.A. Cain. Multiple-focus ultrasound phased-array pattern synthesis: optimal driving-signal distributions for hyperthermia. *Ultrasonics, Ferroelectrics and Frequency Control, IEEE Transactions on*, 36(5):540–548, Sept 1989.

[50] Paul Tseng. Further results on approximating nonconvex quadratic optimization by semidefinite programming relaxation. *SIAM Journal on Optimization*, 14(1):268–283, 2003.

[51] Nikos D Sidiropoulos, Timothy N Davidson, and Zhi-Quan Luo. Transmit beamforming for physical-layer multicasting. *Signal Processing, IEEE Transactions on*, 54(6):2239–2251, 2006.

[52] Emad SA Ebbini. Deep localized hyperthermia with ultrasound-phased arrays using the pseudoinverse pattern synthesis method. 1990.

[53] Francesco P Curra, Pierre D Mourad, Vera A Khokhlova, Robin O Cleveland, and Lawrence A Crum. Numerical simulations of heating patterns and tissue temperature response due to high-intensity focused ultrasound. *Ultrasonics, Ferroelectrics and Frequency Control, IEEE Transactions on*, 47(4):1077–1089, 2000.

[54] Yuri Nesterov, Henry Wolkowicz, and Yinyu Ye. Semidefinite programming relaxations of nonconvex quadratic optimization. In *Handbook of semidefinite programming*, pages 361–419. Springer, 2000.

[55] Ralf Seip, Philip VanBaren, and Emad S Ebbini. Dynamic focusing in ultrasound hyperthermia treatments using implantable hydrophone arrays. *Ultrasonics, Ferroelectrics and Frequency Control, IEEE Transactions on*, 41(5):706–713, 1994.

[56] Jean-François Aubry, Mathieu Pernot, Fabrice Marquet, Mickaël Tanter, and Mathias Fink. Transcostal high-intensity-focused ultrasound: ex vivo adaptive focusing feasibility study. *Physics in medicine and biology*, 53(11):2937, 2008.

[57] Christian Dorme and MA Fink. Ultrasonic beam steering through inhomogeneous layers with a time reversal mirror. *Ultrasonics, Ferroelectrics and Frequency Control, IEEE Transactions on*, 43(1):167–175, 1996.

[58] Zhi-Quan Luo, Nicholas D Sidiropoulos, Paul Tseng, and Shuzhong Zhang. Approximation bounds for quadratic optimization with homogeneous quadratic constraints. *SIAM Journal on Optimization*, 18(1):1–28, 2007.

[59] Eleftherios Karipidis, Nikos D Sidiropoulos, and Zhi-Quan Luo. Quality of service and max-min fair transmit beamforming to multiple cochannel multicast groups. *Signal Processing, IEEE Transactions on*, 56(3):1268–1279, 2008.

[60] K.T. Phan, S.A. Vorobyov, N.D. Sidiropoulos, and C. Tellambura. Spectrum sharing in wireless networks via qos-aware secondary multicast beamforming. *Signal Processing, IEEE Transactions on*, 57(6):2323–2335, June 2009.

[61] Y. Nesterov and A. Nemirovsky. *Front Matter*, chapter 0, pages i–ix.

[62] Stephen P Boyd and Lieven Vandenberghe. *Convex optimization*. Cambridge university press, 2004.

[63] Jos F Sturm. Using sedumi 1.02, a matlab toolbox for optimization over symmetric cones. *Optimization methods and software*, 11(1-4):625–653, 1999.

[64] J. Lofberg. Yalmip : a toolbox for modeling and optimization in matlab. In *Computer Aided Control Systems Design, 2004 IEEE International Symposium on*, pages 284–289, Sept 2004.

[65] Omar Mehanna, N Sidiropoulos, and G Giannakis. Joint multicast beamforming and antenna selection. 2012.

[66] M.A. Munger and D.W. Hawkins. Atherothrombosis: epidemiology, pathophysiology, and prevention. *J. Am. Pharm. Assoc.*, 44(2):S5–S13, 2004.

[67] I.A. Shehata. Treatment with high intensity focused ultrasound: Secrets revealed. *Eur J. Radiol.*, 81(3):534–541, 2012.

[68] Laura Poissonnier, Albert Gelet, Jean-Yves Chapelon, Raymonde Bouvier, Olivier Rouviere, Catherine Pangaud, Denis Lyonnet, and Jean-Michel Dubernard. [results of transrectal focused ultrasound for the treatment of localized prostate cancer (120 patients with psa¡ or+ 10ng/ml]. *Progres en urologie: journal de l'Association francaise d'urologie et de la Societe francaise d'urologie*, 13(1):60–72, 2003.

[69] T. A. Gardner, M. O. Koch, A. Shalhav, R. Bihrle, R. S. Foster, C. Steidle, I. Grunberger, A. S. M. Resnick, J. Cochran, V. Rao, and N. T. Sanghvi. Minimally invasive treatment of benign prostatic hyperplasia with high intensity focused ultrasound using the sonablate tm system: An updated report of phase iii clinical studies conducted in the usa.

[70] Narendra T Sanghvi, Francis J Fry, Richard Bihrle, Richard S Foster, Michael H Phillips, Jayne Syrus, Alexander V Zaitsev, and Carl W Hennige. Noninvasive surgery of prostate tissue by high-intensity focused ultrasound. *Ultrasonics, Ferroelectrics and Frequency Control, IEEE Transactions on*, 43(6):1099–1110, 1996.

[71] Sheng Li and Pei-Hong Wu. Magnetic resonance image-guided versus ultrasound-guided high-intensity focused ultrasound in the treatment of breast cancer. *Chinese journal of cancer*, 32(8):441, 2013.

[72] Ali Ziadloo and Shahram Vaezy. Real-time 3d image-guided hifu therapy. In *Engineering in Medicine and Biology Society, 2008. EMBS 2008. 30th Annual International Conference of the IEEE*, pages 4459–4462. IEEE, 2008.

[73] Michael A Penna, Kris A Dines, Ralf Seip, Roy F Carlson, and Narendra T Sanghvi. Modeling prostate anatomy from multiple view trus images for image-guided hifu therapy. *Ultrasonics, Ferroelectrics and Frequency Control, IEEE Transactions on*, 54(1):52–69, 2007.

[74] Arthur H Chan, Victor Y Fujimoto, Donald E Moore, Roy W Martin, and Shahram Vaezy. An image-guided high intensity focused ultrasound device for uterine fibroids treatment. *Medical physics*, 29(11):2611–2620, 2002.

[75] Islam A Shehata, John R Ballard, Andrew J Casper, Leah J Hennings, Erik Cressman, and Emad S Ebbini. High-intensity focused ultrasound for potential treatment of polycystic ovarian syndrome: toward a noninvasive surgery. *Fertility and sterility*, 2013.

[76] Stephen Monteith, Jason Sheehan, Ricky Medel, Max Wintermark, Matthew Eames, John Snell, Neal F Kassell, and W Jeff Elias. Potential intracranial applications of magnetic resonance–guided focused ultrasound surgery: a review. *Journal of neurosurgery*, 118(2):215–221, 2013.

[77] Hüseyin Emre Güven. *Computational models and methods for ultrasound tomography*. PhD thesis, Northeastern University Boston, 2012.

[78] Francesco P Curra, Pierre D Mourad, Lawrence A Crum, and Vera A Khokhlova. 3d full wave ultrasonic field and temperature simulations in biological tissue containing a blood vessel. *The Journal of the Acoustical Society of America*, 107(5):2814–2814, 2000.

[79] E Sassaroli, KCP Li, and BE O'Neill. Modeling focused ultrasound exposure for the optimal control of thermal dose distribution. *The Scientific World Journal*, 2012, 2012.

[80] Vera A Khokhlova, Olga V Bessonova, Mikhail V Averiyanov, Joshua E Soneson, and Robin O Cleveland. Modeling of nonlinear shock wave propagation and

thermal effects in high-intensity focused ultrasound fields. *The Journal of the Acoustical Society of America*, 127(3):1827–1827, 2010.

[81] M.S. Canney M.R. Bailey Khokhlova, V.A. and L.A. Crum. Ultra fast thermal effect of high intensity focused ultrasound (hifu) and localized boiling in tissue due to exposure of shock waves.

[82] Wayne Kreider, Petr V Yuldashev, Oleg A Sapozhnikov, Navid Farr, Ari Partanen, Michael R Bailey, and Vera A Khokhlova. Characterization of a multi-element clinical hifu system using acoustic holography and nonlinear modeling. *Ultrasonics, Ferroelectrics and Frequency Control, IEEE Transactions on*, 60(8), 2013.

[83] Hong Chen, Andrew A Brayman, Thomas J Matula, and Andrew P Evan. Vascular damage by ultrasound-activated microbubble induced vessel invagination. In *Ultrasonics Symposium (IUS), 2010 IEEE*, pages 678–681. IEEE, 2010.

[84] J.H. Hwang, A.A. Brayman, and S. Vaezy. Pulsed high-intensity focused ultrasound-induced endothelial cell injury in vessels infused with ultrasound contrast agent. In *istu2*, pages 275–281. IEEE, 2003.

[85] R.W. Hobson, W. C. Mackey, E. Ascher, and et al. Management of atherosclerotic carotid artery disease: Clinical practice guidelines of the society for vascular surgery. *J. Vasc. Surg.*, 48(2):480–486, 2008.

[86] I.A. Shehata, J.R. Ballard, A.J. Casper, D. Liu, and E.S. Ebbini. Feasibility of targeting atherosclerotic plaques by high intensity focused ultrasound using dual-mode ultrasound array systems: an in vivo study. *J. Vasc Interv. Radiol.*, 24(12):1880–1887, 2013.

[87] Andrew Casper, Dalong Liu, John Ballard, and Emad S Ebbini. Real-time implementation of a dual-mode ultrasound array. *Biomedical Engineering, IEEE Transactions on*, 60(10):2751–2759, 2013.

[88] James William Thomas. *Numerical partial differential equations: finite difference methods*, volume 22. Springer, 1995.

[89] Francis A Duck. *Physical properties of tissue: a comprehensive reference book*. Academic Pr, 1990.

[90] M.C. Gosselin A. Klingenböck N. Kuster P.A. Hasgall, E. Neufeld. Itis database for thermal and electromagnetic parameters of biological tissues.

[91] Chunming Li, Rui Huang, Zhaohua Ding, JChris Gatenby, Dimitris N Metaxas, and John C Gore. A level set method for image segmentation in the presence of intensity inhomogeneities with application to mri. *Image Processing, IEEE Transactions on*, 20(7):2007–2016, 2011.

[92]

[93] M. O'Donnell, A. R. Skovoroda, B. M. Shapo, and S. Y. Emelianov. Internal displacement and strain imaging using ultrasonic speckle tracking. 41(3):314–325, 1994.

[94] E. J. Chen, W. K. Jenkins, and W. D. J. O'Brien. The accuracy and precision of estimating tissue displacements from ultrasonic images. pages 1069–1072, 1992.

[95] J. R. Barron, D. J. Fleet, and S. S. Beauchemin. Performance of optical flow techniques. 12:43–77, 1994.

[96] D. Boukerroui, J. A. Noble, and M. Brady. *Velocity Estimation in Ultrasound Images: A Block Matching Approach*. Springer, 2003.

[97] D. J. Fleet and Y. Weiss. *Optical Flow Estimation*. Springer, 2005.

[98] Q. Duan, E. D. Angelini, S. L. Herz, C. M. Ingrassia, O. Gerard, K. D. Costa, J. W. Holmes, S. Homma, and A. F. Laine. Dynamic cardiac information from optical flow using four dimensional ultrasound. pages 4465–4468, 2005.

[99] Weichuan Yu, Ning Lin, Ping Yan, Kailasnath Purushothaman, Albert Sinusas, Karl Thiele, and James S. Duncan. Motion analysis of 3d ultrasound texture patterns. In *in Lecture Notes in Computer Science*, pages 252–261, 2003.

[100] B. Touil, A. Basarab, P. Delachartre, O. Bernard, and D. Friboulet. Analysis of motion tracking in echocardiographic image sequences: Influence of system geometry and point-spread function. 50(3):373–386, 2010.

[101] M. A. Lubinski, S. Y. Emelianov, , and M. O'Donnell. Speckle tracking methods for ultrasonic elasticity imaging using short-time correlation. 46(1):82–96, 1999.

[102] F. Marquet, M. Pernot, J. F. Aubry annd M. Tanter, G. Montaldo, and M. Fink. In-vivo non-invasive motion tracking and correction in high intensity focused ultrasound therapy. pages 688–691, 2006.

[103] E. J. Chen, W. K. Jenkins, and W. D. J. O'Brien. The impact of various imaging parameters on ultrasonic displacement and velocity estimates. 41(3):293–301, 1994.

[104] C. B. Compas, B. A. Lin, S. Sampath, A. J. Sinusas, , and J. S. Duncan. Combining shape and speckle tracking for deformation analysis in echocardiography using radial basis functions. pages 1322–1325, 2011.

[105] E. J. Harris, N. R. Miller, J. C. Bamber, J. R. N. Symonds-Tayler, and P. M. Evans. The effect of object speed and direction on the performance of 3d speckle tracking using a 3d swept-volume ultrasound probe. 56(22):7127–7143, 2011.

[106] C. Jia, P. Yan, A. J. Sinusas, D. P. Dione, B. A. Lin, Q. Wei, K. Thiele, T. J. Kolias, J. M. Rubin, L. Huang, J. S. Duncan, and M. O'Donnell. 3d elasticity imaging using principal stretches on an open-chest dog heart. pages 583–586, 2010.

[107] C. B. Burckhardt. Speckle in ultrasound b-mode scans. 25(1):1–6, 1978.

[108] B. Cohen and I. Dinstein. New maximum likelihood motion estimation schemes for noisy ultrasound images.

[109] G. Jacob, J. Noble, C. Behrenbruch, A. Kelion, and A. Banning. A shape-space-based approach to tracking myocardial borders and quantifying regional left-ventricular function applied in echocardiography. 21(3):226–238, 2002.

[110] M. Suhling, M. Arigovindan, C. Jansen, P. Hunziker, and M. Unser. Myocardial motion analysis from b-mode echocardiograms. *Image Processing, IEEE Transactions on*, 14(4):525–536, April 2005.

[111] Emad S Ebbini. Phase-coupled two-dimensional speckle tracking algorithm. *Ultrasonics, Ferroelectrics and Frequency Control, IEEE Transactions on*, 53(5):972–990, 2006.

[112] E. Stein and G. Weiss. *Introduction to Fourier Analysis on Euclidean Spaces.* NJ: Princeton Univ., 1971.

[113] Thomas Bülow and Gerald Sommer. Hypercomplex signals-a novel extension of the analytic signal to the multidimensional case. *IEEE trans. on Signal Processing*, pages 2844–2852, 2001.

[114] Thomas Bülow. *Hypercomplex spectral signal representations for the processing and analysis of images.* PhD thesis, Inst. für Informatik und Praktische Mathematik, 1999.

[115] G. H. Granlund and H. Knutsson. *Signal Processing for Computer Vision.* MA: Kluwer Academic Publishers Norwell, 1995.

[116] Stefan L Hahn. *Hilbert transforms in signal processing*, volume 2. Artech House Boston, 1996.

[117] Michael Felsberg and Gerald Sommer. The monogenic signal. *Signal Processing, IEEE Transactions on*, 49(12):3136–3144, 2001.

[118] Bracewell and Ronald Newbold. Two-dimensional imaging. *Two-Dimensional Imaging*, 1, 1995.

[119] Claudio Simon, Philip VanBaren, and Emad S Ebbini. Two-dimensional temperature estimation using diagnostic ultrasound. *Ultrasonics, Ferroelectrics and Frequency Control, IEEE Transactions on*, 45(4):1088–1099, 1998.

[120] Thanasis Loupas, JT Powers, and Robert W Gill. An axial velocity estimator for ultrasound blood flow imaging, based on a full evaluation of the doppler equation by means of a two-dimensional autocorrelation approach. *Ultrasonics, Ferroelectrics and Frequency Control, IEEE Transactions on*, 42(4):672–688, 1995.

[121] Andreas Pesavento, Christian Perrey, Martin Krueger, and Helmut Ermert. A time-efficient and accurate strain estimation concept for ultrasonic elastography

using iterative phase zero estimation. *Ultrasonics, Ferroelectrics and Frequency Control, IEEE Transactions on*, 46(5):1057–1067, 1999.

[122] Yayun Wan, Dalong Liu, and Emad S Ebbini. Simultaneous imaging of tissue motion and flow velocity using 2d phase-coupled speckle tracking. In *Ultrasonics Symposium (IUS), 2010 IEEE*, pages 487–490. IEEE, 2010.

[123] Jørgen Arendt Jensen. *Estimation of blood velocities using ultrasound: a signal processing approach*. Cambridge University Press, 1996.

[124] Jianwen Luo, Kana Fujikura, Leslie S Tyrie, MD Tilson, and Elisa E Konofagou. Pulse wave imaging of normal and aneurysmal abdominal aortas in vivo. *Medical Imaging, IEEE Transactions on*, 28(4):477–486, 2009.

[125] Kozo Hirata, Masanobu Kawakami, and Michael F ORourke. Pulse wave analysis and pulse wave velocity. *Circ J*, 70(10):1231–1239, 2006.

[126] Justine Ina Davies and Allan D Struthers. Pulse wave analysis and pulse wave velocity: a critical review of their strengths and weaknesses. *Journal of hypertension*, 21(3):463–472, 2003.

[127] Oscar P Bruno and Mark Lyon. High-order unconditionally stable fc-ad solvers for general smooth domains i. basic elements. *Journal of Computational Physics*, 229(6):2009–2033, 2010.

[128] Mark Lyon and Oscar P Bruno. High-order unconditionally stable fc-ad solvers for general smooth domains ii. elliptic, parabolic and hyperbolic pdes; theoretical considerations. *Journal of Computational Physics*, 229(9):3358–3381, 2010.

[129] Robin O Cleveland, Theresa Y Cheung, Nathan Albin, and Oscar P Bruno. Numerical simulation of focused nonlinear acoustic beams: A fourier continuation direct solver and comparisons to a paraxial approximation. *The Journal of the Acoustical Society of America*, 129(4):2611–2611, 2011.

[130] Janne Heikkila, Laura Curiel, and Kullervo Hynynen. Local harmonic motion monitoring of focused ultrasound surgerya simulation model. *Biomedical Engineering, IEEE Transactions on*, 57(1):185–193, 2010.

[131] Paul Meaney'Mark D Cahill and Gail ter Haar. The intensity dependence of focused ultrasound lesion position.

[132] Christopher Rowland Hill, Jeff C Bamber, and Gail Haar. *Physical principles of medical ultrasonics*, volume 2. Wiley Online Library, 2004.

[133] Mark F Hamilton, David T Blackstock, et al. *Nonlinear acoustics*, volume 237. Academic press San Diego, 1998.

[134] James R Bergen, Patrick Anandan, Keith J Hanna, and Rajesh Hingorani. Hierarchical model-based motion estimation. In *Computer VisionECCV'92*, pages 237–252. Springer, 1992.

[135] Gunnar Farneback. Very high accuracy velocity estimation using orientation tensors, parametric motion, and simultaneous segmentation of the motion field. In *Computer Vision, 2001. ICCV 2001. Proceedings. Eighth IEEE International Conference on*, volume 1, pages 171–177. IEEE, 2001.

Appendix A

Abbreviations

List of Acronyms

ABS	Absorbing Boundary Condition
ADC	Analog Digital Converter
ASIC	Application Specific Integrated Circuit
BHTE	Bioheat transfer Equation
CFL	Courant, Friedrichs and Lewy
CT	Connective Tissue
DMUA	Dual Mode Ultrasound Array
DSIQ	Direct Sampled In-phase/ Quadrature
DSP	Digital Signal Processing
FA	Femoral Artery
FC	Fourier Continuation
FDTD	Finite Difference Time Domain
FH	Familial Hypercholesterolemic

FPGA	Field Programmer Gate Array
FTCS	Forward Time Central Space
HCC	Hepatocellular Carcinoma
HIFU	High Intensity Focused Ultrasound Array
KZK	Khokhlov-Zabolotskaja-Kuznetsov
LPD	Limited Power Deposition
MDST	Multi-Dimension Speckle Tracking
MPD	Minimum Power Deposition
PDE	Partial Differential Equation
PML	Perfect Matched Layer
QCQP	Quadratic Constraints Quadratic Programming
RF	Radio Frequency
SA	Synthetic Aperture
SDR	Semidefinite Relaxation
STF	Single Transmit Focus
VAR	Virtual Array